



# **NAVAL POSTGRADUATE SCHOOL**

**MONTEREY, CALIFORNIA**

## **THESIS**

**NOVEL SYNTHESIS OF 3D GRAPHENE-CNF  
ELECTRODE ARCHITECTURES FOR  
SUPERCAPACITOR APPLICATIONS**

by

Jason W. Downs

June 2013

Thesis Co-Advisors:

Claudia Luhrs  
Dragoslav Grbovic

**Approved for public release; distribution is unlimited**

THIS PAGE INTENTIONALLY LEFT BLANK

<b>REPORT DOCUMENTATION PAGE</b>			<i>Form Approved OMB No. 0704-0188</i>	
Public reporting burden for this collection of information is estimated to average 1 hour per response, including the time for reviewing instruction, searching existing data sources, gathering and maintaining the data needed, and completing and reviewing the collection of information. Send comments regarding this burden estimate or any other aspect of this collection of information, including suggestions for reducing this burden, to Washington headquarters Services, Directorate for Information Operations and Reports, 1215 Jefferson Davis Highway, Suite 1204, Arlington, VA 22202-4302, and to the Office of Management and Budget, Paperwork Reduction Project (0704-0188) Washington DC 20503.				
<b>1. AGENCY USE ONLY (Leave blank)</b>		<b>2. REPORT DATE</b> June 2013	<b>3. REPORT TYPE AND DATES COVERED</b> Master's Thesis	
<b>4. TITLE AND SUBTITLE</b> NOVEL SYNTHESIS OF 3D GRAPHENE-CNF ELECTRODE ARCHITECTURES FOR SUPERCAPACITOR APPLICATIONS			<b>5. FUNDING NUMBERS</b>	
<b>6. AUTHOR(S)</b> Jason W. Downs				
<b>7. PERFORMING ORGANIZATION NAME(S) AND ADDRESS(ES)</b> Naval Postgraduate School Monterey, CA 93943-5000			<b>8. PERFORMING ORGANIZATION REPORT NUMBER</b>	
<b>9. SPONSORING /MONITORING AGENCY NAME(S) AND ADDRESS(ES)</b> N/A			<b>10. SPONSORING/MONITORING AGENCY REPORT NUMBER</b>	
<b>11. SUPPLEMENTARY NOTES</b> The views expressed in this thesis are those of the author and do not reflect the official policy or position of the Department of Defense or the U.S. government. IRB Protocol number ____ N/A ____.				
<b>12a. DISTRIBUTION / AVAILABILITY STATEMENT</b> Approved for public release; distribution is unlimited			<b>12b. DISTRIBUTION CODE</b> A	
<b>13. ABSTRACT (maximum 200 words)</b> <p>This manuscript presents a novel synthetic pathway for the generation of three-dimensional architectures which main structural component includes the combination of Graphene (G) and Carbon Nanofibers (CNF). The Reduction Expansion Synthesis (RES) approach was used for both, the exfoliation of Graphitic Oxide to produce Graphene, and the simultaneous reduction of a nickel salt to generate Ni catalyst. Carbon Nanofibers were grown from Ni following procedures previously reported. The use of dry and wet conditions for the RES synthesis was explored and the variability of sample properties due to such change analyzed. Resulting composites, Graphene/Carbon Nanofibers/Nickel nanoparticles (G/CNF/Ni) were characterized by X-ray diffraction, Scanning Electron Microscopy and BET surface area analysis. Some specimens were oxidized to produce G/CNF/NiO. All the materials were then used as electrodes in supercapacitor cells and the capacitance of the same evaluated.</p> <p>The growth of carbon nanofibers within the Graphene layers prevented the collapse of the layers when the material was laid as a paste in the current collectors and increased both ion and charge transport between the Graphene sheets. When combined with pseudocapacitive effects of NiO, a 350 percent increase in specific capacitance was attained for the G/CNF/NiO material when compared with its individual components.</p>				
<b>14. SUBJECT TERMS</b> Graphene, Carbon Nanofibers, Supercapacitors, Pseudocapacitors			<b>15. NUMBER OF PAGES</b> 113	
			<b>16. PRICE CODE</b>	
<b>17. SECURITY CLASSIFICATION OF REPORT</b> Unclassified	<b>18. SECURITY CLASSIFICATION OF THIS PAGE</b> Unclassified	<b>19. SECURITY CLASSIFICATION OF ABSTRACT</b> Unclassified	<b>20. LIMITATION OF ABSTRACT</b> UU	

THIS PAGE INTENTIONALLY LEFT BLANK

**Approved for public release; distribution is unlimited**

**NOVEL SYNTHESIS OF 3D GRAPHENE-CNF ELECTRODE  
ARCHITECTURES FOR SUPERCAPACITOR APPLICATIONS**

Jason W. Downs  
Lieutenant, United States Navy  
B.S., Purdue University, 2004

Submitted in partial fulfillment of the  
requirements for the degree of

**MASTER OF SCIENCE IN MECHANICAL ENGINEERING**

from the

**NAVAL POSTGRADUATE SCHOOL  
June 2013**

Author: Jason W. Downs

Approved by: Claudia C. Luhrs, PhD.  
Thesis Co-Advisor

Dragoslav Grbovic, PhD  
Thesis Co-Advisor

Knox T. Millsaps, PhD  
Chair, Department of Mechanical and Aerospace Engineering

THIS PAGE INTENTIONALLY LEFT BLANK

## ABSTRACT

This manuscript presents a novel synthetic pathway for the generation of three-dimensional architectures which main structural component includes the combination of Graphene (G) and Carbon Nanofibers (CNF). The Reduction Expansion Synthesis (RES) approach was used for both, the exfoliation of Graphitic Oxide to produce Graphene, and the simultaneous reduction of a nickel salt to generate Ni catalyst. Carbon Nanofibers were grown from Ni following procedures previously reported. The use of dry and wet conditions for the RES synthesis was explored and the variability of sample properties due to such change analyzed. Resulting composites, Graphene/Carbon Nanofibers/Nickel nanoparticles (G/CNF/Ni) were characterized by X-ray diffraction, Scanning Electron Microscopy and BET surface area analysis. Some specimens were oxidized to produce G/CNF/NiO. All the materials were then used as electrodes in supercapacitor cells and the capacitance of the same evaluated.

The growth of carbon nanofibers within the Graphene layers prevented the collapse of the layers when the material was laid as a paste in the current collectors and increased both ion and charge transport between the Graphene sheets. When combined with pseudocapacitive effects of NiO, a 350 percent increase in specific capacitance was attained for the G/CNF/NiO material when compared with its individual components.

THIS PAGE INTENTIONALLY LEFT BLANK



## TABLE OF CONTENTS

<b>I.</b>	<b>INTRODUCTION.....</b>	<b>1</b>
A.	<b>OVERVIEW .....</b>	<b>1</b>
B.	<b>ENERGY STORAGE TECHNOLOGY.....</b>	<b>1</b>
1.	Capacitor Theory .....	1
2.	Electric Double Layer Capacitors (Supercapacitors).....	2
3.	Carbon Electrode Technology .....	5
a.	<i>Graphene and Three-dimensional Architecture .....</i>	<i>6</i>
4.	Use of Metal Oxides in Supercapacitors .....	9
C.	<b>THESIS OBJECTIVES.....</b>	<b>10</b>
D.	<b>HYPOTHESIS.....</b>	<b>11</b>
<b>II.</b>	<b>EXPERIMENTAL METHODS .....</b>	<b>13</b>
A.	<b>GRAPHITE OXIDE PRODUCTION.....</b>	<b>13</b>
B.	<b>GRAPHENE PRODUCTION .....</b>	<b>16</b>
C.	<b>SYNTHESIS OF CARBON NANOFIBER ARCHITECTURES INTO   GRAPHENE LAYERS.....</b>	<b>17</b>
1.	Aqueous Preparation .....	19
a.	<i>Graphite Oxide Precursor.....</i>	<i>19</i>
b.	<i>Graphene Precursor.....</i>	<i>20</i>
2.	Dry Preparation .....	21
a.	<i>Graphite Oxide Precursor.....</i>	<i>22</i>
b.	<i>Graphene Precursor.....</i>	<i>23</i>
3.	Carbon Nanofiber Growth.....	23
4.	Oxidation Process.....	25
D.	<b>CARBON NANOFIBER BLANK SYNTHESIS .....</b>	<b>26</b>
E.	<b>ELECTRODE SYNTHESIS.....</b>	<b>26</b>
<b>III.</b>	<b>CHARACTERIZATION TECHNIQUES.....</b>	<b>31</b>
A.	<b>THERMOGRAVIMETRIC ANALYSIS .....</b>	<b>31</b>
B.	<b>X-RAY DIFFRACTION .....</b>	<b>32</b>
C.	<b>SCANNING ELECTRON MICROSCOPY .....</b>	<b>34</b>
D.	<b>BRUNAUER EMMETT TELLER SURFACE AREA ANALYSIS .....</b>	<b>35</b>
E.	<b>ELECTRICAL CHARACTERIZATION METHODS .....</b>	<b>37</b>
<b>IV.</b>	<b>RESULTS AND DISCUSSION .....</b>	<b>43</b>
A.	<b>GRAPHITE OXIDE .....</b>	<b>43</b>
B.	<b>GRAPHENE.....</b>	<b>44</b>
C.	<b>CARBON NANOFIBER BLANK SAMPLES. PRODUCTS CNF/Ni. ...</b>	<b>48</b>
D.	<b>3D GRAPHENE-CARBON NANOFIBER ARCHITECTURES   CONTAINING NICKEL .....</b>	<b>49</b>
1.	Aqueous Preparation .....	50
a.	<i>Graphite Oxide Precursor. Products: Graphene/Ni and       Graphene/CNF/Ni.....</i>	<i>51</i>

b.	<i>Graphene Precursor. Products: Graphene/Ni and G/CNF/Ni</i>	54
2.	<b>Dry Preparation</b>	59
a.	<i>Graphite Oxide Precursor</i>	59
b.	<i>Graphene Precursor</i>	61
E.	<b>OXIDIZED SAMPLES</b>	63
F.	<b>SURFACE AREA CHARACTERIZATION SUMMARY</b>	64
G.	<b>ELECTRICAL CHARACTERIZATION</b>	70
V.	<b>CONCLUSION</b>	81
A.	<b>MILESTONES</b>	81
B.	<b>SUGGESTED NEXT STEPS</b>	82
	<b>LIST OF REFERENCES</b>	85
	<b>INITIAL DISTRIBUTION LIST</b>	91

THIS PAGE INTENTIONALLY LEFT BLANK

## LIST OF FIGURES

Figure 1.	Schematic representation of an electric double layer capacitor. From [3].	3
Figure 2.	Power density versus energy density for common energy storage devices. From [6].	5
Figure 3.	Graphene (top left) is a honeycomb lattice of carbon atoms. Graphite (top right) can be viewed as a stack of graphene layers. Carbon nanotubes are rolled-up cylinders of graphene (bottom left). Fullerenes (C60) are molecules consisting of wrapped graphene through the introduction of pentagons on the hexagonal lattice. From [19].	7
Figure 4.	Carbon nanofibers at (a) low magnification and at (b) high magnification. Original image from work conducted at NPS.	8
Figure 5.	Stepwise production of graphite oxide. From [36]	14
Figure 6.	(a) Branson ultrasonic sonicator (b) Corning hotplate and stirrer (c) Hermle Z300 Centrifuge with 4x50 mL rotor. From [36]	16
Figure 7.	(a) Mixture of graphite powder with acids and $\text{KMnO}_4$ and $\text{H}_2\text{O}_2$ at the end of the reaction time (b) GO prior to being placed under vacuum (c) Nalgene vacuum desiccator with graphite oxide drying. From [36]	16
Figure 8.	(a) MKS Multi Gas Controller 647C (b) Thermo Scientific Lindberg Blue M tubular clamshell furnace. From [36].	17
Figure 9.	Stepwise production of graphene from GO.	17
Figure 10.	Stepwise production of graphene with nickel particle catalyst sites using the aqueous preparation method.	21
Figure 11.	Stepwise production of graphene with nickel particle catalysts using the dry preparation method.	23
Figure 12.	Stepwise production of G/CNF/Ni from graphene with Ni particle catalyst sites.	24
Figure 13.	Stepwise oxidation process.	25
Figure 14.	Stepwise production of CNF blank samples.	26
Figure 15.	(a) Micrometer film spreader used to evenly spread electrode slurry (b) Slurry with graphene as active material spread to 250 $\mu\text{m}$ .	28
Figure 16.	(a) Cole Parmer Laboratory Oven (b) MTI Corporation Precision Disc Cutter (c) Completed 15 mm diameter electrode.	29
Figure 17.	Stepwise electrode synthesis.	29
Figure 18.	NETZSCH STA 449 F3 Jupiter thermal analyzer on the right and the NETZSCH QMS 403C Aeolos spectrum analyzer on the left.	32
Figure 19.	Image of X-ray diffractometer. From [36].	34
Figure 20.	An image of the Zeiss SEM. From [36].	35
Figure 21.	NOVA 4200E surface area and pore size analyzer.	37
Figure 22.	Top view (46mm x 41.3 mm) (a) and side view (b) of constructed electrical test cell.	38
Figure 23.	Electrical characterization equipment (a) BK Precision 4011A 5MHz function generator (b) Global Specialties design and prototyping proto-	

	board PB-503 (c) Tektronix TDS2024B four channel digital storage oscilloscope.....	38
Figure 24.	Electrical test cell in construction: (a) acrylic base, (b) nickel foil current collector on inside surface of test cell, and (c) copper wire protruding from exterior surface of test cell.....	39
Figure 25.	Electrical test cell assembly schematic.....	40
Figure 26.	Capacitance measurement circuit schematic.....	41
Figure 27.	XRD peaks of GO. Note the primary peak (Miller index (002), has shifted from $\sim 25^\circ$ to $\sim 10^\circ$ .....	44
Figure 28.	XRD analysis of graphene.....	46
Figure 29.	Visual comparison of 15 mg of GO versus graphene.....	46
Figure 30.	SEM image of graphene.....	47
Figure 31.	SEM images of blank sample (nickel only) at (a) 16k and (b) 32k magnification before fiber growth.....	48
Figure 32.	SEM images of CNF blank sample (CNF/Ni) at (a) 4k and (b) 32k magnification after the fiber growth process.....	49
Figure 33.	SEM images of an aqueously prepared sample from GO precursor before CNF growth, G/Ni at (a) low magnification and at (b) high magnification. Note the nickel particles underneath the top graphene layer in (a).....	51
Figure 34.	SEM images of an aqueously prepared sample with GO precursor after CNF growth, G/CNF/Ni at (a) 4k and (b) 32k magnification.....	52
Figure 35.	SEM images of aqueously prepared graphene with nickel nanoparticles from a graphene precursor (G/Ni) at low magnification with (a) 1 wt% nickel loading and (b) 3 wt% nickel loading.....	54
Figure 36.	SEM images of aqueously prepared graphene with nickel nanoparticles from a graphene precursor (G/Ni) at high magnification with (a) 1 wt% nickel loading and (b) 3 wt% nickel loading.....	55
Figure 37.	SEM images of aqueously prepared graphene-CNF architecture containing nickel (G/CNF/Ni) from a graphene precursor at 4k magnification with (a) 1 wt% nickel loading and (b) 3 wt% nickel loading.....	56
Figure 38.	SEM images of aqueously prepared graphene-CNF architecture (G/CNF/Ni) containing nickel from a graphene precursor at 32k magnification with (a) 1 wt% nickel loading and (b) 3 wt% nickel loading. Note the nickel nanoparticle in (b).....	57
Figure 39.	SEM image of aqueously prepared graphene-CNF sample from a graphene precursor and 1 wt% nickel loading, G/CNF/Ni-1%. Note the CNF growth in between the sheets of exfoliated graphene.....	58
Figure 40.	SEM images of dry prepared graphene layers with nickel nanoparticles from a GO precursor (G/Ni) at (a) 16k and (b) 32k magnification. Note the nickel catalyst in (b).....	60
Figure 41.	SEM images of dry prepared graphene-CNF (G/CNF/Ni-3%) structure from a GO precursor at (a) 4k and (b) 32k magnification.....	61
Figure 42.	SEM images of dry prepared graphene samples with nickel nanoparticles from a graphene precursor, G/Ni at (a) 16k and (b) 32k magnification.....	62

Figure 43.	SEM images of graphene-CNF architecture prepared via the dry method with a graphene precursor, G/CNF/Ni at (a) 4k and (b) 32k magnification. ...	63
Figure 44.	TGA results of nickel oxidation procedure.....	64
Figure 45.	Surface area comparison between precursors and preparation methods with a constant nickel loading (3 wt%).....	66
Figure 46.	Surface area comparison for the aqueously prepared samples as a function of precursor, nickel loading and oxidation status. ....	68
Figure 47.	Surface area comparison for the CNF blank samples as a function of oxidation status. ....	69
Figure 48.	Full output waveform and normalized charge curves for (a) aqueously prepared G/CNF/Ni-1% (b) aqueously prepared G/CNF/NiO-1% .....	72
Figure 49.	Full output waveform and normalized charge curves for (a) aqueously prepared G/CNF/Ni-3% (b) aqueously prepared G/CNF/NiO-3% .....	73
Figure 50.	Full output waveform and normalized charge curves for (a) CNF/Ni (b) CNF/NiO and (c) pure graphene.....	74
Figure 51.	(a) Exponential curve fit of equation 3 and the (b) linear curve fit of equation 4 for the aqueously prepared G/CNF/Ni-3 wt% Ni. ....	75
Figure 52.	BET and specific capacitance summary. ....	76

THIS PAGE INTENTIONALLY LEFT BLANK

## LIST OF TABLES

Table 1.	Summary of electrical storage device requirements to supply a 100 kW directed energy weapon. ....	4
Table 2.	Separate syntheses for 3D graphene-CNF architectures with nickel.....	19
Table 3.	Settings used for x-ray diffraction runs to determine composition of nanopowder materials. ....	33
Table 4.	Summary of electrical characterization .....	75



THIS PAGE INTENTIONALLY LEFT BLANK

## LIST OF ACRONYMS AND ABBREVIATIONS

2D	Two-dimensional
3D	Three-dimensional
$\alpha\text{-Fe}_2\text{O}_3$	Hematite
Å	Angstroms
Ar	Argon
BET	Brunauer Emmett Teller
$\text{C}_2\text{H}_4$	Ethylene
CNF	Carbon Nanofiber
CV	Cyclic Voltammetry
DI	Deionized
EDLC	Electric Double Layer Capacitor
G	Graphene
GO	Graphite Oxide
$\text{H}_2$	Diatomic Hydrogen
$\text{H}_2\text{O}$	Water
$\text{H}_2\text{O}_2$	Hydrogen Peroxide
$\text{H}_2\text{S}$	Hydrogen Sulfide
$\text{H}_2\text{SO}_4$	Sulfuric Acid
$\text{H}_3\text{PO}_4$	Phosphoric Acid
keV	Kiloelectron Volt
KOH	Potassium Hydroxide
kV	Kilovolt
MnO	Manganese Oxide
$\text{MnO}_2$	Manganese Dioxide
mL	Milliliter
mm	Millimeter
MWNT	Mutli-walled Carbon Nanotube
$\text{N}_2$	Diatomic Nitrogen
$\text{Ni}(\text{NO}_3)_2 \cdot 6\text{H}_2\text{O}$	Nickel (II) Nitrate Hexahydrate
$\text{Ni}(\text{OH})_2$	Nickel Dihydroxide

NiO	Nickel Oxide
N-Methyl-2-pyrrolidone	NMP
O <sub>2</sub>	Diatomic Oxygen
SEM	Scanning Electron Microscope
Si	Silicon
SiC	Silicon Carbide
SCCM	Standard Cubic Centimeters per Minute
TiO <sub>2</sub>	Titanium Dioxide
Wt%	Weight Percent
XRD	X-Ray Diffraction
μm	Micrometer
Ω	Ohm

THIS PAGE INTENTIONALLY LEFT BLANK

## ACKNOWLEDGMENTS

This work would not have been possible with the help and dedication of many of my professors, peers, and family. I would like to personally thank Dr. Claudia Luhrs, my thesis advisor, for her kindness, professionalism, and unyielding willingness to do whatever she could to help her students. It has been a pleasure working with you over the course of this work. I would also like to thank Dr. Drago Grbovic who went well above and beyond in his efforts to help me in any way possible. Furthermore, I would like to thank Dr. Sebastian Osswald for generously allowing me to use some of his laboratory equipment and materials and Dr. Chanman Park for always being available to help with any lab work materials necessary.

Additionally, my experience with the entire Department of Mechanical and Aeronautical Engineering at NPS has been a delight. Each of the professors is more than willing to sacrifice their personal time to help the students succeed.

Next, I would like to thank my peers who have always been willing to lend a hand whenever necessary, whether that's help casting electrodes, using laboratory equipment, or interpreting capacitor charge curves. Specifically, I would like to mention LCDR Chris Daskam, LT Russell Canty, LT Jamie Cook, LT Ashley Maxson, LT Samuel Fromille, and Edwin Gonzalez. Thanks so much and good luck with each of your theses.

I would be remiss if I did not take a moment to thank my family: my wife Samantha, my oldest son Logan, and my youngest son Noah. Samantha has been able to hold the fort down while I've been ensconced in writing my thesis and I am so very grateful for her.

Finally, I would like to acknowledge my Lord, Jesus Christ, without whom none of this would be possible. "Every good and perfect gift comes from above ..." James 1:17.

THIS PAGE INTENTIONALLY LEFT BLANK

# **I. INTRODUCTION**

## **A. OVERVIEW**

This manuscript presents the ongoing efforts at the Naval Postgraduate School to develop carbon based electrode materials for use in state of the art energy storage devices. The novel synthesis of three-dimensional (3D) graphene (G)-carbon nanofiber (CNF) materials with nickel catalyst particles (G/CNF/Ni) and the construction of electrodes of the same for use in supercapacitors are the central focus of this study.

Typical materials used for energy storage include batteries, fuel cells, electrostatic capacitors and electric double layer capacitors (EDLC), also known as ultracapacitors or supercapacitors. Currently, no device can supply both high power and energy densities. Delivering such an energy storage method is the focus of much ongoing research with specific efforts invested in supercapacitors which do have an acceptable range of energy density combined with large values of power density. Additionally, the energy stored in supercapacitors can be accessed very quickly and they typically have significantly longer shelf and cycle lives than batteries, thus improving supercapacitor performance is a milestone that can expand Navy expeditionary capabilities.

## **B. ENERGY STORAGE TECHNOLOGY**

### **1. Capacitor Theory**

Capacitance is defined as the ability of a system to store an electric charge. Electrostatic capacitor charge storage is done by the physical charge storage on opposing electrodes, typically made of metal. Capacitor technology began in the late 18<sup>th</sup> century with the invention of the electric condenser, referred to as the “Leyden Jar” and known as the predecessor to the electrostatic capacitor. The principle of design and operation of the Leyden Jar and subsequent electrostatic capacitors is as follows: two metal surfaces (electrodes) separated at some small distance in air, vacuum, liquid, or on either side of a solid film. The media separating the electrodes is referred to as the dielectric and the capacitance per unit surface area of the electrodes depends on the properties of said

dielectric, which is characterized by its dielectric constant. Furthermore, specific capacitance,  $C$  (F/g), of a capacitor is given by Conway [1]:

$$C = \varepsilon_0 \varepsilon_r \frac{S}{D} \quad 1$$

where  $\varepsilon_0$  is the electric constant ( $8.854 \times 10^{-12}$  F/m),  $\varepsilon_r$  the relative dielectric constant,  $S$  is the specific surface area of the electrodes ( $\text{m}^2/\text{g}$ ), and  $D$  (m) is the separation between the electrode plates.

Capacitors are energy storage devices that can access and deliver their energy quickly. Capacitors are used in a wide variety of applications that have high power demand for short periods of time such as backup devices in electronic systems to maintain power during brief outages and in car audio systems to store energy for the amplifier to use on demand. Additionally, capacitors are used to supply large pulses of current for pulsed power applications such as lasers and are often employed for signal conditioning.

## 2. Electric Double Layer Capacitors (Supercapacitors)

Although many consider batteries and capacitors separate technologies, it is beneficial to examine them as part of the same continuum of energy storage technology, one that illustrates the transfer of electrons between electrode and electrolyte. Electrostatic capacitors, which store charge electrostatically on their electrodes would lie one end of the spectrum whereas batteries, which store energy via chemical reactions, would be located at the opposing end [2]. Supercapacitors, which could be placed in the mentioned continuum of energy storage in between electrostatic capacitors and batteries, differ from electrostatic capacitors by storing charge as an electric double layer at the interface between electrode and electrolyte. The electric double layer consists of ions which are dissolved in the electrolyte and are attracted to the equal but opposite charges on the electrode surfaces. This essentially creates two capacitors in series as demonstrated in Figure 1. Moreover, due to the extremely high values of specific surface area of electrode materials and the nanometer scale of the electric double layer, supercapacitors have energy densities that are often several orders of magnitude higher



than conventional electrostatic capacitors (Figure 2) [2]. This is further emphasized by examining equation 1. Supercapacitor electrode material tends to have specific surface areas two to three orders of magnitude greater than do electrostatic capacitors and thus a significant improvement upon specific capacitance.

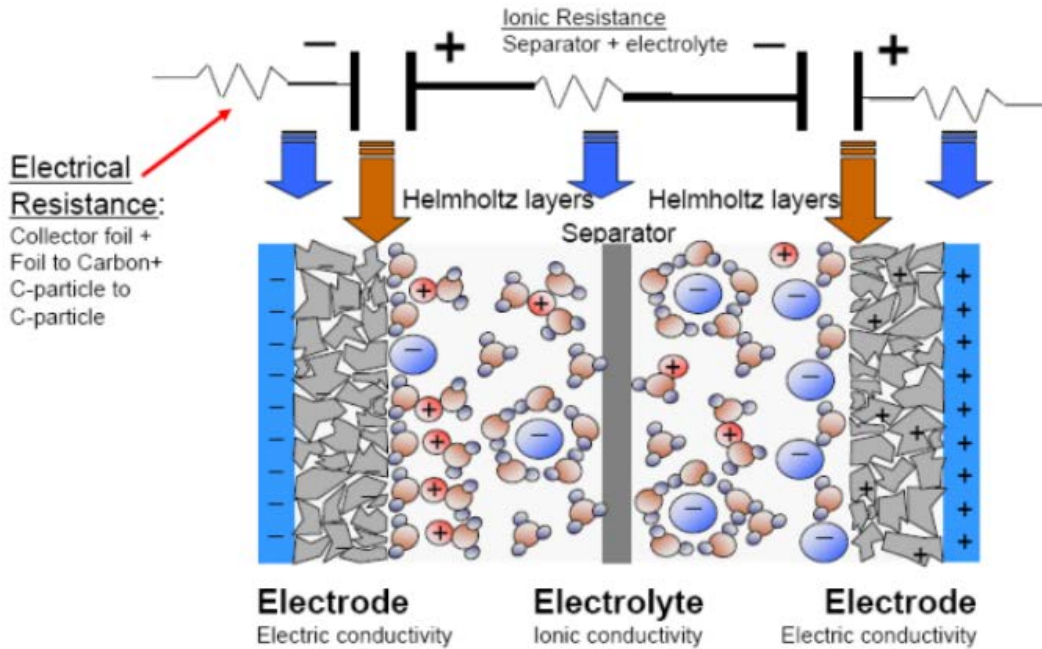


Figure 1. Schematic representation of an electric double layer capacitor. From [3].

Another step in the energy storage continuum of electrode/electrolyte electron transfer, a step further towards battery systems than electrostatic capacitors, is the redox type of faradaic charge transfer. This type of charge transfer may occur across the electric double layer and is referred to as pseudocapacitance by Conway [1] who goes on to state that pseudocapacitance is observed when fast, potential-dependent reactions occur, that become thermodynamically favorable in certain ranges of potential and produce capacitive charge/discharge characteristics. These types of faradaic charge transfers in supercapacitors tend to occur during the oxidation and reduction of a transition metal. In sum, the pseudocapacitive behavior just described may be combined with the electric double layer charge transfer mechanisms depicted above, creating a hybrid supercapacitor.

The discussion of the hybrid supercapacitor transitions into the central theme of this work: three-dimensional graphene-carbon nanofiber material syntheses for construction and evaluation as electrode materials in supercapacitors. This work evaluates the electrical characteristics of said electrode materials as a function specific surface area, nickel and carbon nanofiber loading, and pseudocapacitance behavior (hybrid supercapacitors).

Finally, similar to conventional electrostatic capacitors, supercapacitors have a wide variety of applications, which include power capture and supply, power quality, and backup, safety, and low maintenance applications. Hybrid energy systems will soon combine high energy density systems, such as batteries, with those of high power density features, such as supercapacitors. The significant advantage of this hybrid system is that because the batteries would provide the normal, steady state load and supercapacitors would provide the extra power necessary for peaks and surges, the battery system will not be exhausted by being stressed to limit of its power capabilities. This will result in longer battery lifetimes [4]. Examples of such hybrid energy systems would be passenger cars driven in settings which accelerate and decelerate frequently where the battery would maintain the load during normal driving operations and supercapacitors would deliver power required for the “stop and go” driving [4, 5]. For a Naval application of supercapacitors, one need only to examine the ongoing directed energy weapon research for use in cruise missile defense, which requires hundreds of kilowatts of power. Table 1 is a summary of electrical storage device requirements to supply 100 kW to a directed energy weapon using Figure 2 as a reference.

Table 1. Summary of electrical storage device requirements to supply a 100 kW directed energy weapon.

Component	Power density (W/kg)	Energy density (Wh/kg)	Mass required (kg)	Time energy available (s)
Electrostatic capacitor	$10^7$	$10^{-1}$	0.01	$36 \times 10^{-6}$

Component	Power density (W/kg)	Energy density (Wh/kg)	Mass required (kg)	Time energy available (s)
Supercapacitor	$10^5$	1	1	$3.6 \times 10^{-3}$
Battery	$10^2$	$10^2$	1000	360

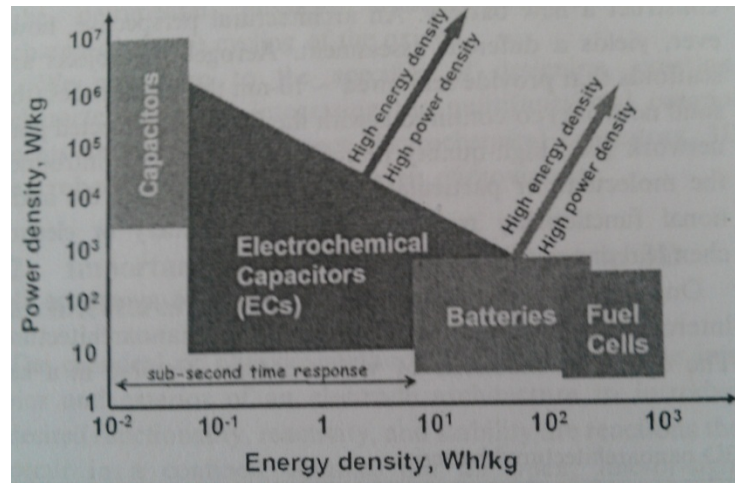


Figure 2. Power density versus energy density for common energy storage devices. From [6].

### 3. Carbon Electrode Technology

Apart from merely examining supercapacitor behavior, this manuscript specifically investigates the novel synthesis of carbonaceous materials for use as electrodes in supercapacitors. From the significant amount of research performed on carbon electrode materials [1, 7–9], Hall et al. [2] describes four primary requirements for carbon materials employed as supercapacitor electrodes: high surface area, low electrical resistance, good polarizability and controllable pore size. Furthermore, due to its ability to exist in many forms (powders, fibers, foams, and composites), processing ease, low cost, thermal stability, and relatively high specific surface area, carbon is an element uniquely suited to supercapacitor electrode production [8].

There are many carbon materials which have been employed as electrode materials in supercapacitors such as activated carbons, carbon nanotubes, carbon nanofibers, graphene, carbide-derived carbons, template-derived carbons, and polymer-derived carbons [2].

*a. Graphene and Three-dimensional Architecture*

While there are many possible carbonaceous material options for use as electrode materials, the focus of this study is the application of carbon nanofibers within a graphene matrix to construct a three-dimensional architecture. The intent is to grow carbon nanofibers from within and directly upon the graphene sheets to not only physically exfoliate the graphene layers but also provide electrical and ion connectivity between the sheets and prevent their collapse when an electrode paste is made and laid in the current collector surface.

The first aspect in the proposed three-dimensional structure is the graphene base material. Graphene is a one-atom-thick planar sheet of sp<sup>2</sup>-bonded carbon atoms that are densely packed in a honeycomb crystal lattice that has attracted significant attention because of its two dimensional (2D) structure, excellent chemical and physical properties [10–12], and wide potential applications in nanoelectronics, energy storage and conversion, chemical and biological sensors, composite materials and biotechnology [10, 12, 13] as documented by Li and Shi [14]. Three-dimensional graphene (Figure 3), however, provides several advantages over the 2D version such as high specific surface area, fast mass and electron transport kinetics, and strong mechanical strengths [14] and is required for applications of graphene-based materials in energy, environment, sensing and biological fields [15–18].

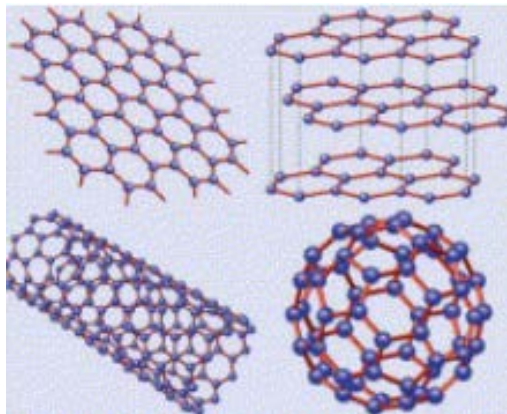


Figure 3. Graphene (top left) is a honeycomb lattice of carbon atoms. Graphite (top right) can be viewed as a stack of graphene layers. Carbon nanotubes are rolled-up cylinders of graphene (bottom left). Fullerenes (C60) are molecules consisting of wrapped graphene through the introduction of pentagons on the hexagonal lattice. From [19].

The construction of 3D graphene has been widely studied and many methods for developing 3D graphene architectures are documented in literature such as the gelation of graphite oxide (GO) [13], centrifugal evaporation-induced assembly of GO [20], hydrothermal reduction of GO [17, 21], combining the assembly of GO on the surface of *E. coli* with a directional freezing technique [22], and optical disc recording technology irradiating GO affixed to the top of a LightScribe enabled DVD media disc [23, 24] as well as many others. In regard of applications, Li and Shi [14] summarize the main applications of 3D graphene structures, which include supercapacitors, stretchable electronics, and hydrogen storage, amongst others, with the goal of this manuscript being the applicability of three-dimensional graphene structures for use in supercapacitors.

Transitioning to carbon nanofibers and their role in the proposed 3D architecture of this thesis, the history of CNF goes back more than a century when a patent published in 1889 [25] reports carbon filaments grown from carbon-containing gases using a metal crucible as—potentially unintentionally—the catalyst. Carbon nanofibers are cylindrical nanostructures with graphene layers arranged as stacked cones, cups or plates and were first a major focus of research in the 1990s [26]. Carbon

nanofibers have been shown to be an ideal material for application in supercapacitors because they generally demonstrate an open mesoporous structure and possess good conductivity along the fiber axis [2].

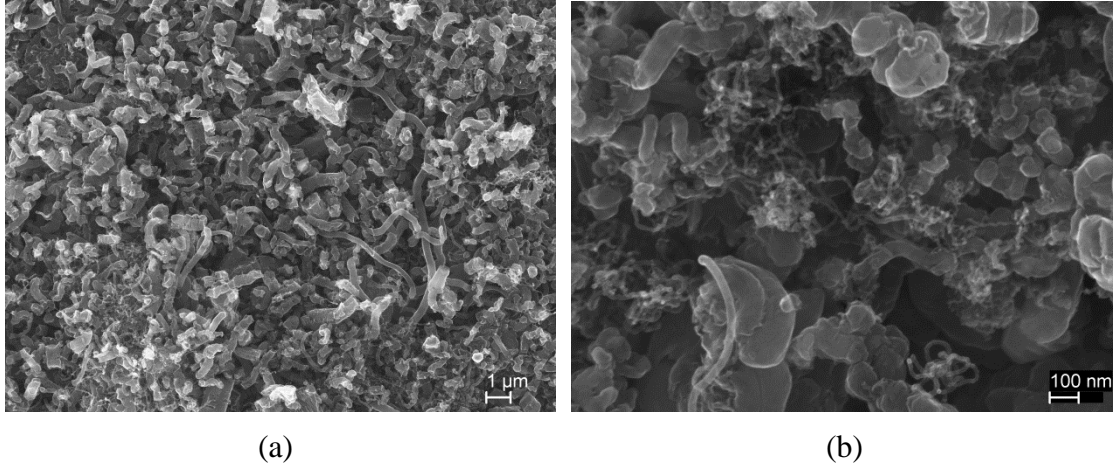


Figure 4. Carbon nanofibers at (a) low magnification and at (b) high magnification. Original image from work conducted at NPS.

Carbon nanofibers are employed in this work by being grown within the graphene matrix directly upon the graphene layers to increase both the electron and ion connectivity between graphene layers and create a three-dimensional structure for use as electrode materials in supercapacitors. This work is unique in that the CNF are grown directly upon the graphene *in situ* as opposed to dispersing the carbon nanofibers with graphene sheets or GO in an aqueous solution [27, 28]. The method employed in this study has the advantages of simpler synthesis processes and better carbon nanofiber distribution.

Fan et al. [27] report a strategy to construct a carbon nanofiber and graphene sandwich, which possesses superior specific surface area ( $612 \text{ m}^2/\text{g}$ ) and specific capacitance ( $385 \text{ F/g}$ ) by means of chemical vapor deposition (CVD). In order to create the CNF-graphene sandwich, Fan et al. [27] first synthesized and exfoliated graphite oxide via ultrasonication. Carbon nanotubes were then prepared via catalytic

decomposition of propylene and were ultrasonicated in GO suspension to create the CNF-graphene sandwich. In this approach, the carbon nanotubes were grown separately and dispersed within the graphene matrix via aqueous suspension.

Separately, Kwon et al. [28] detail the fabrication of nanostructured hybrid materials in which CNF are intercalated between graphene sheets with the additional aspect of having the carbon nanofibers impregnated with  $\text{MnO}_x$  nanocrystals. The method of material synthesis followed for this architecture is similar to that described previously by Fan et al. [27], the carbon nanofibers were grown separately from the graphene sheets and were later distributed via aqueous dispersion with graphite oxide.

Both of the above syntheses create 3D graphene-CNF architectures but neither does so in a manner similar to that which is detailed in this work. The structure preparation in this study is novel because the growth of the carbon nanofibers occurs directly upon the graphene *in situ*. This allows for more uniform carbon nanofiber distribution leading to more complete graphene exfoliation and better electrical and ion connectivity between graphene layers.

#### **4. Use of Metal Oxides in Supercapacitors**

The last aspect of the material synthesized for the use in electrodes created in this work is the application of metal oxides in supercapacitors. Transition metal oxides have been studied for pseudocapacitive charge storage. As described *a priori*, pseudocapacitors rely on fast and reversible faradaic reactions for charge storage and, combined with electric double layer capacitive behaviors, form a hybrid supercapacitor. Furthermore, research has indicated that the capacitance of faradaic electrodes exceeds that of nonfaradaic charge storage [28]. To that end, much research has been documented on the nanostructured metal oxides such as titanium dioxide ( $\text{TiO}_2$ ) [29], nickel oxide ( $\text{NiO}$ ) [30, 31], nickel dihydroxide ( $\text{Ni(OH)}_2$ ) [32], manganese dioxide ( $\text{MnO}_2$ ) [28, 33], and iron oxide ( $\alpha\text{-Fe}_2\text{O}_3$ ) [34].

This work is unique also in the method by which the pseudocapacitance behavior was attained. Nickel catalyst sites were used to grow the CNF within the graphene matrix for this study. Following fiber growth, the nickel particles remained in the 3D

architecture (as opposed to being filtered out or etched away with acid baths) and were subsequently oxidized to utilize the faradaic redox reaction inherent to pseudocapacitance. This varies from other works which impregnate the carbon nanofibers with nanoparticles of the transition metal via calcination followed by carbonization [28] or the aqueous dispersion method [34]. The method proposed by this study is relatively low cost, simple to synthesize, and the process can be easily manipulated to control variables of interest such as nickel loading. Moreover, it produces highly dispersed NiO nanoparticles, which promotes changes in electrical properties in a homogenous fashion across the sample.

### **C. THESIS OBJECTIVES**

The general scope of this thesis is centered on the development of three-dimensional graphene-carbon nanofiber architectures for use as electrode materials in supercapacitors. In particular, this work aimed to design a nanohybrid that combined the potential of graphene sheets with the characteristics of carbon nanofibers and transitional metal oxides to produce a material with superior specific surface area and specific capacitance.

Moreover, both graphene and hybrid type nanostructures have been prepared by diverse routes, but no attempts have been made to design the structures such that the carbon nanofibers are grown directly upon the graphene sheets *in situ*. Carbon nanofibers, grown from nickel catalyst sites, are intercalated amongst the graphene sheets in order to more completely exfoliate the graphene as well as provide a pathway for electrons between the sheets thus increasing the electrical conductivity of the architecture. Finally, by utilizing nickel catalysts for CNF growth, the resulting three-dimensional structures can then be oxidized to make use of the pseudocapacitance behaviors described above.

The thesis is divided into five chapters that present in a systematic way the protocols designed for materials synthesis and construction, beginning with graphite oxide and transitioning through to completion, 3D graphene-CNF architecture containing nickel and nickel oxide. The methods employed to characterize material composition,



crystalline structure, microstructure, specific surface area, and electrical properties are discussed along with the results of the same. The manuscript then summarizes the milestones achieved and compares the data with those previously published for similar electrochemical systems. Suggested next steps to further the research conclude this thesis.

#### **D. HYPOTHESIS**

- The combination of graphene with carbon nanofibers grown in between sheets will provide a three-dimensional architecture which could be used as electrode material in supercapacitors.
- Without the removal of the catalyst, the resulting 3D structures G/CNF/Ni composites will present improved specific capacitance values over either graphene or CNF individual components.
- Oxidation of the nickel particles in the 3D graphene-CNF matrix will increase the capacitance values of the three-dimensional architecture due to the formation of G/CNF/NiO.

THIS PAGE INTENTIONALLY LEFT BLANK

## II. EXPERIMENTAL METHODS

A variety of equipment and techniques were used to create the 3D graphene-CNF electrode architectures. This and the following chapter will summarize the steps followed for the fabrication protocols, the operational principles for the techniques, and conditions of analysis.

The three-dimensional structures consisted of layers of graphene with carbon nanofibers intergrown upon them. The sample fabrication section will begin with the protocols to generate graphene from graphite oxide followed by the inclusion of a nickel catalyst in between graphene layers to continue with carbon nanofiber growth upon said layers. An oxidation step to create a graphene-carbon nanofiber nickel oxide architecture will close out the sample synthesis and electrode generation of the same will conclude Chapter II.

### A. GRAPHITE OXIDE PRODUCTION

The first step in the creation of the 3D graphene-CNF structure was the generation of graphite oxide (Figure 5). GO was primarily used in this work as a precursor for graphene and was produced based on a further modification to the modified Hummer's method reported by Marcano *et al.* [35] as detailed by Maxson [36] who described the motivation for using commercial graphite nanopowder (Sigma-Aldrich, < 20 nm) instead of commercial graphite flakes for the production of GO.

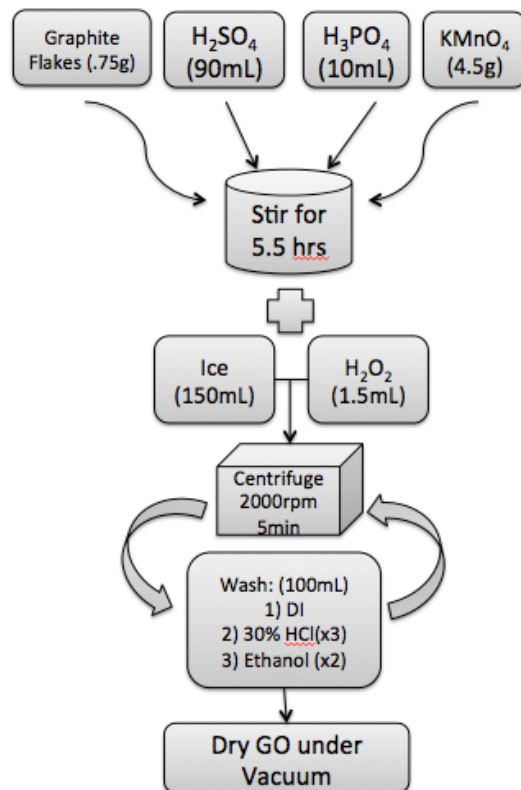


Figure 5. Stepwise production of graphite oxide. From [36]

The controlled oxidation of graphite started by adding a mixture of 90 mL  $\text{H}_2\text{SO}_4$  (Sigma-Aldrich ACS reagent 95.0–98.0%) to 10 mL  $\text{H}_3\text{PO}_4$  (Sigma-Aldrich ACS reagent,  $\geq 85$  wt. % in  $\text{H}_2\text{O}$ ) to 750 mg of graphite flakes (Aldrich graphite flakes, particle size +100 mesh,  $\geq 75\%$  min). The solution was then sonicated for one minute using a Branson ultrasonic model 2510R-MTH sonicator (Figure 6(a)).

Following sonication, the mixture was placed on a Corning hotplate and stirrer (AC input 120 V, 4"x5") (Figure 6(b)), where it was stirred at 240 rpm to ensure the mixture remained a homogeneous dispersion. As the solution was being stirred, 4.5 g of  $\text{KMnO}_4$  (Mallinckrodt Baker Inc., ACS reagent, 3227-01, 500 g) were added to the mixture. The solution then continued stirring for five and a half hours.

Upon completion of the five and a half hour wait, ice cubes made from 150 mL of deionized (DI) water were added to the solution one ice cube at a time and were allowed to dissolve in the solution, at which time 1.9 mL of  $\text{H}_2\text{O}_2$  (Sigma-Aldrich hydrogen

peroxide solution, contains inhibitor, 30 wt. % in H<sub>2</sub>O, ACS reagent) was added drop wise to the solution and the mixture was allowed to stir for another hour and settle overnight (Figure 7(a)).

After allowing the mixture to settle overnight, the excess liquid was siphoned from the top of the solution the following day. The remaining dispersion was placed evenly into two 50 mL centrifuge tubes. The mixture was then centrifuged for five minutes at 2000 rpm, in a Hermle Z300 Centrifuge (Figure 6(c)) fitted with a 4 x 50 mL rotor.

After the mixture had been centrifuged, the supernatant was removed from the top and replaced with 20 mL of deionized water. The centrifuge tubes were then shaken to homogenize the solution and replaced in the centrifuge which was again set at 2000 rpm for five minutes. The excess liquid was again removed and replaced this time with 20 mL of 30% HCl solution (prepared from Sigma-Aldrich hydrochloric acid ACS reagent, 37%) as opposed to DI water. The solution was again shaken to homogenize the solution before being centrifuged. The washing step employing 30% HCl solution was repeated as necessary until the supernatant contained no remnant MnO<sub>2</sub> as indicated by transparency. The final washing step was performed twice with 20 mL of ethanol (Sigma-Aldrich, ACS reagent,  $\geq 99.5\%$ , 200 proof, absolute).

Upon completing the final washing step, the supernatant was removed and the remaining slurry was poured into a small dish (Figure 7(b)) for drying in a Nalgene vacuum desiccator (with stopcock, overall H 262 mm). A pump was employed to draw a vacuum on the desiccator and the resultant graphite oxide was dried overnight until the light brown color shown in Figure 7(c) was obtained.

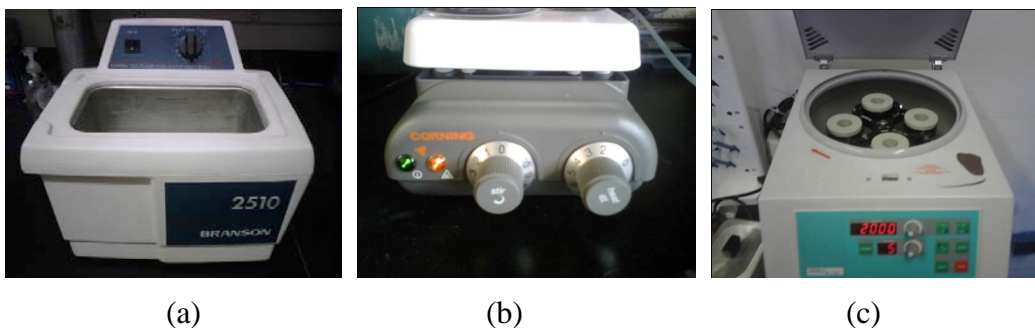


Figure 6. (a) Branson ultrasonic sonicator (b) Corning hotplate and stirrer (c) Hermle Z300 Centrifuge with 4x50 mL rotor. From [36]

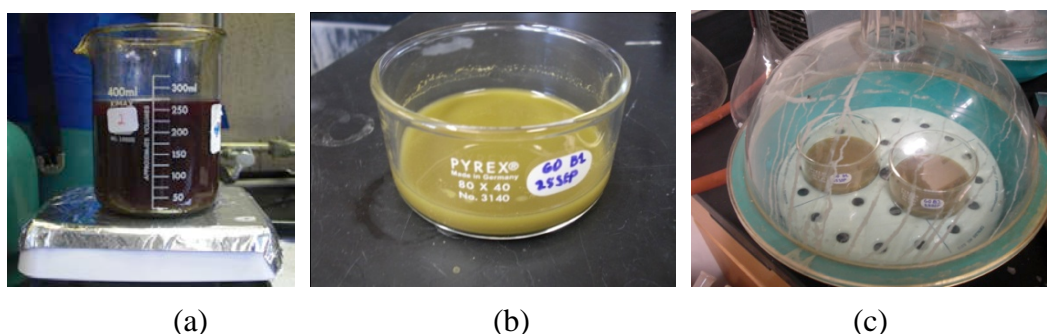


Figure 7. (a) Mixture of graphite powder with acids and  $\text{KMnO}_4$  and  $\text{H}_2\text{O}_2$  at the end of the reaction time (b) GO prior to being placed under vacuum (c) Nalgene vacuum desiccator with graphite oxide drying. From [36]

## B. GRAPHENE PRODUCTION

Following GO production, the next step performed in the construction of 3D graphene-CNF architecture was the fabrication of graphene, which was used as the base material from which the CNF grew. The GO was thermally exfoliated after it was vacuum dried and hand crushed in a mortar and pestle for 15 minutes. For each exfoliation, 200 mg of GO were measured and spread evenly along the bottom of an alumina boat (Sigma-Aldrich, coors combustion boat, high-alumina, 70 L x 14 W x 10 mm H, 5 mL capacity). The ceramic boat was then sealed inside a one-inch diameter quartz tube. Next, the quartz tube containing the GO was flushed with nitrogen at 500 standard cubic centimeters per minute (SCCM) for 20 minutes to establish an inert environment. The inert environment was accomplished while the quartz tube remained outside of the clamshell tubular furnace. Gas flow was regulated using a MKS multi-gas

controller 647C (4 channels) (Figure 8(a)). The Thermo Scientific Lindberg Blue M 1200C clamshell tubular furnace (Figure 8(b)) was preheated to 900°C while flowing the inert environment.

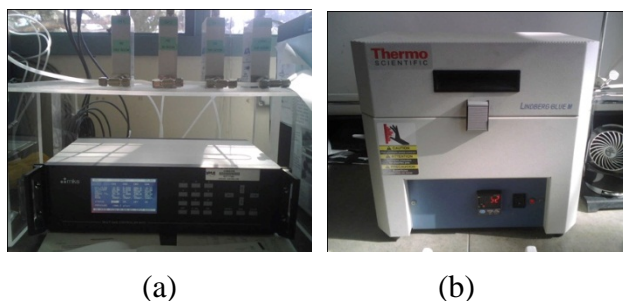


Figure 8. (a) MKS Multi Gas Controller 647C (b) Thermo Scientific Lindberg Blue M tubular clamshell furnace. From [36].

After the 20 minute purge, N<sub>2</sub> flow was lowered to 15 SCCM. The quartz tube was then placed inside of the furnace, the temperature was set to 800°C and the GO was allowed to exfoliate for 10 minutes. Following exfoliation, the quartz tube was removed from the furnace and the graphene was allowed to cool to room temperature while maintaining nitrogen at 15 SCCM. Typical mass yield of graphene was 30–35% the mass of GO used for exfoliation (i.e., 200 mg of GO would yield approximately 65 mg of graphene). The stepwise production of graphene from GO is shown in Figure 9.

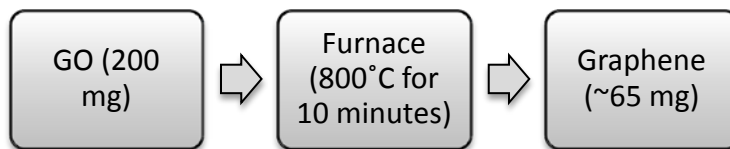


Figure 9. Stepwise production of graphene from GO.

### C. SYNTHESIS OF CARBON NANOFIBER ARCHITECTURES INTO GRAPHENE LAYERS

Following the exfoliation of graphene, the next step in the creation of graphene-CNF structures was to grow the carbon nanofibers into the graphene layers. Nickel

particles were used as catalyst sites for the growth of CNF. Nickel was produced by reducing nickel(II) nitrate hexahydrate ( $\text{Ni}(\text{NO}_3)_2 \cdot 6\text{H}_2\text{O}$ ) via a reaction with urea as reported by Zea et al., Luhrs et al., and Phillips et al. [37–39], known as Reduction Expansion Synthesis (RES). The reduction of nickel salt to obtain nickel particles was used as opposed to commercial nickel nanoparticles because the reduction process allowed for better nickel particle size and distribution control. Commercial nickel nanoparticles have a wide variety of particles sizes ranging from nano to micron. This work required homogeneous particle size distribution to ensure uniform carbon nanofiber growth. The reduction of nickel salt provided by RES methodology also permitted better distribution of nickel particles than commercial powders did. In order to adequately disperse the particles in between the graphene sheets and therefore grow fibers within the same, RES presents advantages that are more evident when samples characterization is performed, as will be discussed in the following chapters.

Two different approaches were used for depositing nickel particles into the graphene layers: an aqueous preparation and a dry preparation method. Detailed descriptions of each method follow. Additionally, in the case of the aqueous preparation method, two different weight percentages were employed for the nickel inclusion in the graphene layers to examine effects of diverse amounts of Ni/NiO/CNF growth on both surface area and conductivity: 1 wt% and 3 wt%. Moreover, for each preparation method, two methods were used to disseminate the nickel catalysts within the graphene matrix: using GO precursor directly or employing previously exfoliated graphene.

The first preparation of graphene-CNF structures began with 3 wt% nickel loading for both the dry and aqueous approaches for both the GO and graphene precursors. Subsequently, the aqueous samples displayed more potential for desirable electrical performance based upon superior specific surface area values, and as such further experimentation followed with the aqueous approach only (Table 2).



Table 2. Separate syntheses for 3D graphene-CNF architectures with nickel.

Method	Precursor	Nickel Loading
Aqueous Preparation	GO	3%
	Graphene	1%
		3%
Dry Preparation	GO	3%
	Graphene	3%

### 1. Aqueous Preparation

This method was employed with the motivation of uniformly dispersing the nickel particles within the graphene sheets, based on the idea that the nickel salt will be easily dissolved in the aqueous dispersion and graphene sheets were light enough to be suspended in the same bath as individual entities. Furthermore, two methods were employed to disperse the nickel particle catalysts within the graphene matrix within the aqueous preparation method: using the GO precursor directly and starting with previously exfoliated graphene. Both GO and graphene were used as separate precursors in the aqueous preparation method in an attempt to maximize surface area of the resulting 3D graphene-CNF structure. Lastly, as the aqueous prepared samples had superior surface area performance when compared to the dry method, the nickel loading was also altered between two values, 1 wt% and 3 wt%. Nickel loading was varied in an effort to examine the effects on surface area and specific capacities.

#### a. Graphite Oxide Precursor

Though both GO and previously exfoliated graphene were used as precursors for the nickel particle deposition, graphite oxide was the first method employed. Additionally, the GO precursor had inferior surface area performance when compared to the graphene precursor and as such was prepared only with 3 wt% nickel loading. The nickel particle addition to the graphene matrix was done through the

reduction of  $\text{Ni}(\text{NO}_3)_2 \cdot 6\text{H}_2\text{O}$  via reaction with urea (RES methodology) at a weight ratio of urea to nickel salt of 7:1. Urea was used to simultaneously reduce the nickel salt to nickel particle and exfoliate the GO [37–39].

Aqueous synthesis with a GO precursor began by weighing 72.8 mg urea and 10.4 mg nickel salt. This would yield 2.1 mg of nickel nanoparticles after the reduction, which is 3 wt% of 70 mg, the expected yield of graphene following exfoliation of 200 mg of GO. Both the urea and the nickel salt were then dissolved in 10 mL deionized water. Next, 200 mg of GO was measured and added to the solution and the entire solution was sonicated for 30 minutes. Following sonication, the solution was dried using a Corning hotplate and stirring rod. The temperature was maintained at approximately 60°C while drying and the stirring rate were adequate to ensure complete mixing during the drying process.

After the solution was dried, the mixture was placed into a ceramic boat and sealed in a one-inch diameter quartz tube outside of the clamshell tubular furnace while the furnace was preheated to 900°C. A  $\text{N}_2$  purge of 500 SCCM was applied for 20 minutes to establish an inert environment. The  $\text{N}_2$  flow was then reduced to 15 SCCM, the quartz tube containing the sample was placed inside the furnace, the temperature was lowered to 800°C, and 10 minutes were allowed to elapse. Next, the quartz tube was removed from the furnace and allowed to cool to room temperature while maintaining nitrogen flow at 15 SCCM. This method of preparing graphene sheets with nickel particle catalyst sites typically yields 3 mg of final product for every 20 mg of GO precursor while the use of urea combined with high temperature allows the simultaneous reduction of nickel salt and exfoliation of graphite oxide.

#### ***b. Graphene Precursor***

Graphene sheets with nickel catalyst sites were also prepared using a previously exfoliated graphene precursor. These samples were synthesized in a similar manner to that of the GO precursor discussed above; however, one key difference did exist: the amount of nickel loading. The nickel loading was varied between 1 wt% and 3 wt% in an effort to examine the effects on surface area and specific capacities. The

aqueous prepared sample with graphene precursor demonstrated superior specific surface area values when compared to the other methods and as such the further experimentation (varied nickel loading and oxidation) was performed on these samples only.

The first step in creating a graphene matrix intercalated with nickel nanoparticles via the aqueous method with a graphene precursor was measuring the nickel (II) nitrate hexahydrate and urea. For the 3 wt% loading scenario, 4.5 mg of nickel salt and 31.5 mg of urea (for 0.9 mg of nickel particles following reduction) were added to 10 mL of DI water. For the case of the 1 wt% nickel loading, 1.5 mg of nickel salt and 10.5 mg of urea were employed (for 0.3 mg of nickel particles following reduction). For either loading scenario, after the nickel salt and urea were mixed in the 10 mL of deionized water, 30 mg of graphene were added to the solution that was then sonicated for 30 minutes.

Following sonication, the drying process and the nickel salt reduction protocol were exactly the same as detailed for the GO precursor. Typical yields using this method were 3 mg nickel doped graphene for every 4 mg graphene. The stepwise production of graphene with nickel particle catalysts using the aqueous preparation method is shown in Figure 10.

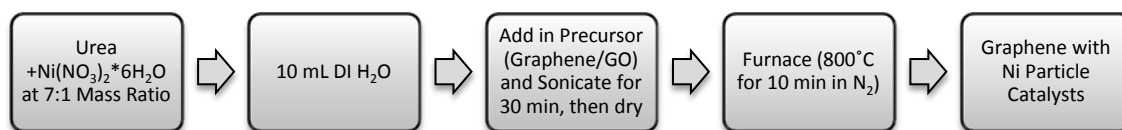


Figure 10. Stepwise production of graphene with nickel particle catalyst sites using the aqueous preparation method.

## 2. Dry Preparation

Similarly to the aqueous preparation synthesis, both GO and graphene were used as precursors in the dry preparation method in an attempt to maximize surface area of the resulting graphene-CNF architecture; however, only 3 wt% nickel loading was

employed in the dry synthesis for either precursor. Upon initial characterization of the 3 wt% nickel loaded dry and aqueously prepared architectures, it was discovered the aqueous preparation method had superior surface area performance, and, as such, no further modification to the dry synthesis was performed.

*a. Graphite Oxide Precursor*

As detailed in the aqueous preparation method section, two methods were employed to disseminate the nickel particles within the graphene layers: beginning with the GO precursor and beginning with previously exfoliated graphene. The first to be detailed is the sample preparation involving the GO precursor.

The first step in creating a graphene matrix intercalated with nickel nanoparticles was the mixture of  $(\text{Ni}(\text{NO}_3)_2 \cdot 6\text{H}_2\text{O})$  and urea. A weight ratio of urea to nickel salt of 7:1 was utilized in the dry preparation method in order to achieve the desired reduction of nickel salt to nickel particles.

Dry preparation using GO as a precursor synthesis began by weighing out 72.8 mg of urea and 10.4 mg of nickel salt based upon 3 wt% nickel loading (yielding 2.1 mg following reduction, which is 3 wt% of 70 mg expected yield of graphene). Similar to the aqueous preparation, the nickel salt and urea masses were added based on the expected yield of 30–35% graphene during the exfoliation process. The nickel salt and urea were then crushed together to homogenize the mixture using a mortar and pestle. Following crushing, 200 mg of GO were measured and added to the mortar where the entire mixture was crushed for fifteen additional minutes.

Following crushing, the same procedure described in the aqueous preparation was employed to simultaneously reduce the nickel salt and exfoliate the graphite oxide via reaction with urea at high temperatures in the clamshell tubular furnace. Upon completion of the dry preparation method with GO precursor, a typical yield would be 3 mg graphene intercalated with nickel defect sites for each 20 mg of GO employed.

### ***b. Graphene Precursor***

The preparation of graphene sheets with nickel catalyst sites via the dry method using previously exfoliated graphene as a precursor varied little from the method employing GO as a precursor. The first step in the synthesis was to measure out 4.5 mg of nickel salt and 31.5 mg of urea (to achieve a 3 wt% nickel loading-0.9 mg of nickel nanoparticles following reduction) and crush the two using a mortar and pestle until a homogeneous paste was attained. Next, 30 mg of graphene was added to the mortar where the entire mixture was crushed for 15 additional minutes.

Following the sample mixture, the nickel salt reduction at high temperature in the clamshell tubular furnace was performed identically as described previously. This method for producing graphene interlaced with nickel particles typically would yield 3 mg return for 4 mg graphene. The stepwise production of graphene with nickel particle catalysts using the aqueous preparation method is shown in Figure 11.

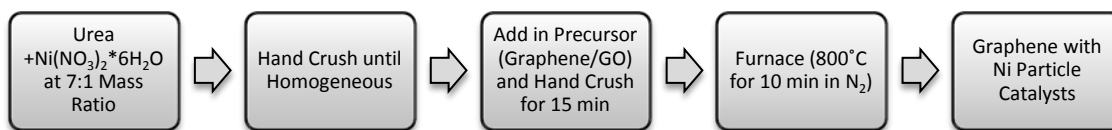


Figure 11. Stepwise production of graphene with nickel particle catalysts using the dry preparation method.

### **3. Carbon Nanofiber Growth**

After exfoliating the graphite oxide and intercalating nickel particle catalyst sites, the next step in the architecture synthesis was to grow the carbon nanofibers from the nickel sites. The identical growth process was executed for all samples regardless of method by which the nickel particles were dispersed among the graphene sheets or nickel loading.

The first step in the CNF growth protocol is to inert the atmosphere in which the fibers are grown. This was accomplished by placing the graphene sample with nickel

catalyst particles in a ceramic boat within a one-inch diameter quartz tube and flushing the tube with N<sub>2</sub> at 15 SCCM for one hour. The second step in the growth is the reduction step that is accomplished by placing the quartz cylinder containing the graphene sample inside the furnace and establishing a temperature of 350°C. An Ar/H<sub>2</sub> mixture at a ratio of 98:2% was then passed through the sample at 20 SCCM for 30 minutes. This was done to completely reduce the sample environment and ensure no O<sub>2</sub> remained, including any oxygen that may have previously reacted with the nickel particles forming NiO.

The next step in the CNF growth protocol was the low temperature growth. This was executed by applying a gas environment consisting of N<sub>2</sub> at 30 SCCM, C<sub>2</sub>H<sub>4</sub> at 42 SCCM, and O<sub>2</sub> at 20 SCCM. These gases were administered at 350°C for 15 minutes to establish a carbon shell around the nickel defect sites in the graphene. After 15 minutes had elapsed at 350°C, the penultimate step commenced: high temperature growth. The furnace temperature was increased to 550°C and the high temperature growth stage was allowed 45 minutes to complete. The CNF grew up from the graphene base material displacing the nickel particles away from the graphene during the high temperature growth step. The final stage in CNF growth was cooling the specimen in an inert environment. This was accomplished by eliminating the O<sub>2</sub> and the C<sub>2</sub>H<sub>4</sub> from the gas purge and subsequently lowering the N<sub>2</sub> flow to 15 SCCM. The graphene-CNF sample inside of the quartz tube was then removed from the furnace and allowed to cool to room temperature. The stepwise production of graphene-CNF structures with nickel from graphene with nickel particle catalysts is shown in Figure 12.

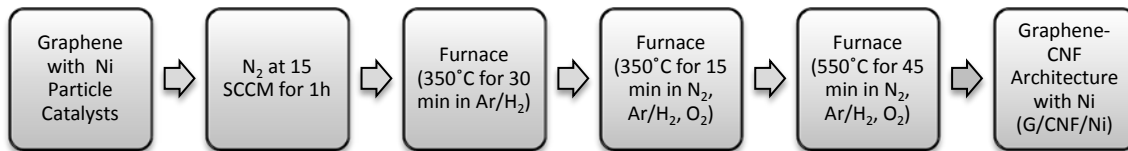


Figure 12. Stepwise production of G/CNF/Ni from graphene with Ni particle catalyst sites.

#### 4. Oxidation Process

The last step in the synthesis of 3D graphene-CNF structures with nickel was the oxidation of the Ni ( $\text{Ni} \rightarrow \text{NiO}$ ). The nickel in these samples was oxidized in an attempt to utilize the pseudocapacitive effects of the faradaic redox reactions involving a transition metal oxide. Additionally, the oxidized samples were compared with those not oxidized in an effort to encapsulate the effects of the oxidation on the graphene-CNF matrix.

Thermogravimetric analysis (TGA) was performed to determine the temperature at which nickel oxidation would be maximized and CNF burn off would be minimized in the previously synthesized graphene-CNF structures. This analysis, which is detailed in Chapter IV, yielded 400°C as the ideal oxidation temperature.

Following TGA to determine the appropriate oxidation temperature, oxidation synthesis commenced by weighing out the graphene-CNF containing nickel sample and placing it into a ceramic boat into a one-inch diameter quartz tube. The quartz tube containing the specimen was then placed into the furnace where an oxidant environment was established by purging the sample with a 4:1 ratio of  $\text{N}_2:\text{O}_2$  (12 SCCM:3 SCCM). Next, the furnace temperature was set to 400°C. Once the furnace reached the desired temperature, 30 minutes were allowed to elapse while maintaining a constant temperature. The furnace was then turned off, the sample removed from the furnace, and the sample allowed to cool to room temperature while maintaining the oxidant environment. The gas purge was removed once the sample reached room temperature. The stepwise oxidation procedure is shown in Figure 13.

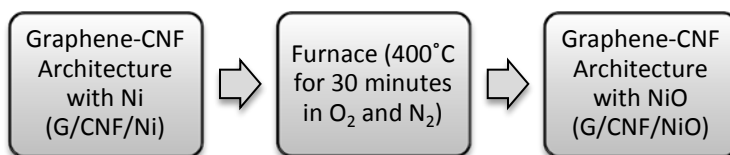


Figure 13. Stepwise oxidation process.

#### D. CARBON NANOFIBER BLANK SYNTHESIS

After complete synthesis of the graphene-CNF architecture containing either nickel or nickel oxide, a carbon nanofiber blank sample was prepared for comparison. A CNF sample was generated from nickel catalyst particles attached to amorphous carbon as opposed to being intergrown upon graphene sheets to be able to evaluate the added benefits/disadvantages of the combined 3D materials as compared with a CNF blank. The synthesis protocols of said CNF blank samples follow.

The production of the CNF blank sample began with the reduction of  $\text{Ni}(\text{NO}_3)_2 \cdot 6\text{H}_2\text{O}$  with urea to produce nickel catalyst particles. Similarly to the previous syntheses, the weight ratio of 7:1 (urea to nickel salt) was used for the reduction. The first step in the reduction of nickel salt to nickel nanoparticles was to weigh each component (90 mg of nickel salt and 630 mg of urea). The nickel salt and urea mixture was then crushed until homogeneous with a mortar and pestle. After the sample was weighed and mixed, the nickel was reduced via urea at high temperature in the clamshell tubular furnace identically as described *a priori*.

Following the high temperature reduction of nickel salt to nickel nanoparticles via urea, CNF were grown on the sample. The CNF growth procedure discussed in the preceding section was followed exactly for the CNF growth for the CNF blank samples and the stepwise production is shown in Figure 14.

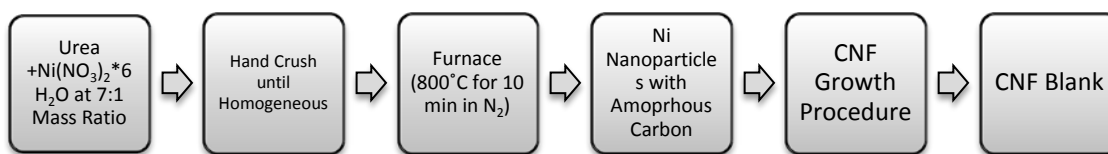


Figure 14. Stepwise production of CNF blank samples.

#### E. ELECTRODE SYNTHESIS

The final discussion in Chapter II is that of creating electrodes using the graphene-CNF structures described heretofore. The ultimate objective of this work is the novel synthesis of a graphene-CNF structure containing either nickel or nickel oxide for



use as active material for electrodes for use in energy storage devices, specifically supercapacitors. These electrodes were designed and tested to evaluate the efficacy to which this objective was realized.

The first step in the electrode construction was designing a process by which the graphene-CNF materials could be adhered to a current collector. The graphene-CNF architectures were nanopowder materials and as such a slurry containing the graphene-carbon nanofiber structures was designed to allow the application of the synthesized materials to a metallic current collector. This paste was prepared using graphene-CNF samples, acetylene black (JACAAB L.L.C, Carbon Black Acetylene Black, 100% weight), polyvinylidene fluoride (PVDF) (MTI Corporation, Ethene, 1, 1-difluoro-, homopolymer, 100% weight), and N-Methyl-2-pyrrolidone (NMP) (MTI Corporation,  $C_5H_9NO$ , 99.5% weight, <0.1% water, density p20g/ml 1.032-1.035). Acetylene black is used as a complementary material to increase available mass for use in electrode production and to combat the negative effect on conductivity experienced by adding PVDF. PVDF is a binding material employed to ensure the slurry will adhere to the current collector as well as the proper pasted consistency; however, PVDF lowers the overall conductivity of the solution. Finally, NMP chemically activates the PVDF binder and is the solvent in which the slurry solution is dispersed.

After selecting the materials used for slurry generation, the next obstacle to electrode construction was designing the proportionality of the slurry constituents. To this end, for each graphene-carbon nanofiber active material electrode created, the same weight percentage ratio of solid powder ingredients was used: 72 wt% graphene CNF architecture, 20 wt% acetylene black, and 8 wt% PVDF.

Once the wt% of the slurry components were determined, the next step in constructing the electrodes was to weigh out each of said elements based upon the intended proportion. The graphene-CNF material, acetylene black and PVDF were weighed and mixed together in a 20 mL beaker forming a homogenous solid powder. Following mixing, the solid powder materials were sonicated for five minutes to ensure the PVDF binder was adequately dispersed throughout the solid powder mixture. Next, NMP was added drop wise to the dry powder combination until the solution had a “flat

black paint” consistency. After the NMP addition, the solution was again sonicated for five minutes to guarantee both the PVDF and NMP had been evenly distributed amongst the slurry solution.

Following sonication, the slurry was evenly spread to a thickness of 250  $\mu\text{m}$  over nickel foil (Alfa Aesar, nickel foil, 0.0025 mm (0.001 in) thick, annealed, 99.5% (metals basis), 25 x 500 mm) using a micrometer film spreader (Figure 15). After the slurry was evenly spread, it was dried in a Cole Parmer Laboratory Oven (Model 05015-50, 115 volts, 800 watts) at 100°C for one hour (Figure 16(a)). Finally, the dried electrode material was allowed to cool to room temperature and was then cut into 15 mm diameter circles using an MTI Corporation Precision Disc Cutter (Model T-0.6, weight 38.5 kg, no. 01196, date 03/13/2012) (Figure 16(b), (c)). Electrodes were now created from graphene-CNF architectures containing either nickel or nickel oxide as their active materials and were now ready for characterization (Figure 17).



Figure 15. (a) Micrometer film spreader used to evenly spread electrode slurry (b) Slurry with graphene as active material spread to 250  $\mu\text{m}$ .

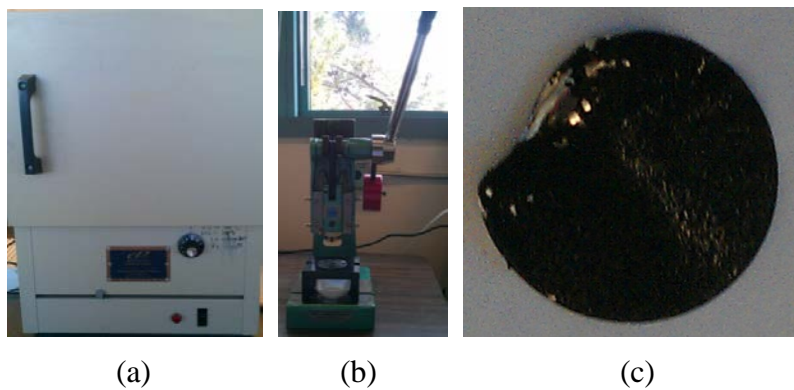


Figure 16. (a) Cole Parmer Laboratory Oven (b) MTI Corporation Precision Disc Cutter (c) Completed 15 mm diameter electrode.



Figure 17. Stepwise electrode synthesis.

THIS PAGE INTENTIONALLY LEFT BLANK

### **III. CHARACTERIZATION TECHNIQUES**

This chapter is a segue between the material synthesis and the results and discussion chapters. Upon completion of the 3D graphene-carbon nanofiber architecture containing nickel syntheses, oxidation of the same, generation of carbon nanofiber blank samples and electrodes of each of the above, various methods were used to characterize the composition, crystalline structure, microstructure, surface area, and specific capacitance of the materials. The techniques used to perform such characterization were thermogravimetric analysis (TGA), X-ray diffraction (XRD), scanning electron microscopy (SEM), Brunauer Emmett Teller (BET) surface area analysis, and electrical characterization, specifically specific capacitance measurements.

#### **A. THERMOGRAVIMETRIC ANALYSIS**

The first characterization technique described is thermogravimetric analysis (TGA), a method of thermal analysis in which changes in sample weight are measured as a function of increasing temperature (with constant heating rate) or as a function of time (with constant temperature) [40]. TGA can provide information about both physical phenomena, such as absorption, adsorption, and desorption and also chemical phenomena including decomposition and solid-gas reactions (e.g., oxidation or reduction) among others [40]. TGA was used in this work to analyze the simultaneous oxidation of nickel nanoparticles and burn off of carbonaceous materials (graphene and CNF).

The intent of the thermal analysis performed in this study was to determine the optimal temperature at which the nickel nanoparticle oxidation could be maximized but carbon burn off would be minimized. To that end, the thermal analyzer used for this analysis was the NETZSCH STA 449 F3 Jupiter analyzer connected with the NETZSCH QMS 403C Aeolos spectrum analyzer (Figure 18), which consists of a sensitive scale (0.001 mg) and heating elements inside a tubular furnace that can tightly control atmosphere.

Thermogravimetric analysis protocols are relatively straight forward with the first step being to weigh out the sample which is to be analyzed and placing it into the sample

crucible. The desired temperature and gas profile for the thermal experiment is then programmed into the STA 449 software suite and the automated thermal analysis commences. The thermal analyzer then measures mass changes throughout the conduct of the temperature profile and the mass spectra analyzer identifies volatile species evolved from the sample heating process.

More specifically, the thermal analysis cycle employed for this experiment began at room temperature and increased to a final temperature of 750°C at a constant heat rate of 5°C per minute. The analysis cycle was performed in an oxidant environment with a 4:1 ratio of Ar to O<sub>2</sub> (40:10 mL/min). The results and discussion of the TGA are included in the following chapter.

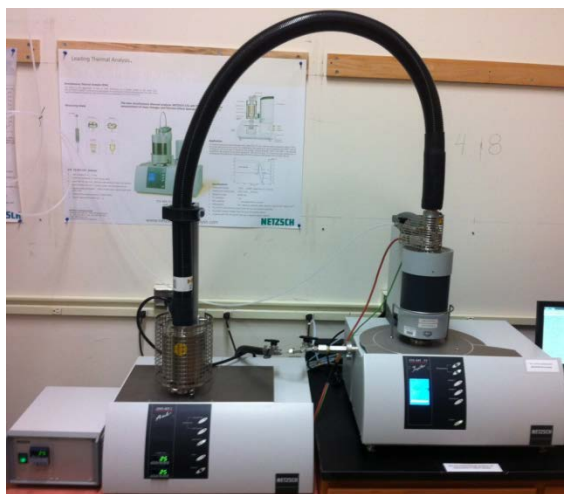


Figure 18. NETZSCH STA 449 F3 Jupiter thermal analyzer on the right and the NETZSCH QMS 403C Aeolos spectrum analyzer on the left.

## **B. X-RAY DIFFRACTION**

X-ray crystallography is a method used for determining the atomic and molecular structure of a crystal in which the atoms in the crystal cause a beam of X-rays to diffract into specific directions. By measuring the angles and intensities of these diffractions, the crystalline structure, composition based on crystalline components, as well as many other physical characteristics of the sample can be identified. The materials synthesized in this manuscript consisted of nanopowders that were crystalline in nature, and thus X-ray

diffraction could provide much insight into the crystalline structure of said nanopowders. XRD characterization was performed primarily to verify the transformation of graphite into graphite oxide and the decomposition of the same into graphene during the thermal exfoliation step. The X-ray diffractometer used was a Phillips Type PW1830/40 Analytical X-ray B.V. with a PW1830 generator (Figure 19). The X'Pert Data software package was programmed with the following parameters for each XRD run:

Table 3. Settings used for x-ray diffraction runs to determine composition of nanopowder materials.

Parameter	Value
Start Position [ $^{\circ}2\theta$ ]	5.000
End Position [ $^{\circ}2\theta$ ]	70.000
Step Size [ $^{\circ}2\theta$ ]	0.0100
Scan Step Time [s]	1.0000
Scan Type	Continuous
Offset [ $^{\circ}2\theta$ ]	0.0000
Anode Material	Cu
K-Alpha1 [ $\text{\AA}$ ]	1.54060
K-Alpha2 [ $\text{\AA}$ ]	1.54443
K-Beta [ $\text{\AA}$ ]	1.39225
K-A1/K-A2 Ratio	0.50000
Generator Settings	10 mA, 10 kV

X-ray diffraction characterization is nearly completely automated. After placing the sample on a zero-background sample holder, the specimen was locked inside the diffractometer. Next, the XRD voltage and current were established at 30 kV and 35 mA respectively. Following establishing the XRD parameters, the software suite executed the program detailed in Table 3.

The software suite collected the diffracted data and compared the results to the database of the International Centre for Diffraction Data identifying possible crystalline

structure matches and ranking them by likelihood percentage. The operator is then provided the opportunity to select only patterns that indicate a match based on the diffraction data and known composition.



Figure 19. Image of X-ray diffractometer. From [36].

### C. SCANNING ELECTRON MICROSCOPY

The description of the characterization methods now turns to scanning electron microscopy, which was performed to examine the microstructural details of the structures synthesized herein. A scanning electron microscope (SEM) is a microscope which produces images based on the interaction of a focused beam of electrons and the electrons contained within the specimen. The focused beam of electrons supplied by the microscope elicits specific interactions with the electrons within the sample and those produce signals that contain information regarding the sample's surface topography and composition. The electron beam, typically scanned in a raster scan pattern, then combines beam position with collected data to produce an image which can be stored digitally.

SEM images were collected using a Zeiss Neon 40 Crossbeam scanning electron microscope with a Schottky type field emission system (Figure 20). After, the specimen was loaded onto a stage and placed inside a vacuum chamber, the microscope voltage and current were established at 20 kV and  $0.33 \times 10^{-6}$  mA respectively. Images were then collected at 2K, 4K, 8K, 16K, 32K, and at higher magnification as the sample warranted.



At lower magnifications general characteristics of the samples surface were obtained, while at higher magnifications it was possible to closely examine the microstructure of the 3D graphene-carbon nanofiber architecture containing dispersed nickel to evaluate the distribution of phases and efficacy of the synthesis protocols.

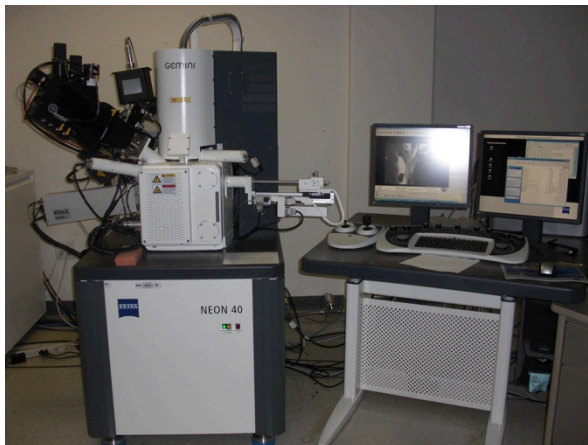


Figure 20. An image of the Zeiss SEM. From [36].

#### **D. BRUNAUER EMMETT TELLER SURFACE AREA ANALYSIS**

The Brunauer Emmett Teller (BET) method was employed for the evaluation of the surface area of the nanopowder materials generated in this manuscript [41]. The surface area analysis was performed using a NOVA 4200e Surface Area and Pore Size Analyzer by Quantachrome Instruments (Figure 21). Surface area analysis was instrumental in evaluating the potential for strong electrical performance for each of the synthesized architectures based on the correlation of such with surface area measurements. The greater the specific surface area, the more area available to generate charges within the electric double layer, and as such, specific surface area was the determining factor as to which graphene-CNF structures were carried forward for electrical characterization.

BET theory aims to explain the physical adsorption of gas molecules on a solid surface and serves as the basis for an important analysis technique for the measurement of the specific surface area of a material. The BET equation is given by:

$$\frac{1}{W((P_o / P)-1)} = \frac{1}{W_m C} + \frac{C-1}{W_m C} \left( \frac{P}{P_o} \right) \quad 2$$

where  $W$  is the weight of the gas adsorbed at the relative pressure of  $P/P_o$ , and  $W_m$  is the weight of the adsorbate constituting a monolayer of surface coverage. The term  $C$ , the BET  $C$  constant, is related to the energy of adsorption in the first adsorbed layer and consequently its value is an indication of the magnitude of the adsorbent/adsorbate interactions [41].

BET analysis is largely automated, the first step involved loading the sample to be measured into the BET cabinet. The surface area analysis then began with a degassing procedure in which the sample was degassed at room temperature for 10 minutes, 100°C for 30 minutes, and 200°C for 150 minutes. Upon completion of the degassing phase, the Quantachrome NovaWin software suite commanded the sample to be submerged in liquid nitrogen and followed the preprogrammed carbonaceous material measuring protocol to analyze surface area.

The automated measurements were allowed to run overnight. Following completion of the measurements, the sample was removed from the NOVA instrumentation and an accurate sample weight was determined. The final weight was input into the software analysis suite and the specific surface area was calculated. This specific surface area values were compared amongst the graphene-CNF structures to determine which had the superior surface area.



Figure 21. NOVA 4200E surface area and pore size analyzer.

## E. ELECTRICAL CHARACTERIZATION METHODS

The final characterization method employed was that of electrical properties, namely specific capacitance measurements. The primary objective of this thesis was the novel synthesis of graphene-CNF materials and electrodes of the same for use in energy storage devices, specifically supercapacitors. Furthermore, specific capacitance was the measurement by which the achievement of this goal and sample comparison was evaluated.

To that end, an electrical test cell (Figure 22) was designed and constructed in order to measure capacitance by means of a BK Precision 4011A 5MHz function generator, a Global Specialties design and prototyping proto-board PB-503, and a Tektronix TDS2024B four channel digital storage oscilloscope (Figure 23).

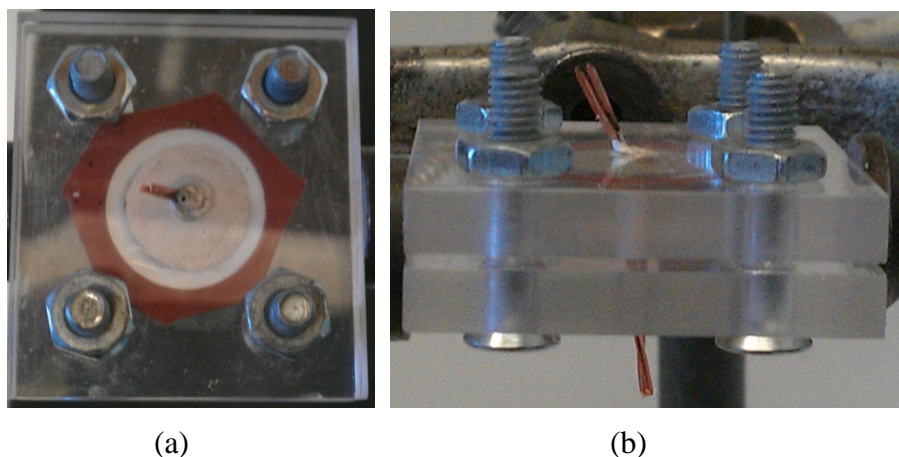


Figure 22. Top view (46mm x 41.3 mm) (a) and side view (b) of constructed electrical test cell

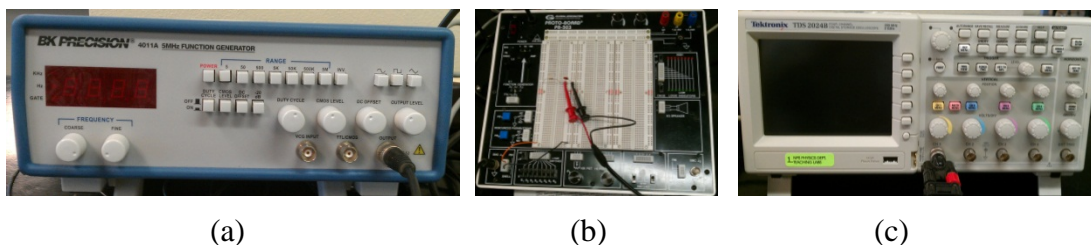


Figure 23. Electrical characterization equipment (a) BK Precision 4011A 5MHz function generator (b) Global Specialties design and prototyping proto-board PB-503 (c) Tektronix TDS2024B four channel digital storage oscilloscope

The first step in the electrical characterization was the design and construction of the electrical test cell, which began with the acrylic base material (Figure 24(a)). The acrylic was cut into 46 mm x 41.3 mm rectangles and five holes were drilled into the rectangular base with the central hole cut to a 3 mm diameter. The four holes in the corners are 4.5 mm in diameter.

After the acrylic base was cut to size, a 15 mm nickel foil current collector (of same material as detailed during the electrode synthesis, Chapter II section E) was attached to one side of the acrylic base directly over the central hole using colloidal silver (Figure 24(b)). The final step in the acrylic base construction was to fill the central hole

with colloidal silver and insert copper wire into the central hole, directly opposite and in contact with the nickel foil. The copper wire was used as electrical test lead during the conduct of capacitance measurements (Figure 24(c)).

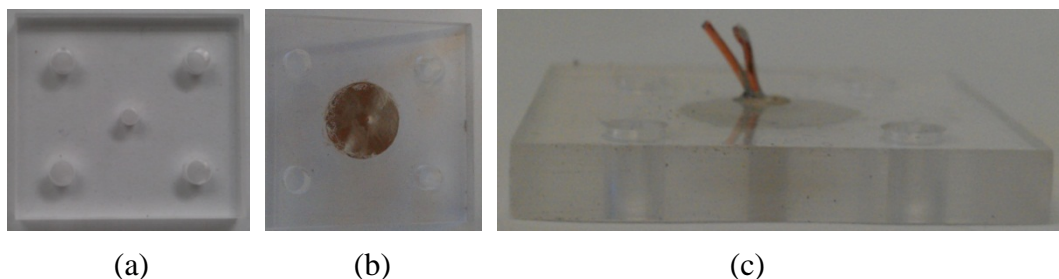


Figure 24. Electrical test cell in construction: (a) acrylic base, (b) nickel foil current collector on inside surface of test cell, and (c) copper wire protruding from exterior surface of test cell.

Once the acrylic base was constructed, complete electrical test cell assembly began by selecting one acrylic base as the bottom of the test cell. The copper wire face would be oriented toward the bottom of the test cell. The next component in test cell assembly was a rubber O-ring of 20 mm diameter which was placed down surrounding the 15 mm diameter nickel foil previously attached to the acrylic base. A 15 mm diameter electrode would then be carefully placed directly on top of the nickel foil current collector with the active material facing upward. Following the electrode insertion, a Celgard 3501 2  $\mu\text{m}$  microporous monolayer membrane (surfactant coated) cut to a 20 mm diameter was placed over the electrode. 0.2 ml of 1M potassium hydroxide (KOH) was then placed on the upper side of the membrane. The second electrode, of the same active material as the first, was then placed, active material down, on top of the membrane. A second acrylic base piece completed the test capacitor, with the copper wire surface facing upward. Finally, the entire assembly was secured with nuts tightened to 5 in-lbs force using CDI torque products dial torque wrench. A schematic of electrical test cell assembly is shown in Figure 25.

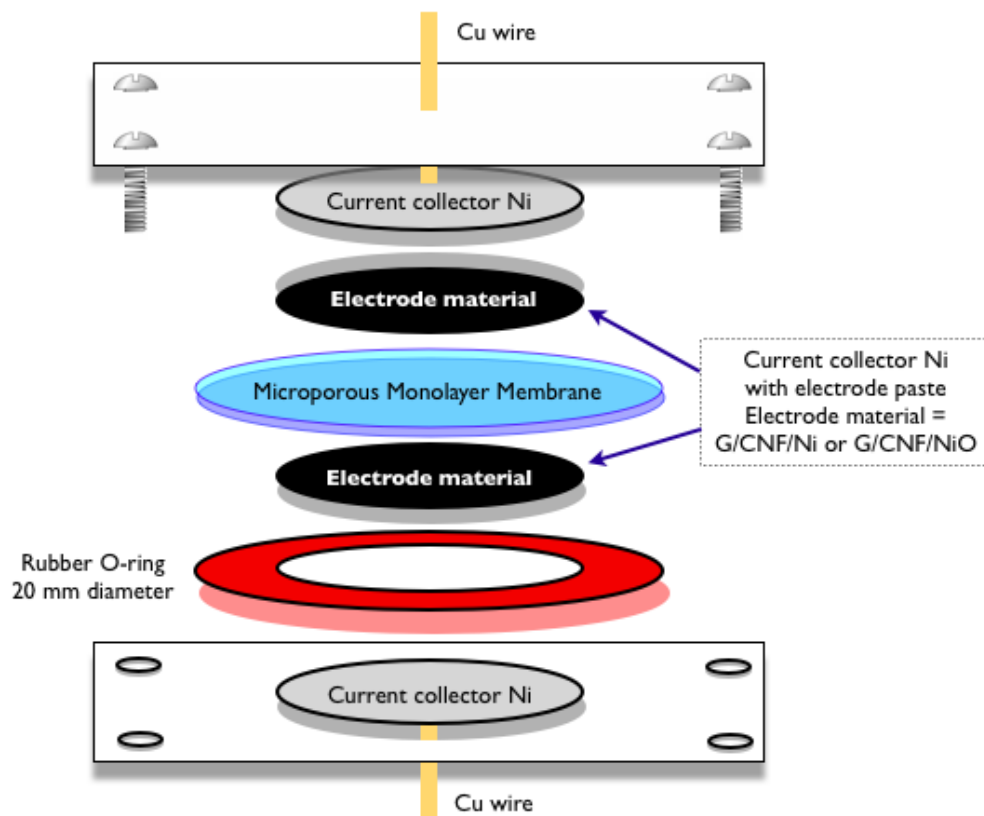


Figure 25. Electrical test cell assembly schematic.

After assembling the electrical test cell, electrical characterization was performed by analyzing a circuit with a resistor and the test cell assembly (capacitor) in series (RC circuit) (Figure 26) which was wired into the proto-board. The resistor in the RC circuit was a known  $100\ \Omega$  resistor and the capacitor was the test capacitor constructed above. A square wave of 5 Hz was then generated by the function generator and was the input voltage for the test circuit. The wave form across the electrical test cell was captured using the oscilloscope and an exponential curve fit was applied to the data of one charging cycle of the test capacitor.

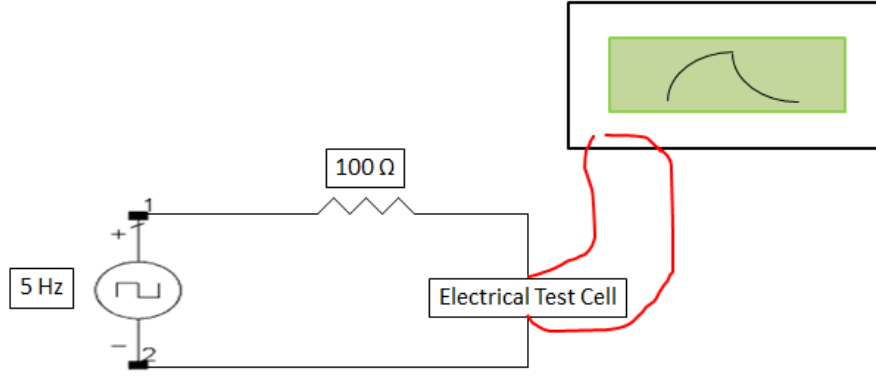


Figure 26. Capacitance measurement circuit schematic.

Upon capturing the output waveform, two different methods were employed to calculate the capacitance of the test cell. The first method was to apply an exponential curve fit in the form of equation 3 to the raw output data. The curve fit provided the value in the exponential term ( $-1/RC$ ) and capacitance could be calculated. The second means by which capacitance was determined was by plotting a linear curve fit to the raw data in the form of equation 4. The slope of the best fit line then correlated to ( $-1/RC$ ) and capacitance of the test cell was easily calculated. Both means of calculating test cell capacitance was used to check for consistency between the measurements.

$$V(t) = V_0 \left( 1 - e^{\frac{-t}{RC}} \right) \quad 3$$

$$\ln \left( \frac{V_0 - V(t)}{V_0} \right) = -\frac{1}{RC} t \quad 4$$

Finally, specific capacitance was determined. Specific capacitance was the primary metric used to evaluate the performance of graphene-CNF materials for use in energy storage devices. In order to determine the graphene-CNF architecture that performed the best electrically, the empirically determined capacitance values were normalized by the weight of the graphene-carbon nanofiber material utilized in each test capacitor. This allowed for direct electrical comparison with the results being detailed in Chapter IV.

THIS PAGE INTENTIONALLY LEFT BLANK



## IV. RESULTS AND DISCUSSION

After describing both the syntheses and the characterization techniques used in this manuscript, this chapter reveals the results of said characterizations and discusses the possible mechanisms and theories used to elaborate on the results. Moreover, the novelty of the methods employed to generate materials, the structural characteristics of the same, and capacitance values comparison with respect to the previously published data is discussed.

### A. GRAPHITE OXIDE

The first material creation protocol described was that of graphite oxide, and thus these are the first results discussed. As detailed in Chapter II, GO was produced using a further alteration to the modified Hummer's method [35] and used primarily as the precursor to graphene. The GO synthesized in this study was evaluated using XRD, where the d-spacing was calculated using the  $2\theta$  values according to Bragg's Law:

$$n\lambda = 2d \sin \theta \quad 5$$

Diffraction data was evaluated in order to determine the peak shifts that occurred during the transformations from commercial graphite nanopowder to GO (Figure 27). XRD analysis of these peak shifts was employed to demonstrate the inclusion of the oxide groups amongst the graphite nanopowder as opposed to alternative methods to confirm the presence of oxygen described in literature [42].

The principal indication the commercial graphite nanopowder had successfully transitioned to graphite oxide was the shift of the primary XRD peak [43]. Commercial graphite nanopowder used for the synthesis of GO in this work shows the (002) reflection at  $\sim 25^\circ$ , which corresponds to a d-spacing of 3.366 Å. The shift of this peak from  $\sim 25^\circ$  to  $\sim 10^\circ$  in GO indicates the intended attachment of oxide groups to the graphite nanoparticles.

XRD analysis of the graphite oxide synthesized from the commercial graphite nanopowder yielded peaks near 10 and 45 degrees, corresponding to d-spacings of 9.791

Å and 2.129 Å. This demonstrates the desired shift of the primary peak, miller index (002), from  $\sim 25^\circ$  (commercial graphite nanopowder) to the near  $10^\circ$  (graphite oxide) indicating successful attachment of the oxide groups to the graphite nanoparticles. The attachment of the oxide groups is essential in the subsequent generation of graphene, which is formed when the graphite oxide oxygen groups located in between the sheets are lost during thermal exfoliation.

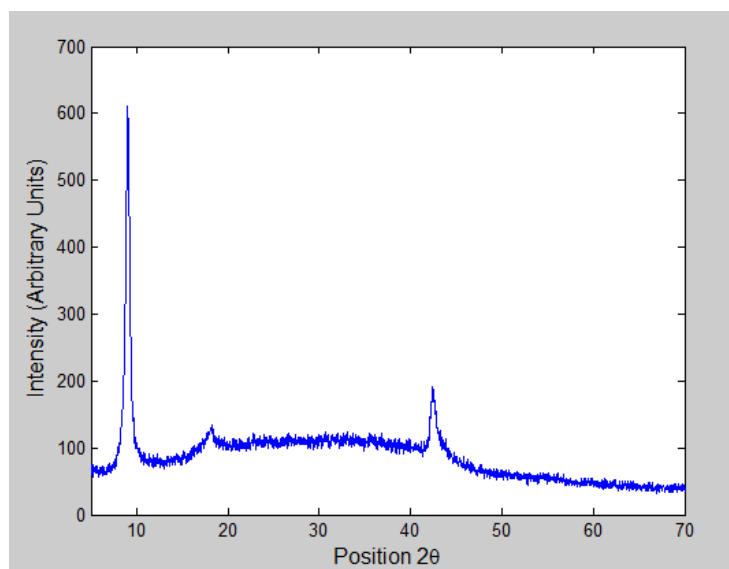


Figure 27. XRD peaks of GO. Note the primary peak (Miller index (002), has shifted from  $\sim 25^\circ$  to  $\sim 10^\circ$ .

## B. GRAPHENE

Following the generation of graphite oxide, the next step in the creation of a graphene-CNF structure was the exfoliation of GO into graphene. Many procedures for the production of graphene have been reported in literature: micromechanical cleavage [11, 44, 45], chemical reduction techniques which utilize hydrazine or urea to remove oxygen from GO [46, 47], procedures that generate free-standing graphene sheets such as chemical vapor deposition [48, 49], thermal exfoliation of graphite oxide such as performed in this manuscript [50, 51], thermal desorption of Si from SiC substrates [52], and the solvothermal process to achieve a reduction in GO and introduction of primary amine to graphene [53] are some examples.

This study employed the thermal exfoliation of graphite oxide technique to produce graphene due to ease of synthesis and relative high yields. Thermal exfoliation of GO into graphene essentially consisted of two phases: oxygen species addition between graphite layers to encourage separation between sheets (during the production of GO and as demonstrated above) and exfoliation at high temperature which eliminated the oxygen groups leaving behind separated sheets of graphene in a honeycomb type of network.

Graphene, which was the base material from which carbon nanofibers were grown, was characterized via multiple mechanisms including XRD, SEM and BET. XRD analysis was used to confirm the removal of the oxygen groups from among the graphene layers during the high temperature exfoliation process and confirm the crystalline nature of the graphene. SEM was employed to examine the microstructure of the graphene and BET was performed to measure specific surface area for comparison with the completed 3D G/CNF/Ni and G/CNF/NiO architectures, as well as contrasting such values with similar structures found in literature.

X-ray diffraction results will be the first to be described with respect to the graphene characterization (Figure 28). Of note demonstrated by the XRD peaks, is the primary peak, miller index (002) and d-spacing of 3.389 Å, has shifted from the  $\sim 10^\circ$  indicated in the XRD analysis of the graphite oxide (Figure 27) back to  $\sim 25^\circ$  indicating the desired elimination of the oxide groups. While the oxide groups were necessary to separate the graphene layers in the GO, the goal of the thermal exfoliation was the removal of the oxygen groups to leave behind the honeycomb structure of graphene sheets.

Further observation of the XRD analysis of the graphene sample reveals it is suggestive of a specimen having less crystalline order than does GO, as demonstrated by both wide peaks and low intensity peaks in the XRD pattern; however, those characteristics are also observed with disordered graphene or when small particle size is attained. Visual inspection of graphene after production confirms evident exfoliation based upon volume occupied after exfoliation as demonstrated by Figure 29, which shows 15 mg of GO and graphene side by side.

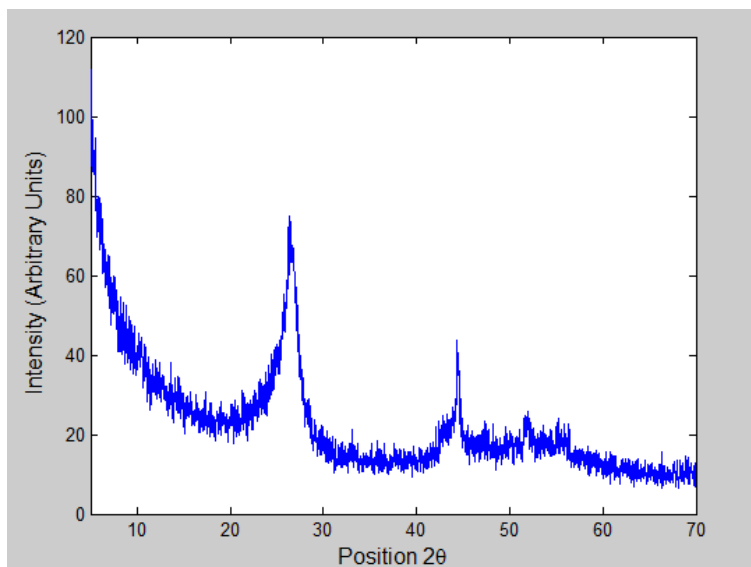


Figure 28. XRD analysis of graphene.



Figure 29. Visual comparison of 15 mg of GO versus graphene.

Following XRD analysis of graphene, scanning electron microscopy was performed with a typical image of the microstructure shown in Figure 30.

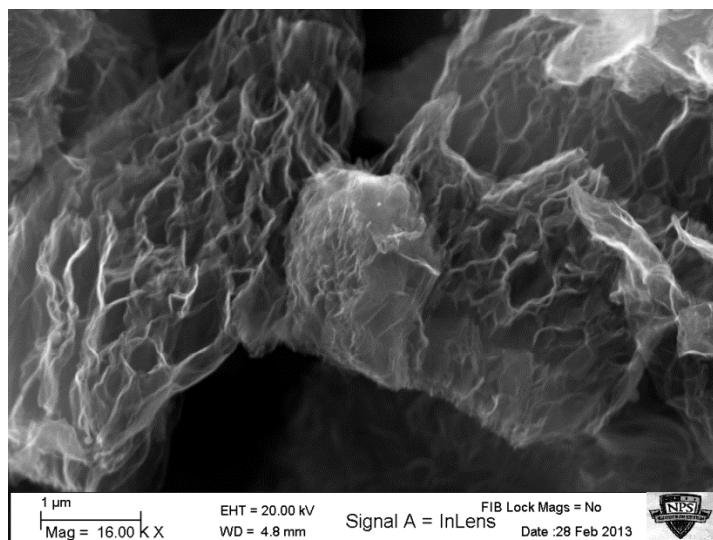


Figure 30. SEM image of graphene.

Inspection of the graphene micrograph indicates the graphite oxide exfoliated in a transverse direction in a honeycomb pattern as opposed to exfoliating in singular sheets. Moreover, each fan-shaped structure appears to be completely randomly oriented with respect to one another. Additionally, the fan-like architecture provides a three-dimensional network when compared with individual sheets but does not adversely affect the surface area. This honeycomb three-dimensional network is an ideal birthplace for creating a 3D graphene-CNF matrix. By examining the graphene micrograph it is clear that a 3D architecture can be created if the carbon nanofibers can be disseminated and grown within the graphene sheets.

The final characterization method used to analyze graphene was surface area analysis, which was performed in order to compare the specific surface area values with the graphene-carbon nanofiber architectures as well as published metrics in current literature. The specific surface area of graphene created for this work was measured at  $620 \text{ m}^2/\text{g}$  which compares favorably to numbers reported in literature (202, 612, and  $705 \text{ m}^2/\text{g}$ , respectively) [27, 54, 55]. Furthermore, this sets the standard for surface area against which the G/CNF/Ni and G/CNF/NiO structures will be measured.

### C. CARBON NANOFIBER BLANK SAMPLES. PRODUCTS CNF/NL.

As detailed in the Chapter II, carbon nanofibers were grown from nickel catalyst sites amongst amorphous carbon for comparison with the graphene-CNF architectures in both surface area analysis and electrical characterization. Moreover, as a point of further reference, the carbon nanofiber blank sample was also oxidized to compare the effects on surface area and capacitance to the graphene carbon-nanofiber structure. The CNF blank samples were analyzed via scanning electron microscopy and BET surface area analysis. Figure 31 shows the microstructure before the fiber growth synthesis.

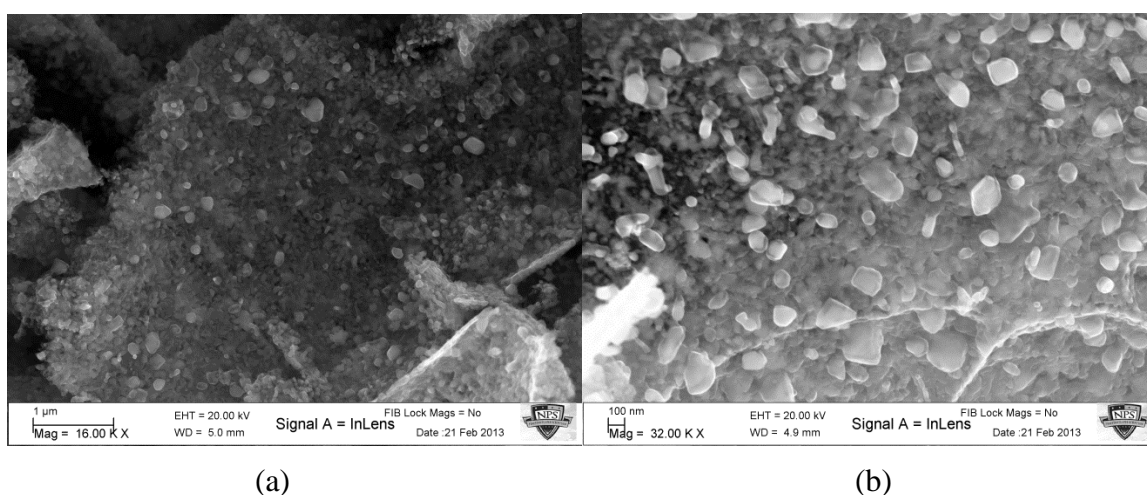


Figure 31. SEM images of blank sample (nickel only) at (a) 16k and (b) 32k magnification before fiber growth.

Evident in the nickel blank pre-fiber growth micrographs are varying sizes of nickel nanoparticles. The effect of urea in the RES is to reduce the sample to its metallic state. A byproduct of the same is the generation of amorphous carbon, which is evident in the SEM observation of the nickel only (no CNF) images in Figure 31. Moreover, the nickel salt reduction resulted in nickel particles ranging in diameter from 10s of nm to 100s of nm. These values are highly preferred when compared to the commercial nickel nanopowder, which usually range from a few nm to a submicron range, having only the average in the nm size. The subsequent carbon nanofiber growth procedure therefore yielded fibers of a similar distribution of sizes (Figure 32).

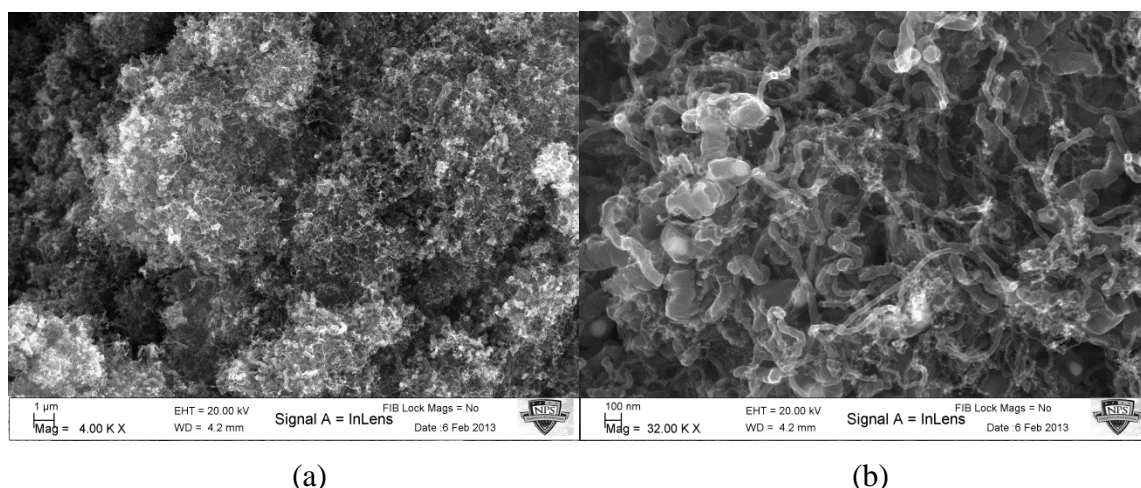


Figure 32. SEM images of CNF blank sample (CNF/Ni) at (a) 4k and (b) 32k magnification after the fiber growth process.

The second means by which the CNF blank samples were characterized was BET surface area analysis, which yielded values of 79.3 and 90.9 m<sup>2</sup>/g for samples which were not oxidized and oxidized respectively. The carbon nanofiber blank sample was grown from nickel nanoparticles produced by RES, which usually yields some amount of amorphous carbon, and was oxidized as well for surface area and specific capacitance comparison with the graphene-CNF structures. The surface area determination for the CNF blank samples with Ni (CNF/Ni) and NiO (CNF/NiO) demonstrates an increase in surface area due to the oxidation process. Though there is no graphene in the blank sample, amorphous carbon is still present at the base of the fibers for CNF/Ni samples, and though the oxidation temperature was low enough to prevent significant carbon burn off, the CNF/NiO sample presents higher surface area due to pitting that occurred to the amorphous carbon surface.

#### **D. 3D GRAPHENE-CARBON NANOFIBER ARCHITECTURES CONTAINING NICKEL**

After examining both GO and graphene in detail, much characterization effort was spent on determining the material properties of graphene-CNF structures created. The novelty of this work is the unique method by which graphene and carbon nanofibers were intermixed to form a three-dimensional structure. Current research methods employ

an aqueous dispersion technique to intercalate the graphene sheets with carbon nanofibers [27, 28], essentially a physical mixture of components. This manuscript depicts a method in which the carbon nanofibers are grown directly upon the graphene layers *in situ*. Moreover, the fabrication method used, based on the initial mixture of the graphene precursor with a nickel salt and urea represents a series of processes all happening simultaneously: graphene formation by an exfoliation of the carbon sheets while oxygen species leave the structure generating a chemically reduced graphene product as well as the reduction of the nickel salt to produce finely divided metallic nickel nanoparticles. The latter is only possible by the reaction with urea, which produces ammonia and CO that react with oxygen groups and nitrate ions to produce fully reduced nickel. The characterization employed in this section was performed not only to verify distribution of phases but also to understand their growth mechanisms.

As documented in the Chapter II, two separate methods were initially performed to create a graphene material interlaced with nickel nanoparticles: an aqueous preparation and a dry preparation method. Furthermore, within each preparation method, two alternatives were employed to achieve nickel nanoparticle distribution: direct application of nickel salt to GO precursor and addition of the same to previously exfoliated graphene. Please refer to Table 2 in Chapter II.

Initially, G/CNF/Ni materials were generated from both preparation methods (dry and aqueous) and using both precursors (GO and graphene) with 3 wt% nickel loading. Subsequent BET and SEM analysis indicated the aqueous prepared samples from graphene precursors yielded the most potential for electrical properties desired in this work based upon superior surface area performance. Therefore, further experimentation continued only with aqueous samples from graphene precursors, and only the graphene-CNF structures that presented high surface areas were characterized electrically.

### **1. Aqueous Preparation**

Nickel nanoparticles were needed as catalyst to generate the carbon nanofibers within the graphene layers and were synthesized from a nickel salt ( $\text{Ni}(\text{NO}_3)_2 \cdot 6\text{H}_2\text{O}$ ), which could easily be dissolved in water. The aqueous preparation represents an attempt



to uniformly distribute the catalyst particles within the graphene sheets and subsequently, upon a reduction step, grow carbon nanofibers. From these protocols samples of G/CNF/Ni-1% and G/CNF/Ni-3% were generated.

**a. Graphite Oxide Precursor. Products: Graphene/Ni and Graphene/CNF/Ni**

Scanning electron microscopy of the aqueously prepared G/Ni-3% from a GO precursor is shown in Figure 33.

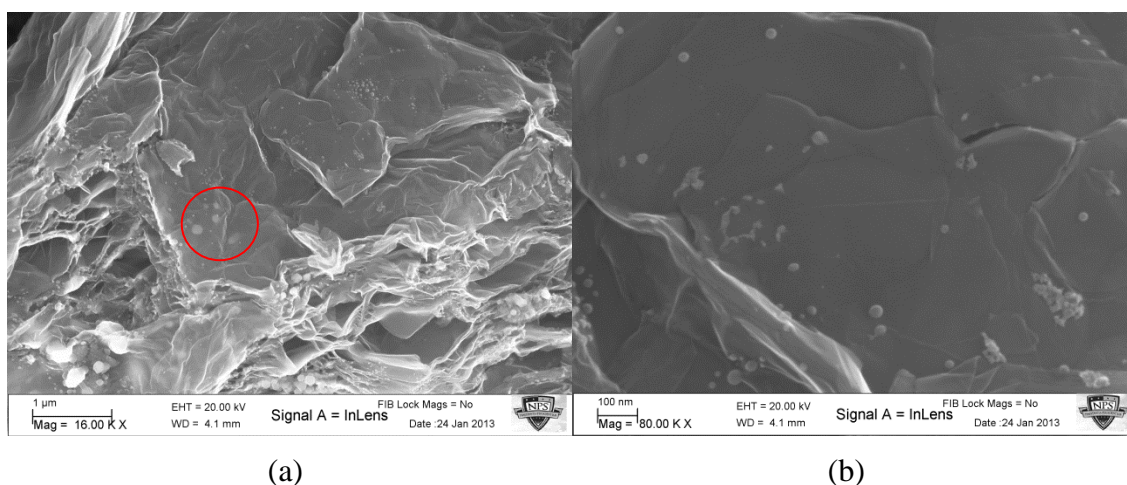


Figure 33. SEM images of an aqueously prepared sample from GO precursor before CNF growth, G/Ni at (a) low magnification and at (b) high magnification. Note the nickel particles underneath the top graphene layer in (a).

Examination of the micrographs in Figure 33 illustrates the successful particle intercalation within the graphene matrix. The particles tend to attach to graphene surface in places where either kinks, voids or defects are evident as well as in the edges, as expected from a heterogeneous nucleation mechanism where the nickel formed from the liquid and deposited in an already existent solid. Furthermore, Figure 33(a) indicates the desired nanoparticle distribution in between graphene sheets as evidenced by the catalysts seen through the top graphene layer. The uniform dispersion of nickel particles within graphene layers indicates the potential for a unified 3D structure upon the completion of CNF growth. Each of the nickel particle locations indicates future growth

sites for carbon nanofibers and the ability to physically exfoliate graphene layers and increase electrical and ionic connectivity between sheets, creating the desired three-dimensional architecture.

Additionally of note in the above micrographs is the size of the nickel deposits on the graphene. Figure 33(b) demonstrates a diverse level of particle sizes and agglomeration, ranging from 10 nm in diameter to much larger nickel agglomerations which are often greater than 100 nm. This range in nanoparticle size distribution is acceptable and is an improvement on that of commercial nanopowders, which have much smaller and larger particles and only an average particle size in the nanometer scale. The reason for the size distribution is during the synthesis the nickel salt gets dissolved and during nucleation the nickel particles form first. Generally, a small nuclei forms initially, but as time passes they become larger (growth dominates over nucleation of new particles) and produce larger particles giving origin to a different size of fiber distribution.

Furthermore, a consequence of a wide range of nickel defect sites in the graphene matrix is a large variety in CNF size after the growth process. Figure 34 illustrates the typical G/CNF/Ni-3% architecture microstructure of the aqueously prepared sample from a GO precursor.

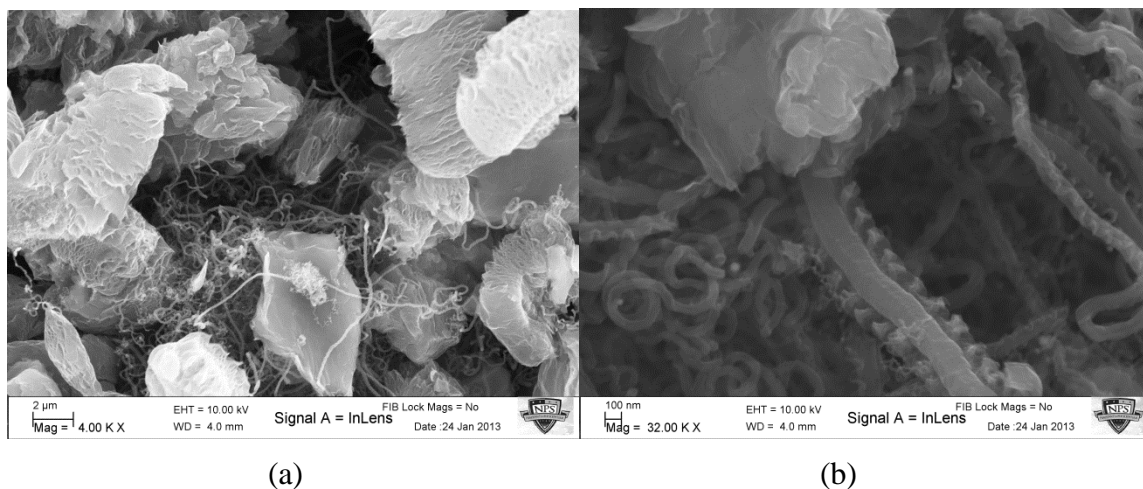


Figure 34. SEM images of an aqueously prepared sample with GO precursor after CNF growth, G/CNF/Ni at (a) 4k and (b) 32k magnification.

Figure 34(a) shows the dispersion of the CNF throughout the graphene base material as well as characterizing the length of the carbon nanofibers. The fibers were able to grow well into the 100s of  $\mu\text{m}$  length range with a 45 minute growth phase. Additionally, the carbon nanofiber network is widely distributed amongst the graphene matrix. This is due to the uniform distribution of nickel nanoparticles during the aqueous preparation method. Figure 34(b) illustrates the wide variation of fiber dimension as a result of the large diversity in nickel defect size discussed previously. As described during the discussion of the nickel nanoparticle size disparity, there are predominantly two classes of nanofiber dimension, the larger size on the order of 100 nm across and the smaller on the order of 10 nm.

The large carbon nanofibers combined with the variety of fiber size indicates the potential of lowering the surface area of the three-dimensional structure; however, as detailed *a priori*, the measured specific surface area was greater for the aqueously prepared samples when compared with the dry samples. This is likely due to perhaps the most intriguing microstructural characteristic discovered: the flap-like structure growing alongside the larger carbon nanofibers. This feature provides additional surface area along which charges may be stored (similarly to fins on a heat exchanger provide higher surface area for heat dissipation), as evidenced by the superior BET results of the aqueous preparation method as compared to that of the dry preparation method.

Upon completion of the SEM characterization, the last analysis employed for the aqueously prepared samples from a GO precursor was BET surface area analysis, which calculated the surface area at  $206 \text{ m}^2/\text{g}$ . This value of surface area is a 67% reduction in surface area from that of pure graphene but is significantly greater than the corresponding dry method from a GO precursor that had a surface area of  $79.6 \text{ m}^2/\text{g}$ . The large advantage in surface area for the aqueously prepared sample is attributed directly to the flap-like feature along the large carbon nanofibers whereas the drastic lowering of surface area from pure graphene is a consequence of nickel nanoparticles in the graphene-CNF matrix.

***b. Graphene Precursor. Products: Graphene/Ni and G/CNF/Ni***

While each of the aqueously prepared architectures had higher surface area values than did their dry method counterparts, the aqueously prepared graphene-CNF structures from graphene precursors demonstrated significantly better BET results than did those from GO precursors and, as a result, the nickel loading adjustments and the nickel oxidations of the graphene-carbon nanofiber structures as well as the electrical characterization were performed on graphene precursor samples only.

Characterization of the aqueously prepared specimens from graphene precursors begins with scanning electron microscopy. The microstructure for the graphene matrix with different nickel particle catalysts loading (both 1 wt% and 3 wt%) generated via the aqueous preparation method with graphene precursor is detailed in Figures 35 and 36.

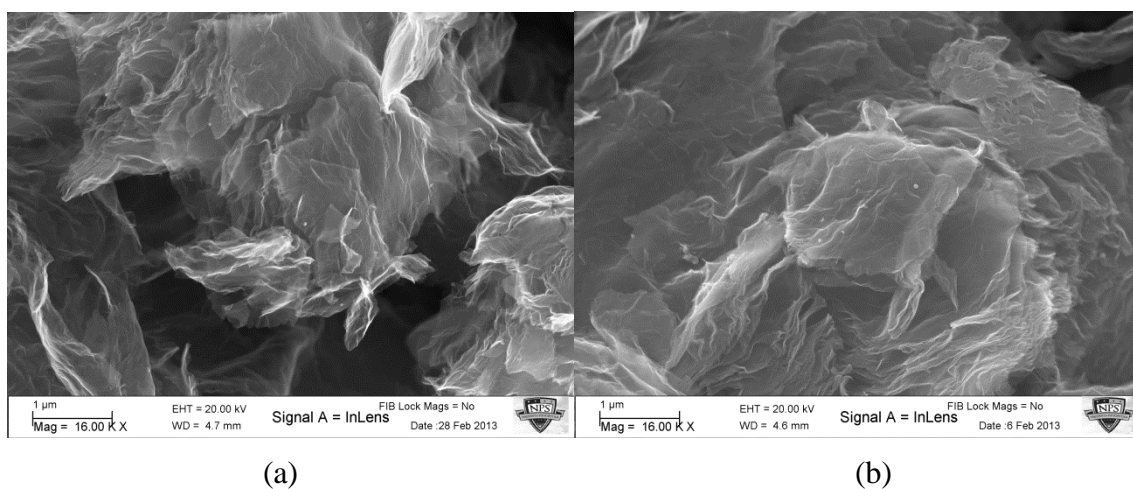


Figure 35. SEM images of aqueously prepared graphene with nickel nanoparticles from a graphene precursor (G/Ni) at low magnification with (a) 1 wt% nickel loading and (b) 3 wt% nickel loading.

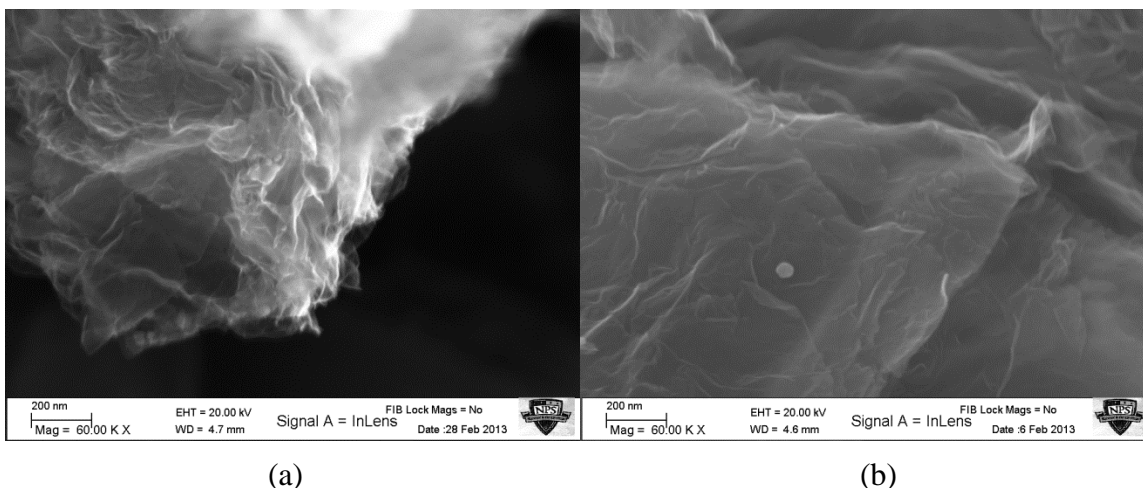


Figure 36. SEM images of aqueously prepared graphene with nickel nanoparticles from a graphene precursor (G/Ni) at high magnification with (a) 1 wt% nickel loading and (b) 3 wt% nickel loading.

Examination of the microstructures in Figures 35 and 36 for the aqueously prepared graphene sheets interlace with nickel nanoparticles yields several conclusions. First, by essentially exfoliating the graphene two times throughout the synthesis process (disseminating the nickel nanoparticles on previously exfoliated graphene before the nickel salt reduction process), the 3D honeycomb lattice displays better exfoliation for the samples with graphene as a precursor as compared with those with GO. Second, the wide variety in nickel defect site dimension, as described in the preceding GO precursor section, is still evident. This is further indication the wide range in nickel nanoparticle dimension is due to the synthesis process as opposed to material properties.

The final conclusion to be elaborated upon when examining the microstructure is that of nickel nanoparticle dispersion. When comparing the nickel particle dispersion between those of GO precursor and those of graphene precursor, there is a more uniform distribution of catalyst sites for samples with graphene as a precursor as compared to those with GO as a precursor. The more homogenous distribution of catalyst sites should indicate a more uniform distribution of carbon nanofibers and subsequently higher surface areas. This is verified by aqueously prepared samples from graphene precursors having superior surface area performance when compared to those of GO precursors. The increased nickel catalyst distribution in the aqueously prepared

sample from graphene precursor is due to the more complete graphene exfoliation. The layers in the three-dimensional honeycomb structures are further separated and therefore it is easier for the nickel particles to fully intermix within the graphene sheets. Additionally of note, there is no discernible change in nickel nanoparticle allocation when comparing the distribution between 1 wt% and 3 wt% nickel loading. This indicates that the fiber density and therefore the surface area should be similar between the two separate nickel loading scenarios, and is confirmed by the surface area values being nearly identical between both 1 wt% and 3 wt% nickel loading. This is further illustrated in Figure 37 where it is difficult to detail difference in the dissemination of the CNF between the separate nickel loading cases; however, the dispersion of CNF is more uniform for the samples with graphene precursor compared with GO precursor (Figure 34).

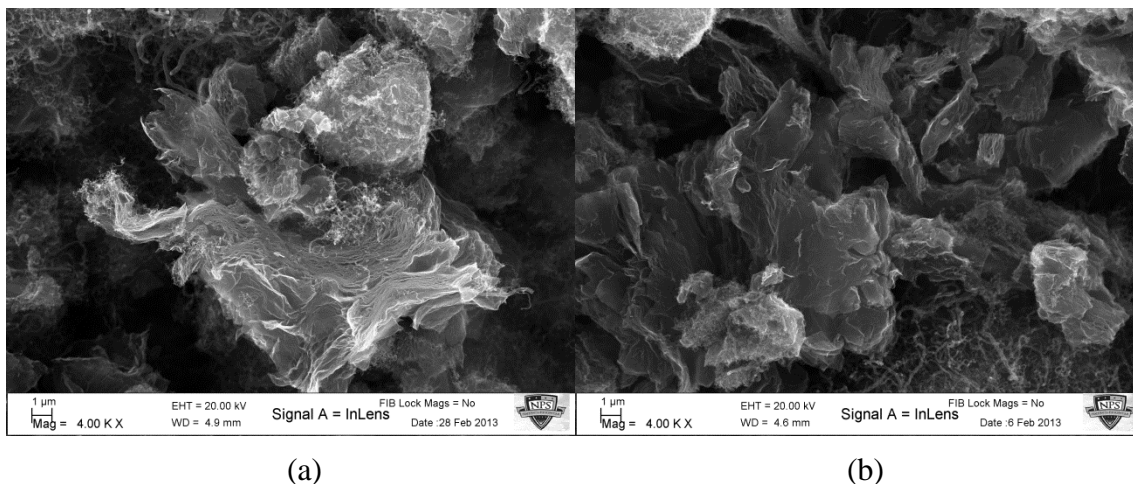


Figure 37. SEM images of aqueously prepared graphene-CNF architecture containing nickel (G/CNF/Ni) from a graphene precursor at 4k magnification with (a) 1 wt% nickel loading and (b) 3 wt% nickel loading.

Figure 38 shows higher magnification image of the carbon nanofibers on the aqueous sample from a graphene precursor. The fiber size disparity is similar to that of the GO precursor samples (i.e., there are largely two classes of fibers, a larger at 100 nm diameter and a smaller at 10 nm) as expected by the existence of the same variety of nickel nanoparticle dimension. Additionally, the same flap-like features can be seen on

the larger group of nanofibers and, as discussed previously, despite the nonhomogeneous fiber size distribution, the aqueously prepared samples have superior surface area numbers when compared to the dry prepared samples due to the flap-like features. Last, in Figure 38(b) a nickel particle can be seen at the end of one of the 100 nm diameter fibers. This proves the initial hypothesis that the carbon nanofiber growth process did indeed begin at the nickel catalyst sites within the graphene matrix. The CNF then extruded up from the graphene base extending the nickel particle away from the basal material.

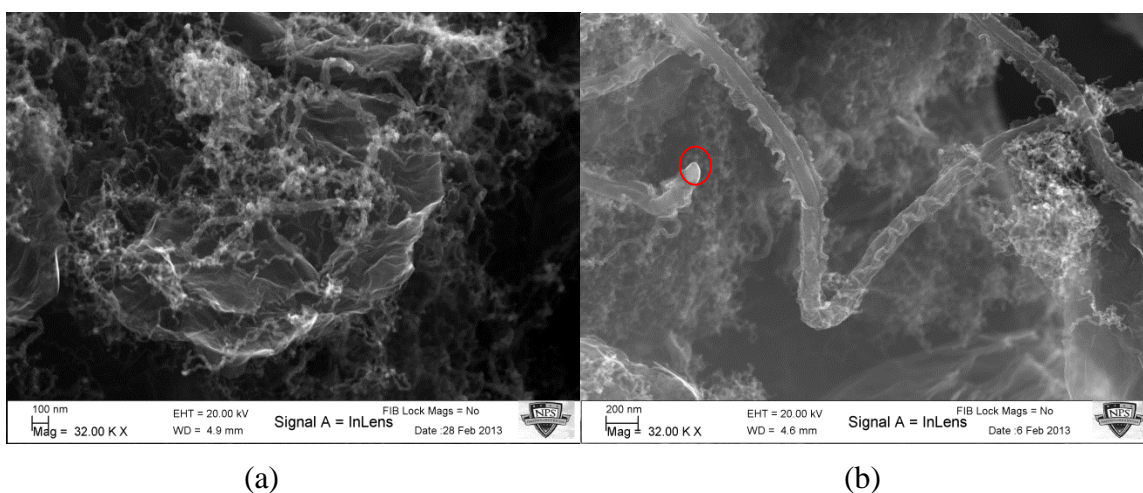


Figure 38. SEM images of aqueously prepared graphene-CNF architecture (G/CNF/Ni) containing nickel from a graphene precursor at 32k magnification with (a) 1 wt% nickel loading and (b) 3 wt% nickel loading. Note the nickel nanoparticle in (b).

The final characterization technique employed for the aqueously prepared samples from graphene precursor was surface area analysis, which yielded a specific surface area of 284 m<sup>2</sup>/g for both the 1 wt% and 3 wt% nickel loading scenarios. This surface area is a 38% increase in surface area from the GO precursor (206 m<sup>2</sup>/g) but is still a 54% reduction in surface area from pure graphene (620 m<sup>2</sup>/g). The appreciable increase in surface area from the GO precursor is due to the more complete exfoliation and more uniform CNF distribution in the samples prepared from a graphene precursor. The decrease in surface area from that of pure graphene is again due to the inclusion of nickel catalyst sites in the matrix. Moreover, the surface area was calculated to be



identical regardless of the amount of nickel loading as suspected by investigation of the microstructure. The identical surface areas between the 1 wt% and 3 wt% nickel loading is due to low levels of loading and is confirmed visually by the above micrographs.

Though the characterization of the aqueously prepared samples from graphene precursors is complete, this manuscript would be remiss if this final microstructure was not examined. The most significant micrograph in terms of proof of concept is shown in Figure 39 which is an edge-on view of a graphene honeycomb from an aqueously prepared G/CNF/Ni structure with graphene as a precursor. The significance of Figure 39 is the indication of carbon nanofibers growing between the sheets of graphene, further exfoliating the graphene sheets and providing electrical and ionic connections between said sheets as presupposed by this manuscript. This image provides evidence the novel synthesis method detailed in this study, growing the carbon nanofibers directly upon the graphene sheets *in situ*, does produce a three-dimensional graphene-carbon nanofiber architecture containing nickel.

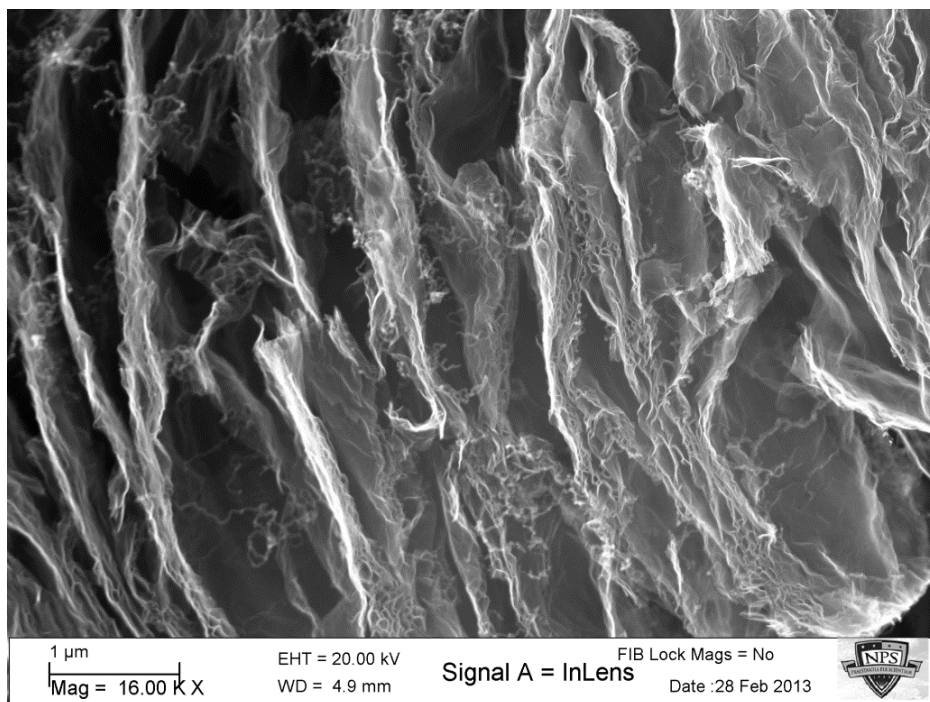


Figure 39. SEM image of aqueously prepared graphene-CNF sample from a graphene precursor and 1 wt% nickel loading, G/CNF/Ni-1%. Note the CNF growth in between the sheets of exfoliated graphene.



## 2. Dry Preparation

### *a. Graphite Oxide Precursor*

The first dry prepared graphene-CNF structures analyzed are those which were prepared from graphite oxide precursors and this analysis begins with examining the microstructure. Figure 40 illustrates the microstructure of dry prepared graphene sheets interlaced with nickel nanoparticles beginning with a GO precursor. Immediately, it is evident that the nickel nanoparticles for the dry preparation method differ significantly from those of the aqueous preparation method. The main difference in the nickel catalysts between the two preparation methods is that there was greater uniformity with respect to the particle size for the samples prepared via the dry preparation method. This is indicated by the increased difficulty in locating the nickel nanoparticles in the dry prepared samples. The nickel defect sites were far easier to identify in the aqueously prepared graphene sheets intercalated with nickel nanoparticles as indicated by Figures 33(a), 35(a), and 36(a). This reason it was increasingly difficult to locate the nickel catalysts in the dry prepared samples is because the particles on average were much smaller for dry prepared samples as compared to those of the aqueous prepared samples. Nearly all nickel nanoparticles were on the order of 10s of nm (~30 nm) in diameter in the samples generated by the dry preparation method as seen in Figure 40(b). This is further evidence the large (>100 nm) aggregate nickel particles found in the aqueously prepared microstructures were a result of the synthesis process; whereas the nickel salt was dissolved in the aqueous preparation and subsequent nucleation led to nickel agglomerate particles, the dry method differed significantly. During the dry synthesis, the nickel salt was reduced in a solid state by losing nitrate groups and being reduced by interaction with urea. Once the nickel salt is reduced to nickel particles, they are covered with a small carbon (amorphous) shell that prevents the agglomeration between particles, and thus, the uniform nickel nanoparticle size of smaller dimension.

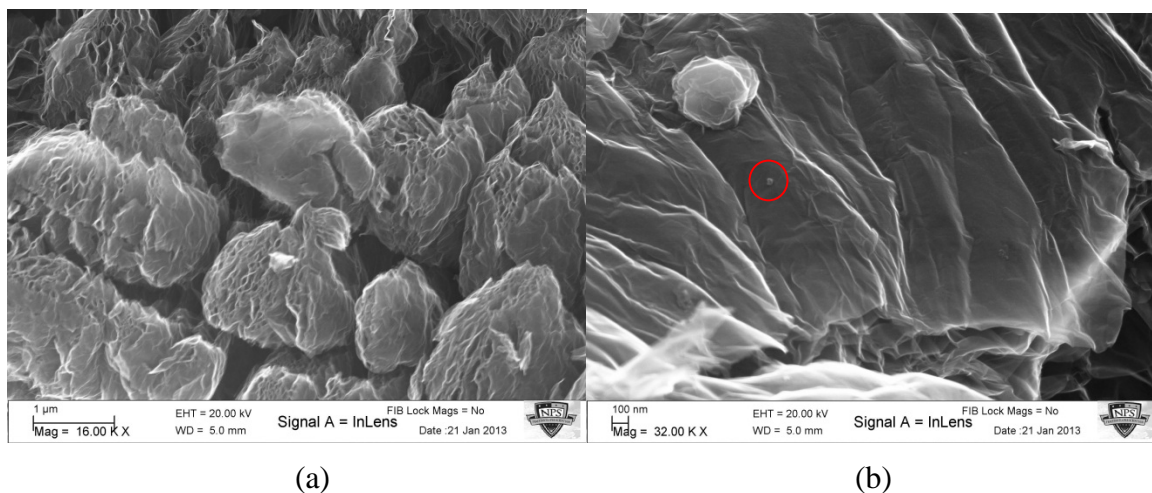


Figure 40. SEM images of dry prepared graphene layers with nickel nanoparticles from a GO precursor (G/Ni) at (a) 16k and (b) 32k magnification. Note the nickel catalyst in (b).

The direct result of the homogenous particle size distribution is homogeneously sized carbon nanofiber growth. The dry prepared samples have both greater CNF dispersion (Figure 41(a)) and size uniformity (Figure 41(b)) than do the similarly prepared aqueous architecture. These features occur because of the uniformity of the nickel nanoparticles interlaced within the graphene matrix of the dry prepared specimens. The uniform size of the CNF and more complete CNF distribution amongst the dry prepared samples are indicative of an expected higher surface area for the dry samples as compared to the aqueous. However, as described earlier, the aqueous samples have significantly larger surface area values than do the dry samples and that is directly attributed to the flap-like structure along the larger carbon nanofibers found in the aqueous samples.

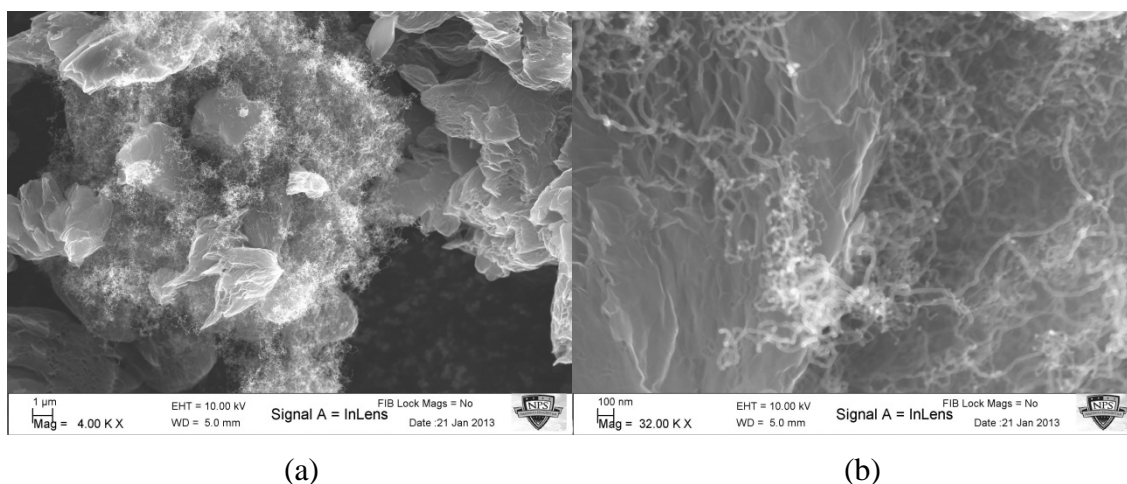


Figure 41. SEM images of dry prepared graphene-CNF (G/CNF/Ni-3%) structure from a GO precursor at (a) 4k and (b) 32k magnification.

The second means by which the dry prepared graphene-CNF matrix from a graphite oxide precursor was characterized was with BET analysis, which yielded a value of  $79.6 \text{ m}^2/\text{g}$ . This surface area calculation is significantly smaller than that of the aqueous counterpart of  $206 \text{ m}^2/\text{g}$ . This significant reduction in specific surface area from the aqueously prepared sample to the dry confirms that despite the uniform fiber size and CNF distribution within the graphene matrix, the surface area for the aqueous sample dominates as a result of the flap-like feature on the larger carbon nanofibers.

### ***b. Graphene Precursor***

Graphene-CNF architectures were also prepared via the dry method with graphene as a precursor, similarly to the aqueous method described in the previous section. Furthermore, the differences between the dry samples with graphene precursor as compared with the dry samples from the GO precursor are similar to those described previously in the aqueously prepared section. To reiterate, there is better exfoliation of the graphene (due to the synthesis process essentially exfoliating the graphene twice) and a greater dispersion of nickel nanoparticles amongst the graphene layers (Figure 42) in the structure with graphene as a precursor compared with the graphite oxide precursor. This directly results in a more uniform distribution of carbon nanofibers (Figure 43) in the sample from a graphene precursor as compared with that of the GO precursor. As

described earlier, the preparation from previously exfoliated graphene allows for more complete exfoliation and permits easier dissemination of the nickel nanoparticles within the graphene sheets. Moreover, greater exfoliation combined with more uniform fiber distribution each indicate greater surface area (confirmed with BET 181 m<sup>2</sup>/g for sample with graphene precursor compared with 79.6 m<sup>2</sup>/g for the sample from GO precursor) and, potentially, greater electrical characteristics for the sample prepared with graphene as a precursor when compared to the same sample prepared with GO as a precursor.

Lastly, the differences between aqueous preparation methods and dry preparation methods detailed in the GO precursor section are also evident for the samples with graphene as the precursor. Despite the clear advantage in nickel catalyst size homogeneity and fiber distribution uniformity, the graphene-CNF composite prepared using the aqueous method with graphene as a precursor has a significantly larger surface area than does that of the dry sample due to the extra surface area of the flap-like features. This is further elucidated by the BET characterization which yields a surface area of 181 m<sup>2</sup>/g for the dry architecture and 284 m<sup>2</sup>/g for the aqueous counterpart.

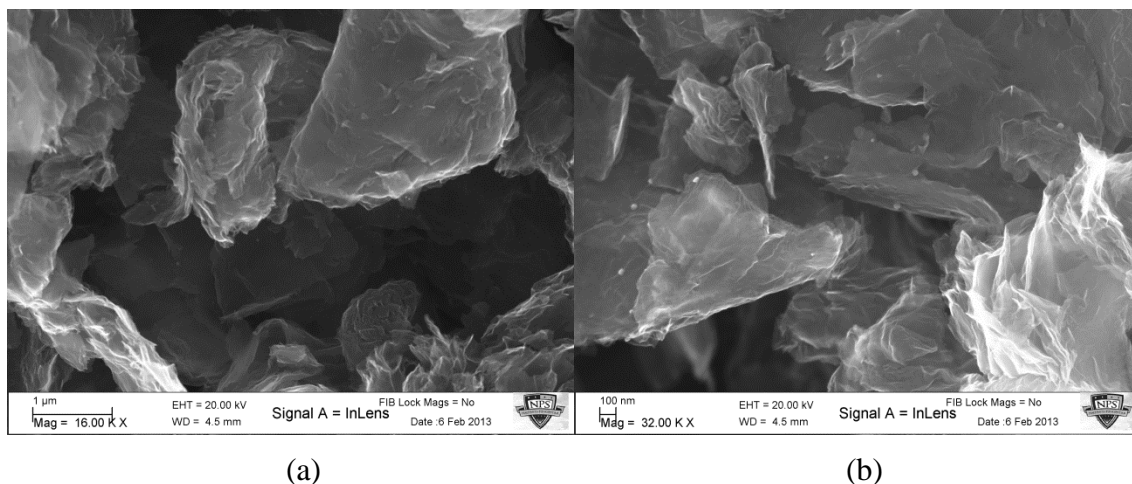


Figure 42. SEM images of dry prepared graphene samples with nickel nanoparticles from a graphene precursor, G/Ni at (a) 16k and (b) 32k magnification.

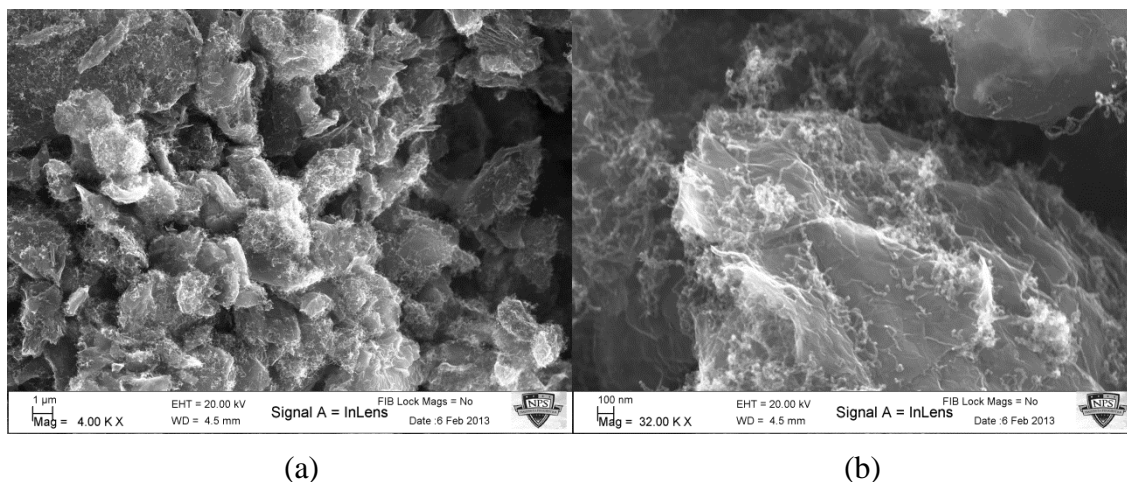


Figure 43. SEM images of graphene-CNF architecture prepared via the dry method with a graphene precursor, G/CNF/Ni at (a) 4k and (b) 32k magnification.

## E. OXIDIZED SAMPLES

Though the oxidation of the nickel nanoparticles within the graphene-CNF matrices and the CNF blank samples to take advantage of the pseudocapacitance effect has been discussed at length, one detail regarding the oxidation procedure requires justification: the chosen oxidation temperature of 400°C as mentioned in Chapter II. The oxidation temperature at 400°C was chosen to simultaneously prevent carbon burn off (from graphene matrix or CNF) and maximize nickel oxidation.

In order to determine the appropriate oxidation temperature, TGA was performed on a carbonaceous nickel powder sample (created by the reduction of nickel (II) nitrate hexahydrate with urea) with the resulting output shown in Figure 44. The thermal analysis experiment began at room temperature and finished at 750°C with a constant heat rate of 5°/min and occurred in an oxidant atmosphere. The results of the TGA yield the expected increase in mass due to Ni forming NiO up to ~475°C and then the 13.2% decrease in mass due to loss of carbonaceous material. Thermal experiment results determined the selection of 400°C as the oxidation temperature for the syntheses involving graphene-carbon nanofiber architectures and the carbon nanofiber blank samples; 400°C is a high enough temperature to allow for nickel oxidation but not sufficiently high to begin significant carbon burn off from the graphene or nanofibers.

Additionally, as described in section D of this chapter, due to the superior surface area performance of the aqueously prepared samples from a graphene precursor, not only was the nickel loading adjusted to examine the effects of nickel loading on electrical characteristics, but also the nickel was oxidized in an effort to increase specific capacitance by utilizing the pseudocapacitive effects, creating a hybrid supercapacitor. The oxidized samples were characterized via BET, which calculated specific surface area at 335 m<sup>2</sup>/g regardless of the nickel loading. The 18% increase in surface area (as compared with aqueously prepared G/CNF/Ni samples) from the oxidation process is directly attributed to the pitting of the graphene sheets during oxidation. Additionally, this increase in surface area indicates the oxidized samples will have greater electrical characteristics not only due to the pseudocapacitive effects but also superior surface area.

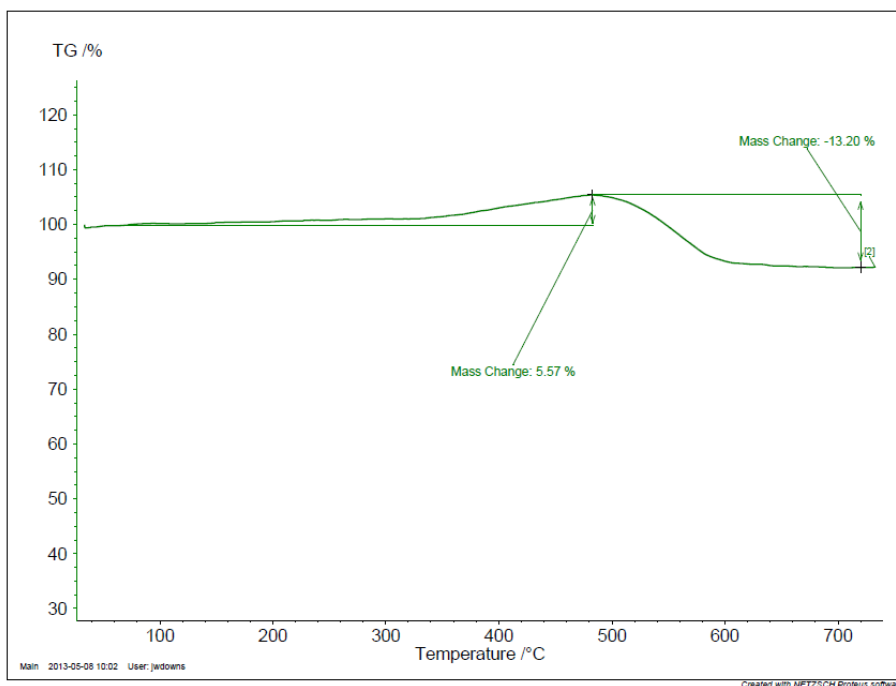


Figure 44. TGA results of nickel oxidation procedure.

## F. SURFACE AREA CHARACTERIZATION SUMMARY

The principal objective of this manuscript is the novel synthesis of a three-dimensional graphene-CNF architecture with either nickel or nickel oxide with a large

specific surface area for use as electrode material of the same. The primary indicator as to whether a graphene-CNF structure would be a good candidate for electrical testing was specific surface area. The more specific surface area an electrode possesses, the greater the space for the electric double layer, and the larger the specific capacitance. As such, the graphene-carbon nanofiber materials synthesized herein were all measured via BET surface area analysis. Moreover, for comparison, the carbon nanofiber blank samples and pure graphene samples were also measured. Lastly, the nickel nanoparticles in each of the aqueously prepared samples from graphene precursors as well as the carbon nanofiber blank samples were oxidized in an attempt to increase specific capacitance as a result of the pseudocapacitive behavior. Surface area characterization of these samples was also performed.

The first material which was characterized via BET was pure graphene. This value was used as a reference point to which the remaining architectures would be compared and was determined to be  $620 \text{ m}^2/\text{g}$ , which compares favorably to numbers reported in literature [27, 54, 55].

Following the surface area characterization of pure graphene, the BET analysis of the graphene-CNF structure with nickel began. Initially, both methods for generating graphene-CNF matrices, the aqueous and dry preparation methods, were employed with constant nickel loading of 3 wt%. Additionally, both methods for disseminating the nickel nanoparticles amongst the graphene sheets, directly upon GO precursor and using previously exfoliated graphene, were performed with each preparation method, and thus, four graphene-carbon nanofiber networks each with 3 wt% nickel loading were initially created and evaluated: aqueously prepared samples from both GO and graphene precursors and dry prepared samples from both GO and graphene precursors, all with 3 wt% nickel loading. These first four structures were then analyzed via BET with the results shown in Figure 45.

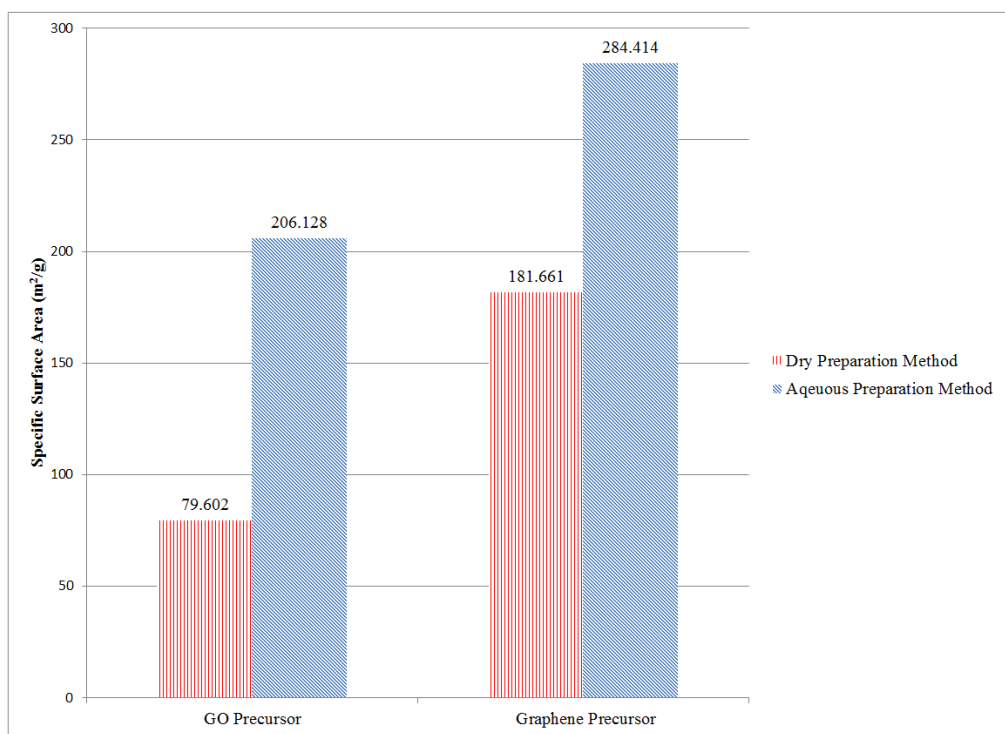


Figure 45. Surface area comparison between precursors and preparation methods with a constant nickel loading (3 wt%).

The essential conclusion drawn from the surface area analysis in Figure 45 was that for either precursor the aqueous preparation method had superior specific surface area values (i.e., 284 m<sup>2</sup>/g compared with 181 m<sup>2</sup>/g for graphene precursor). This fact had been well documented throughout the examination of the microstructures of the graphene-CNF architectures. Though one may reason the homogeneous fiber distribution and size profile, specifically smaller fiber sizes, generated via the dry method as compared to the aqueous preparation method should indicate larger surface area, the large CNF found in the aqueously prepared samples have a flap-like structure along the length of the fibers which dramatically increases the available surface area of the composite.

A second principal observation from the surface area analysis in Figure 45 is that regardless of the preparation method, synthesis with graphene as the precursor had significantly higher specific surface area numbers (nearly a 100 m<sup>2</sup>/g increase for both methods). This is due to the more complete exfoliation of the graphite oxide as the GO is essentially exfoliated two times during the synthesis. The nickel catalyst addition



procedure begins with thermally exfoliated graphene and the graphene is subsequently exfoliated a second time as a result of the high temperature urea reduction of nickel salt to nickel nanoparticles, with the urea performing the vital role of simultaneously reducing the nickel salt and exfoliating the graphene. As a direct result of more complete exfoliation, the nickel particle distribution is greater in the case with graphene as a precursor as compared with those from a GO precursor. It is easier for the nickel catalysts to evenly disseminate within the graphene layers and this leads to greater fiber distribution as well as greater exfoliation of the graphene sheets due to fiber growth. The better exfoliation and nickel particle propagation produces higher surface area values in the architectures created from a graphene precursor as opposed to those from a graphite oxide precursor.

The final discussion topic when examining Figure 45 is the nearly 50% decrease in specific surface area from that of pure graphene to the 3D architectures. This lowering in specific surface area is directly attributed nickel catalyst sites inside the composite matrix. Electrical characterization will determine if the nearly 50% reduction in specific surface area is outweighed by the increased conductivity provided by the combination of nickel particles and carbon nanofibers interlaced within the graphene layers including the increased capacitance provided by the pseudocapacitive effects upon oxidizing the sample.

Upon discovering the aqueous preparation method had superior surface area capabilities, further modification to the architecture occurred in an attempt to maximize surface area and conductivity. The nickel loading was adjusted to 1 wt% and samples were oxidized in an effort to take advantage of hybrid supercapacitor behavior. The resulting surface area analysis is illustrated in Figure 46.

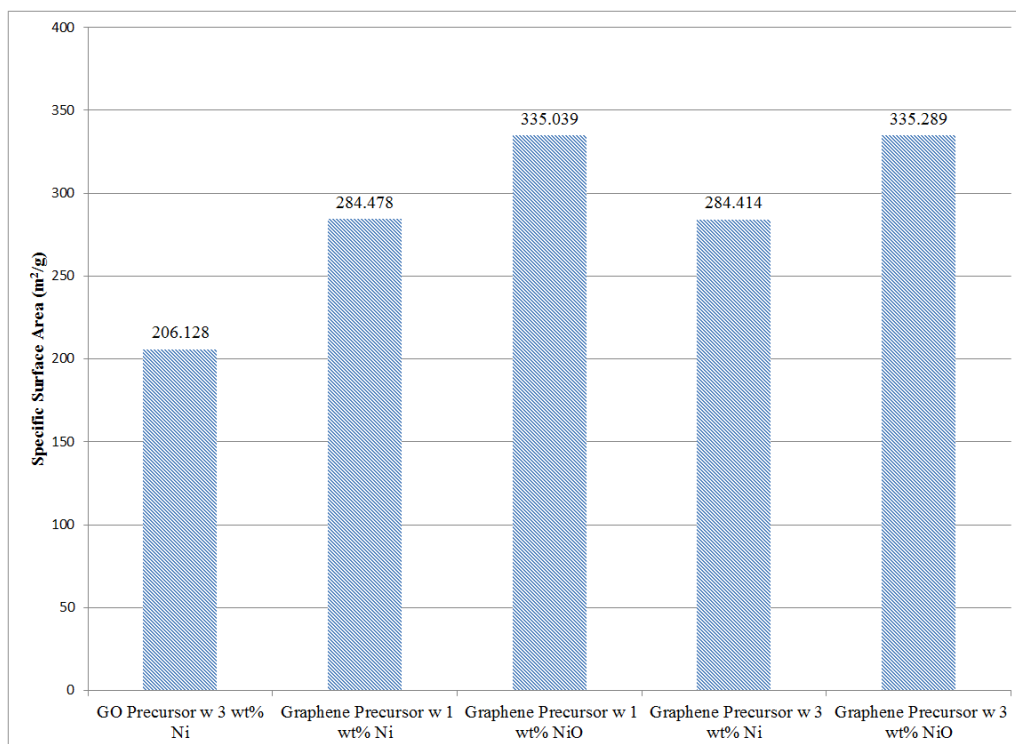


Figure 46. Surface area comparison for the aqueously prepared samples as a function of precursor, nickel loading and oxidation status.

Examination of the various surface areas of the aqueously prepared samples provides several conclusions. First, as stated above, graphene as a precursor has a substantial specific surface area advantage when compared to structures employing graphite oxide as the precursor. Secondly, the surface area is nearly identical when comparing samples with varied nickel loading (between 1 and 3 wt%). This is due to the overall low nickel loading and was demonstrated previously when analyzing the scanning electron micrographs of the two loading scenarios. No exfoliation, nickel particle distribution, or fiber growth differences are readily discernible when inspecting the SEM images which would indicate the two samples would have similar surface area values that are confirmed via BET results (284 m<sup>2</sup>/g for each of the 1 wt% and 3 wt% samples without oxidation). The final conclusion drawn from Figure 46 is that the oxidation of the nickel particles improves the surface area (from 284 m<sup>2</sup>/g to 335 m<sup>2</sup>/g for 3 wt% nickel loading) in all cases. The surface area increases for the graphene-CNF structures after the oxidation process because of slight pitting of the graphene sheets during the

oxidation procedure, essentially creating dimpled surfaces increasing the specific surface area. Combine the higher surface area numbers with the pseudocapacitive effect from the faradaic redox type charge transfer resulting for the transition metal oxide (NiO), and the graphene-CNF samples containing NiO possess the greatest potential for standout electrical performance.

The last samples to be characterized via surface area analysis were the carbon nanofiber blank samples, which were synthesized absent of graphene for comparison with three-dimensional graphene-CNF matrices. The BET analysis performed for the carbon nanofiber blank samples are displayed in Figure 47.

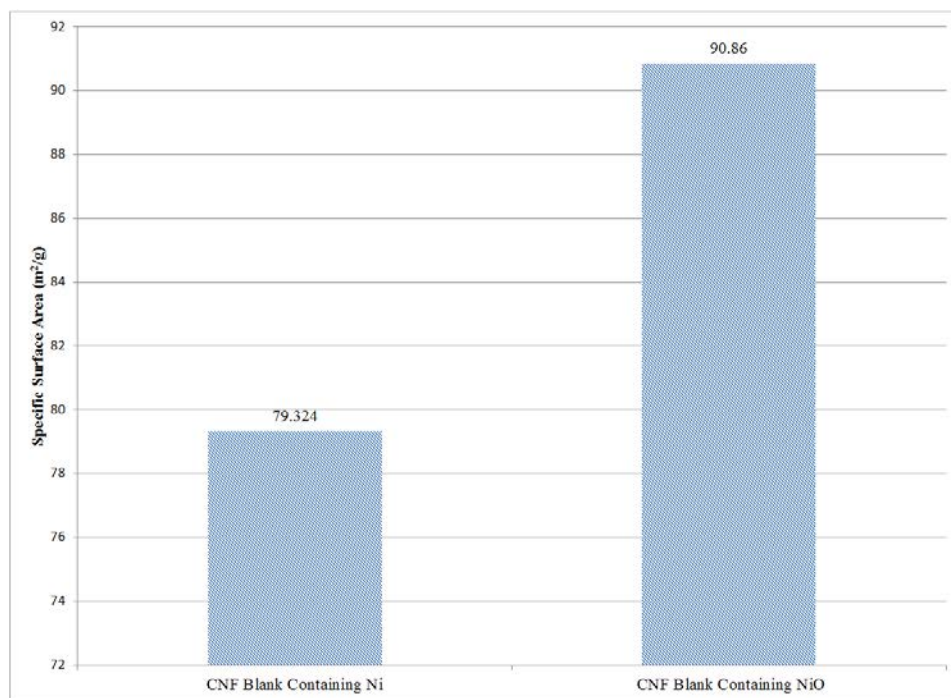


Figure 47. Surface area comparison for the CNF blank samples as a function of oxidation status.

It is clear from Figure 47 that the CNF blank surface area is inferior to the graphitic architecture as expected because of the amorphous carbon from which these fibers were grown. Additionally, as detailed previously, though the carbon nanofiber

sample is devoid of graphene, amorphous carbon still exists at the base of the nanofibers and as such the oxidized sample surface area increases due to the sintering of the carbon during the oxidation process.

Finally, in order to summarize the surface area analysis of the graphene-CNF architectures generated herein, there are several important take-aways:

- Graphene-CNF materials containing nickel have a surface area of ~50% that of pure graphene due to the inclusion of nickel nanoparticles in the graphene matrix.
- The aqueous preparation method yielded the highest surface area values regardless of precursor.
- Graphene as a precursor yielded higher specific surface area numbers when compared to samples which employed a GO precursor regardless of the preparation method.
- At low nickel loading (such as 1 wt% and 3 wt%), no discernible difference in surface area is seen.
- Oxidation of nickel particles within a carbonaceous sample at 400°C increases surface area of the sample due slight pitting of the carbon.

Therefore, as a result of the above, in order to maximize specific surface area of a graphene-CNF structure, prepare it via the aqueous method from a graphene precursor and subsequently oxidize the nickel nanoparticles.

## **G. ELECTRICAL CHARACTERIZATION**

The primary objective of this work was the novel synthesis of a three-dimensional graphene-carbon nanofiber network containing either nickel or nickel oxide to employ as electrode material for use in energy storage devices, specifically supercapacitors. After performing BET characterization, it was evident the aqueously prepared architecture had superior surface area traits, and thus only the aqueously prepared samples were chosen for further experimentation and ultimately electrical testing. Consequently, the nickel loading values (1 wt% and 3 wt%) were varied with the aqueously prepared graphene-

CNF samples as well as oxidizing the nickel nanoparticles of the same. These aqueously generated structures were then carried forward to electrical characterization along with a pure graphene sample, a carbon nanofiber blank sample containing nickel, and a carbon nanofiber blank sample containing nickel oxide. Therefore, seven separate materials were classified electrically: aqueously prepared graphene-CNF structures with 1 wt% Ni (G/CNF/Ni-1%), 1 wt% NiO (G/CNF/NiO-1%), 3 wt% Ni (G/CNF/Ni-3%), and 3 wt% NiO (G/CNF/NiO-3%), pure graphene (G), CNF blank sample with Ni (CNF/Ni), and CNF blank sample with NiO (CNF/NiO).

Electrical testing of the afore mentioned materials was performed by passing a 5Hz square wave through a 100  $\Omega$  resistor and the test capacitor in series. The test cell was constructed as described in the Chapter III. The output wave characteristics across the test capacitor were captured and MATLAB was used to plot both the complete output waveform as well as the charging portion of the curve plotted against a normalized charge voltage. These two curves can be seen side by side in Figures 48–50 for each of the materials listed previously.

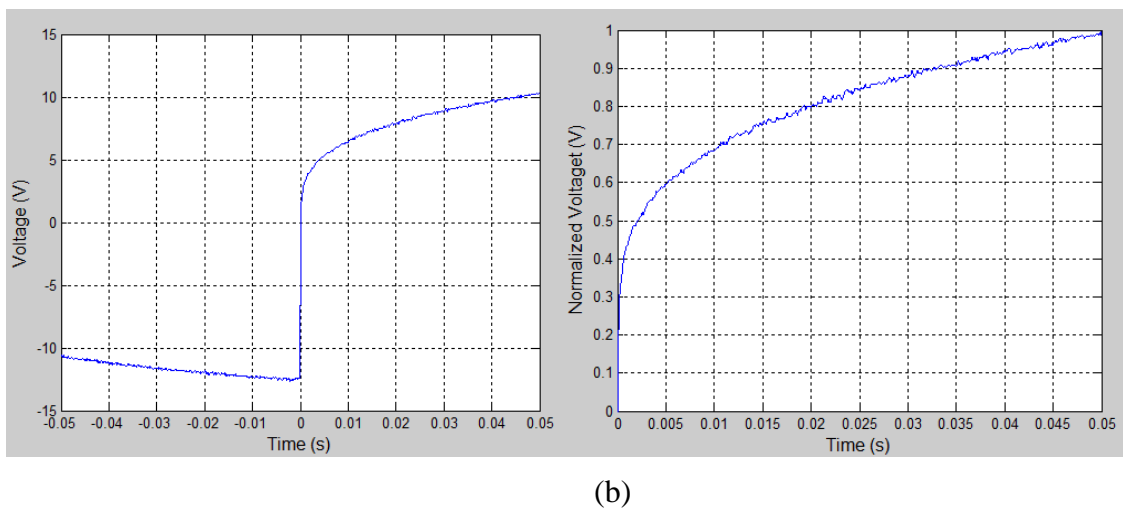
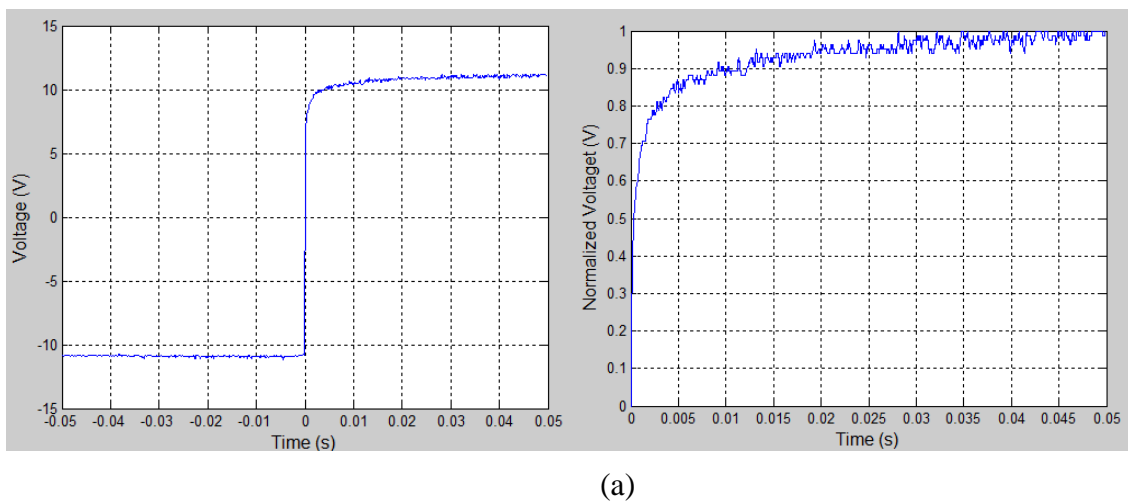
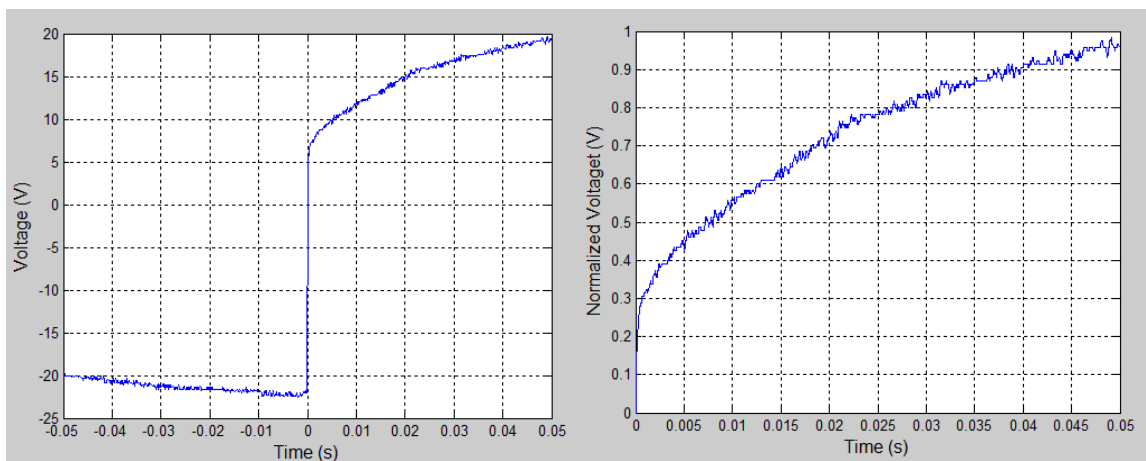
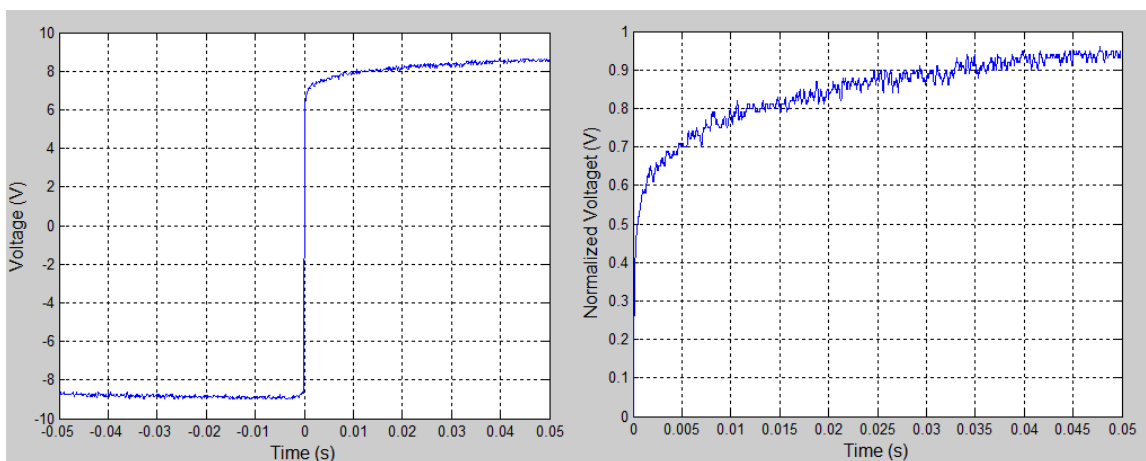


Figure 48. Full output waveform and normalized charge curves for (a) aqueously prepared G/CNF/Ni-1% (b) aqueously prepared G/CNF/NiO-1%

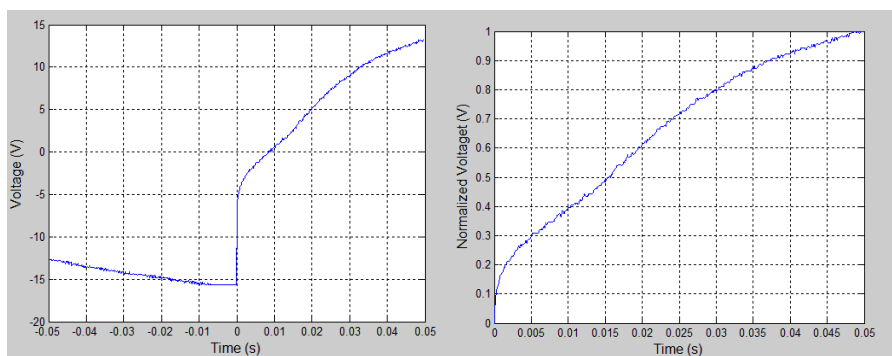


(a)

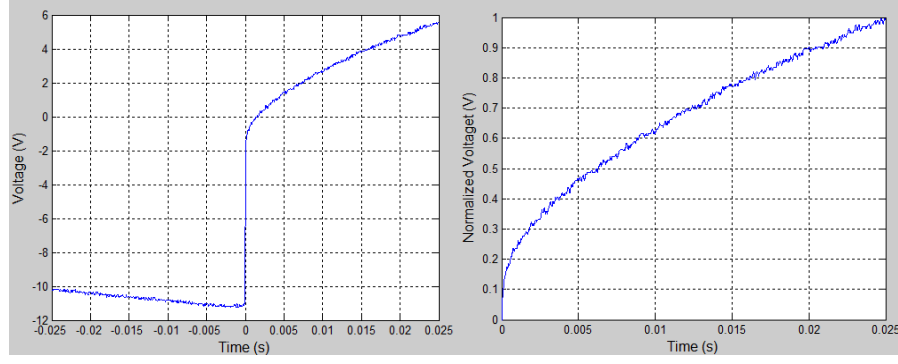


(b)

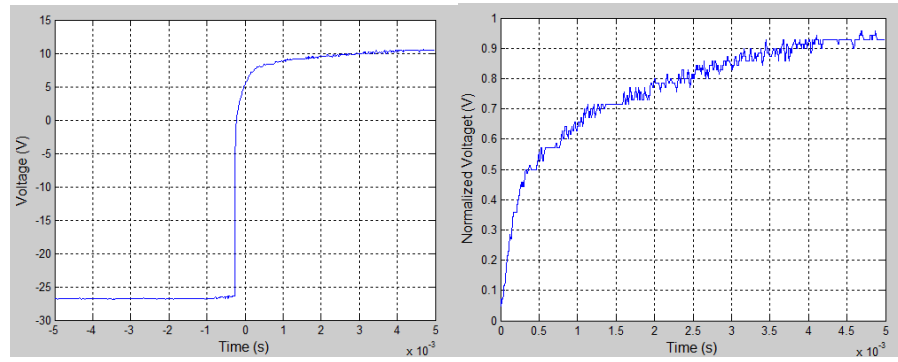
Figure 49. Full output waveform and normalized charge curves for (a) aqueously prepared G/CNF/Ni-3% (b) aqueously prepared G/CNF/NiO-3%



(a)



(b)



(c)

Figure 50. Full output waveform and normalized charge curves for (a) CNF/Ni (b) CNF/NiO and (c) pure graphene.

After capturing and modeling the test capacitor waveforms for each of the seven synthesized materials described previously, the specific capacitance was calculated via two separate means for comparison. First, an exponential curve fit was applied the normalized charge curve in the form of equation 3 (Figure 51(a)) where the exponential term was equal to  $(-1/RC)$ . Knowing the resistance in the circuit, the capacitance was easily determined. The second means for determining capacitance of the test cell was to plot the normalized charge curve the form of equation 4 (Figure 51 (b)). The slope of the best fit line then equaled  $(-1/RC)$  and the capacitance was again easily determined. These two methods for determining capacitance values were compared for consistency. Finally, specific capacitance was calculated by dividing the empirically determined capacitance values by the weight of synthesized material on each electrode. The results of the



specific capacitance calculations are summarized in Table 4 and the electrical characterization is summarized visually simultaneously with the surface area analysis in Figure 52.

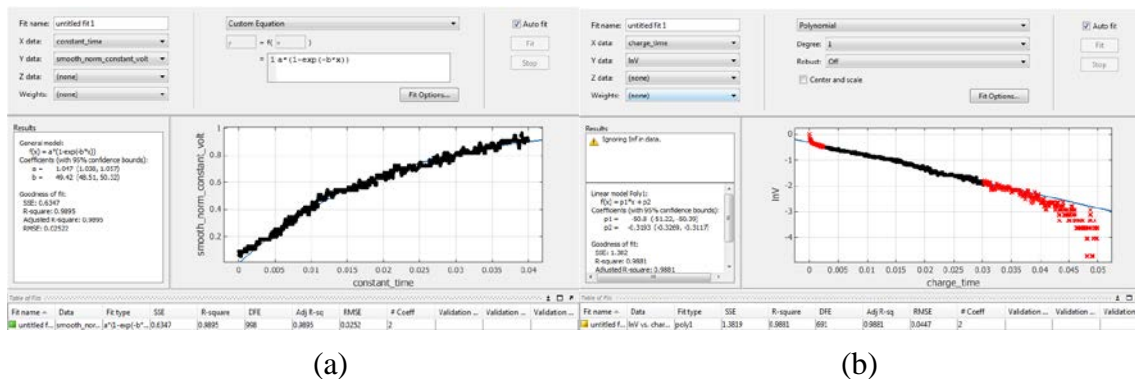


Figure 51. (a) Exponential curve fit of equation 3 and the (b) linear curve fit of equation 4 for the aqueously prepared G/CNF/Ni-3 wt% Ni.

Table 4. Summary of electrical characterization

Sample	Nickel Loading (wt%)	Oxidized	Specific Capacitance (mF/g)
<b>Aqueous Preparation Method</b>	1	N	70.9
	1	Y	120
	3	N	340
	3	Y	361
<b>CNF Blank</b>	10	N	139
	10	Y	100
<b>Graphene</b>	No nickel added.	NA	98.3

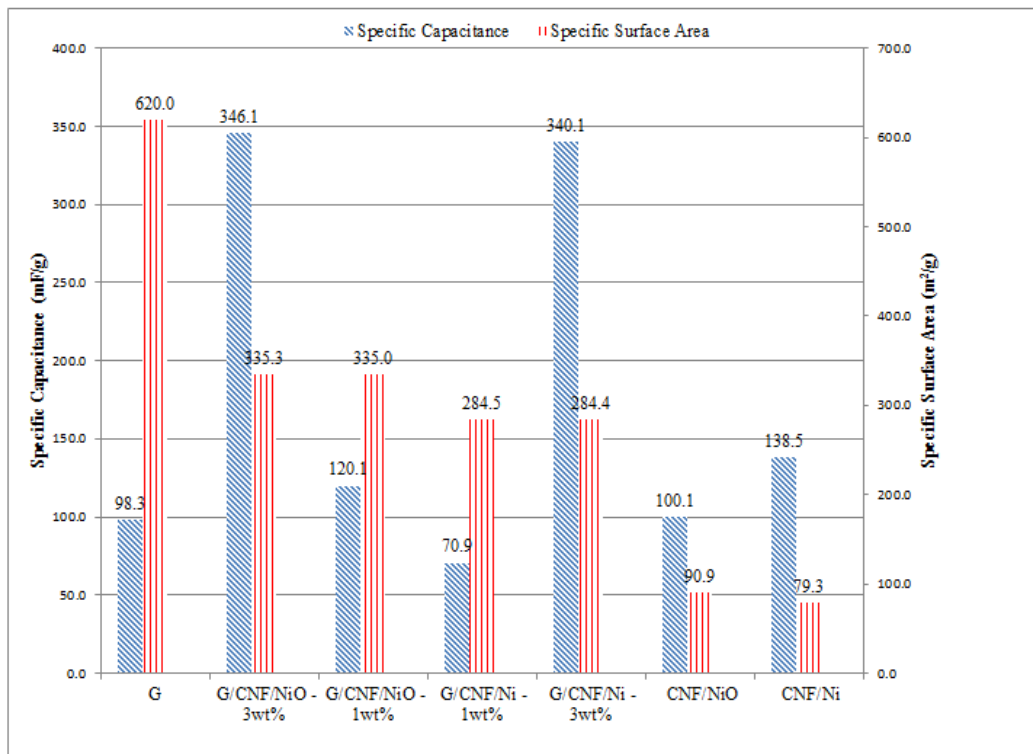


Figure 52. BET and specific capacitance summary.

Upon completion of the specific capacitance calculations and combined with the surface area analyses, several critical observations from Figure 52 can be made. The first such observation is the effect of nickel loading on specific capacitance. Though the specific surface areas are nearly identical when comparing the aqueously prepared graphene-CNF samples of various nickel loading, the specific capacitances are three to five times greater for the graphene-carbon nanofiber architectures with the higher nickel loading (3 wt% as opposed to 1 wt%). This indicates the nickel loading is an essential factor to improved supercapacitor performance. This is also corroborated by the increase in specific capacitance from the pure graphene sample to the graphene-CNF samples containing either Ni or NiO. Moreover, this dramatic increase in specific capacitance proves the hypothesis that the sacrifice in surface area from pure graphene to the 3D structures due to the addition of nickel particles into the matrix is compensated for by increased conductivity within the structure. There exists, however, an optimal nickel loading as evidenced by the increase in capacitance behavior between the 1 and 3 wt% loading combined with the drop in those same characteristics between the 3 wt% loaded

sample and the CNF blank sample, and as such, further testing is required to optimize the nickel loading within the graphene-CNF matrix to ensure the strongest electrical performance.

The second observation from Figure 52 the effect of specific surface area on specific capacitance is far outweighed by that of nickel loading. The aqueously prepared sample with 1 wt% NiO has a larger surface area than that of the aqueously prepared sample with 3 wt% Ni ( $335 \text{ m}^2/\text{g}$  and  $284 \text{ m}^2/\text{g}$ , respectively), yet the latter has a specific capacitance nearly three times that of the former. Along that same argument, pure graphene has a specific surface area twice that of the aqueously prepared sample with 3 wt% NiO, yet pure graphene's specific capacitance is less than one third that of the graphene-CNF sample. This is evidence that while surface area does contribute to specific capacitance, specifically electric double layer capacitance, the nickel content exceeds surface area's contribution to the overall specific capacitance due to the increased conductivity of the nickel nanoparticles within the matrix.

To that end, the next conclusion drawn from Figure 52 is the effect of oxidation on specific capacitance behaviors. Graphene-CNF samples containing nickel were placed in an oxidant environment at  $400^\circ\text{C}$  to oxidize the nickel nanoparticles in an attempt to capitalize on the pseudocapacitive effects of the faradaic redox type reactions of transition metal oxides. The efficacy of the NiO pseudocapacitance appears inconclusive by examining Figure 52. While in each of the graphene-CNF structures, the specific capacitance does increase for the oxidized structures, the increase is very dramatic for 1 wt% NiO loading (a 69% increase from the 1 wt% Ni loading) and very subtle for the 3 wt% NiO loading (only a 6% increase from the 3 wt% Ni loading). Additionally, the specific capacitance lowered from the CNF blank sample with Ni to the CNF blank sample with NiO. The specific capacitance of the CNF blank sample decreases after the oxidation process most probably because of the loss of conductive carbon during the oxidation procedure.

There is much ongoing research into developing supercapacitors with the pseudocapacitive effects of transition metal oxides [28–34] because of their significant improvement in the specific capacitance of said supercapacitors. Kwon et al. [28] reports

ruthenium oxides have been shown to provide specific capacitances as high as 1300 F/g. Furthermore, Zhao et al. [34] quotes developing hybrid type capacitors which utilize  $\alpha$ -Fe<sub>2</sub>O<sub>3</sub> and multi-walled carbon nanotubes (MWNT) which display an energy density eight times that of similar electrodes using only MWNT. These are significant findings with respect to the work performed in this thesis. Though the graphene-CNF structure containing 3 wt% NiO only increased in specific capacitance by 6% over that of the graphene-CNF sample with 3 wt% Ni, it was more than a three and a half times the specific capacitance of either the CNF blank sample or the pure graphene sample. This three and a half times increase in specific capacitance between the G/CNF/NiO-3% sample and the specific capacitance of either of its constituents (CNF blank with NiO or pure graphene) is similar to values published by both Kwon et al. and Zhao et al. [28, 34]. This is evidence that the oxidation procedure combined with the novel synthesis of a three-dimensional graphene-CNF matrix by growing the CNF directly upon the graphene layers *in situ* provides similar improvements to the electrical properties to the composite material when compared to its constituents as shown in recent literature. The CNF intercalated within the graphene sheets aids in both ion and charge transfer between the graphene layers and combined with the pseudocapacitive effects of NiO, a substantial improvement in specific capacitance is achieved by growing carbon nanofibers within the graphene matrix when compared with the performance of either CNF or pure graphene individually.

The final note on the discussion of the effects of oxidizing the samples is the large discrepancy between the increase in specific capacitances from the 1 wt% sample to the 3 wt% samples (69% and 6%, respectively). With a limited number of trials and nickel loading values, little can be summarized from these results. Perhaps, as the nickel loading increases, the pseudocapacitance effects are minimized due to the already significant specific capacitance values. Further tests both with similar nickel loading values and also with various other nickel loading values would be required to fully evaluate the trend in increase of specific capacitance with respect to oxidizing the nickel nanoparticles.

The last discussion topic from the examination of Figure 52 is the comparison of the calculated specific capacitance values of the materials synthesized herein with recently published values of similar architectures. The specific capacitance values determined in this manuscript are all on the order of hundreds of mF/g. This is in stark contrast to values quoted in recent studies: Zhu et al. [56] cite a specific capacitance of microwave exfoliated graphene electrodes of 200 F/g, Liu et al. [57] quote a capacitance of 154 F/g for graphene electrodes, and Kwon et al. [28] report values of 174 F/g for nanohybrid capacitors involving MnO<sub>2</sub>, CNF, and graphene. The published values are all three orders of magnitude larger than those detailed in this manuscript.

There are many reasons for the large discrepancy in specific capacitances determined by this study and those reported in recent literature, with the most important being the separate electrical characterization techniques. The electrical testing in literature is largely performed via cyclic voltammetry (CV), the procedure of holding a constant voltage scan rate on the order of mV/s in a very limited voltage range and measuring the current across the capacitor. From this data, specific capacitance can be determined. This method of testing provides a much more controlled charge and discharge performance of the capacitor under test. Contrast this to the testing performed in this study in which a function generator supplied a 20V square wave at a frequency of 5 Hz to the capacitor, charging and discharging the test capacitor five times per second. This rapid cycling limited data resolution for the capacitor data collection and, as such, specific capacitance comparisons with recently published data is inapplicable due to the significant differences in electrical characterization. Therefore, specific capacitance comparisons from this study should only be compared herein.

Finally, to summarize the electrical characterization there are several important conclusions:

- The nickel loading content effects far outweighs the surface area effects with regard to specific capacitance values.

- The combination of a graphene-CNF matrix with NiO nanoparticles improves on the specific capacitance of either of the individual components (CNF blank samples or pure graphene) by three and a half times, similar to other values in literature.
- Specific capacitance values for similar architectures in recent research are quoted three orders of magnitude higher than those cited in this manuscript. The large discrepancy is due to vastly different electrical characterization methods.

The work demonstrated in this study validates the original hypothesis. A three-dimensional graphene-CNF architecture containing either nickel or nickel oxide was synthesized in a novel manner by growing the carbon nanofibers directly on the graphene layers *in situ*. This 3D structure was then converted to electrode materials for use in supercapacitors. Subsequent electrical measurements verified a substantial improvement in specific capacitance from the individual constituents (graphene and CNF) to the graphene-CNF composite material due to the CNF improving ion and charge transfer within the graphene matrix and additional pseudocapacitance effects from the NiO. This confirms that the synthesis protocols contained herein can be successfully employed to create the desired three-dimensional architectures, improving on electrical performance.

## V. CONCLUSION

### A. MILESTONES

Three-dimensional graphene-carbon nanofiber architectures containing nickel were synthesized in a novel manner by growing the carbon nanofibers directly upon the graphene layers *in situ*. The use of the Reduction Expansion Synthesis that uses urea to produce finely divided nickel particles, which served as catalyst for the carbon nanofiber growth, was instrumental for the success of the protocol. Following creation of the 3D structures, namely G/CNF/Ni, the nickel nanoparticles in those structures were oxidized in an effort to capitalize on the pseudocapacitive effect of transition metal oxides and produce G/CNF/NiO. Electrodes of both types of materials were deposited in current collectors and included in cell geometries and then tested as supercapacitors.

The summary of primary conclusions that verify the hypotheses presented in Chapter I of this manuscript follow:

- The innovative method for generation of 3D graphene-CNF materials described in this work was successful. Evidenced by inspection of the microstructure via scanning electron microscopy, the composite material presents carbon nanofibers intercalated in between graphene layers. The nickel catalyst initially attaches to the graphene surface and when the carbon fiber grows the particle migrates to the front of the fiber, leaving the fiber in direct contact with the graphene.
- The composites G/CNF/Ni and G/CNF/NiO (both 1 and 3 % Ni loadings) displayed high specific surface areas. The aqueously prepared sample from a graphene precursor G/CNF/Ni and G/CNF/NiO with 3 wt% nickel loadings measured 284 and 335 m<sup>2</sup>/g respectively. Values of surface areas have been found to have a direct impact on supercapacitor performance.
- Oxidation of the nickel nanoparticles in the graphene-CNF structures added two main benefits to the composite material: first, the increased surface area available to use in the electric double layer, and second, the

pseudocapacitive properties of the faradaic redox type reactions of a transition metal oxide, which combined provided higher capacitance values.

- The G/CNF/NiO architectures demonstrated a substantial improvement in specific capacitance over that of each of the individual components (graphene or CNF). The specific capacitance increased by 350% from either graphene or CNF to the 3D combined materials.
- The nickel loading variation, limited to 1 and 3% (composites of G/CNF/Ni-1% and 3%, as well as G/CNF/NiO-1% and 3% were studied) did not present significant variations in terms of surface area values. The loading difference did impact the capacitance values, showing that higher loadings improve electrical performance.

The novel synthesis of CNF grown directly upon the graphene layers *in situ* combined with the oxidation of the nickel nanoparticles allowed for both the increased ion and charge transport between graphene sheets and also pseudocapacitance behaviors, significantly improving upon electrical characteristics of either graphene or CNF individually, and providing a high specific surface area 3D material for use as electrode material in supercapacitors.

## **B. SUGGESTED NEXT STEPS**

Though the novelty of the synthesis has been proven, there are many possible next steps to advance the research described in this manuscript, several of which are now discussed.

The first advancement in the study of the 3D materials constructed herein is the adjustment of the variables of synthesis to optimize both surface area and capacitance. In this study, nickel loading was only performed at either 1 wt% or 3 wt% loading. Based on the electrical characterization, there appears to be an optimal loading for nickel nanoparticles and, as such, the nickel loading must continue to be adjusted and studied, in particular, the nickel loading should be increased. Along the same argument, CNF



loading may also be adjusted. In this study, nickel and CNF loading were dependent upon one another. A second future step could be to investigate the surface area and capacitance behaviors of the 3D architectures while holding nickel loading constant and altering CNF loading and vice versa, which could be accomplished by partially dissolving the nickel particles after the fiber growth. Other possible future directions could include adjusting the active material height on the electrode or evaluating other electrolytes (concentration and/or materials).

The final improvement upon the work executed in this study would be to perform more thorough electrical characterization. Cyclic voltammetry would yield capacitance values which could better be compared with those in current research. Moreover, several other electrical classifications should be performed to fully evaluate the materials created herein such as cycle life testing, impedance testing, power density classification, and energy density testing should each be performed to fully classify the electrical properties of the 3D graphene-CNF architectures containing NiO.

THIS PAGE INTENTIONALLY LEFT BLANK

## LIST OF REFERENCES

- [1] B. E. Conway, *Electrochemical Supercapacitors: Scientific Fundamentals and Technological Applications*. New York: Kluwer Academic/Plenum Publishers, 1999.
- [2] P. J. Hall, M. Mirzaeian, S. I. Fletcher, F. B. Sillars, A. J. R. Rennie, G. O. Shitta-Bey, G. Wilson, A. Cruden and R. Carter, "Energy storage in electrochemical capacitors: designing functional materials to improve performance," *Energy & Environmental Science*, vol. 3, pp. 1238–1251, Sep 2010.
- [3] Young. Electronics. Group. [Online]. Available: [http://yegultracapacitors.co.uk/expertise/ultra\\_vs\\_elec](http://yegultracapacitors.co.uk/expertise/ultra_vs_elec).
- [4] R. Carter and A. Cruden, Strategies for Control of a Battery/Supercapacitor System in an Electric Vehicle. 2008.
- [5] T. Markel, A. Brooker, I. Hendricks, V. Johnson, K. Kelly, B. Kramer, M. O’Keefe, S. Sprik and K. Wipke, "ADVISOR: a systems analysis tool for advanced vehicle modeling," *J. Power Sources*, vol. 110, pp. 255–266, Aug 2002.
- [6] D. R. Rolison, J. W. Long, J. C. Lytle, A. E. Fischer, C. P. Rhodes, T. M. McEvoy, M. E. Bourga and A. M. Lubers, "Multifunctional 3D nanoarchitectures for energy storage and conversion," *Chem. Soc. Rev.*, vol. 38, pp. 226–252, 2009.
- [7] E. Frackowiak and F. Beguin, "Carbon materials for the electrochemical storage of energy in capacitors," *Carbon*, vol. 39, pp. 937–950, 2001.
- [8] H. Shi, "Activated carbons and double layer capacitance," *Electrochim. Acta*, vol. 41, pp. 1633–1639, Jun 1996.
- [9] D. Y. Qu and H. Shi, "Studies of activated carbons used in double-layer capacitors," *J. Power Sources*, vol. 74, pp. 99–107, Jul 1998.
- [10] M. J. Allen, V. C. Tung and R. B. Kaner, "Honeycomb Carbon: A Review of Graphene," *Chem. Rev.*, vol. 110, pp. 132–145, Jan 2010.
- [11] K. S. Novoselov, A. K. Geim, S. V. Morozov, D. Jiang, Y. Zhang, S. V. Dubonos, I. V. Grigorieva and A. A. Firsov, "Electric field effect in atomically thin carbon films," *Science*, vol. 306, pp. 666–669, Oct 2004.
- [12] C. N. R. Rao, A. K. Sood, K. S. Subrahmanyam and A. Govindaraj, "Graphene: The New Two-Dimensional Nanomaterial," *Angewandte Chemie-International Edition*, vol. 48, pp. 7752–7777, 2009.

- [13] H. Bai, C. Li, X. Wang and G. Shi, "A pH-sensitive graphene oxide composite hydrogel," *Chemical Communications*, vol. 46, pp. 2376–2378, 2010.
- [14] C. Li and G. Shi, "Three-dimensional graphene architectures," *Nanoscale*, vol. 4, pp. 5549–5563, 2012.
- [15] Q. Chen, L. Zhang and G. Chen, "Facile Preparation of Graphene-Copper Nanoparticle Composite by in Situ Chemical Reduction for Electrochemical Sensing of Carbohydrates," *Anal. Chem.*, vol. 84, pp. 171–178, Jan 2012.
- [16] Z. Niu, J. Chen, H. H. Hng, J. Ma and X. Chen, "A Leavening Strategy to Prepare Reduced Graphene Oxide Foams," *Adv Mater*, vol. 24, pp. 4144–4150, Aug 2012.
- [17] Y. Xu, K. Sheng, C. Li and G. Shi, "Self-Assembled Graphene Hydrogel via a One-Step Hydrothermal Process," *Acs Nano*, vol. 4, pp. 4324–4330, Jul 2010.
- [18] F. Yavari, Z. Chen, A. V. Thomas, W. Ren, H. Cheng and N. Koratkar, "High Sensitivity Gas Detection Using a Macroscopic Three-Dimensional Graphene Foam Network," *Scientific Reports*, vol. 1, pp. 166, Nov 2011.
- [19] A. Castro Neto, F. Guinea and N. M. R. Peres, "Drawing conclusions from graphene," *Physics World*, vol. 19, pp. 33–37, Nov 2006.
- [20] F. Liu and T. S. Seo, "A Controllable Self-Assembly Method for Large-Scale Synthesis of Graphene Sponges and Free-Standing Graphene Films," *Advanced Functional Materials*, vol. 20, pp. 1930–1936, Jun 2010.
- [21] Z. Tang, S. Shen, J. Zhuang and X. Wang, "Noble-Metal-Promoted Three-Dimensional Macroassembly of Single-Layered Graphene Oxide," *Angewandte Chemie-International Edition*, vol. 49, pp. 4603–4607, 2010.
- [22] H. Sun, L. Cao and L. Lu, "Bacteria promoted hierarchical carbon materials for high-performance supercapacitor," *Energy & Environmental Science*, vol. 5, pp. 6206–6213, Mar 2012.
- [23] M. F. El-Kady, V. Strong, S. Dubin and R. B. Kaner, "Laser Scribing of High-Performance and Flexible Graphene-Based Electrochemical Capacitors," *Science*, vol. 335, pp. 1326–1330, Mar 2012.
- [24] V. Strong, S. Dubin, M. F. El-Kady, A. Lech, Y. Wang, B. H. Weiller and R. B. Kaner, "Patterning and Electronic Tuning of Laser Scribed Graphene for Flexible All-Carbon Devices," *Acs Nano*, vol. 6, pp. 1395–1403, Feb 2012.
- [25] T. V. Hughes and C. R. Chambers, "Manufacture of Carbon Filaments," U.S. Patent 405480, Jun 18, 1889.

- [26] W. Lu and D. D. L. Chung, "Mesoporous activated carbon filaments," *Carbon*, vol. 35, pp. 427–430, 1997.
- [27] Z. Fan, J. Yan, L. Zhi, Q. Zhang, T. Wei, J. Feng, M. Zhang, W. Qian and F. Wei, "A Three-Dimensional Carbon Nanotube/Graphene Sandwich and Its Application as Electrode in Supercapacitors," *Adv Mater*, vol. 22, pp. 3723–+, Sep 2010.
- [28] O. S. Kwon, T. Kim, J. S. Lee, S. J. Park, H. Park, M. Kang, J. E. Lee, J. Jang and H. Yoon, "Fabrication of Graphene Sheets Intercalated with Manganese Oxide/Carbon Nanofibers: Toward High-Capacity Energy Storage," *Small*, vol. 9, pp. 248–254, Jan 2013.
- [29] Q. Wang, Z. Wen and J. Li, "A hybrid supercapacitor fabricated with a carbon nanotube cathode and a TiO<sub>2</sub>-B nanowire anode," *Advanced Functional Materials*, vol. 16, pp. 2141–2146, Oct 2006.
- [30] C. Yuan, X. Zhang, Q. Wu and B. Gao, "Effect of temperature on the hybrid supercapacitor based on NiO and activated carbon with alkaline polymer gel electrolyte," *Solid State Ionics*, vol. 177, pp. 1237–1242, May 2006.
- [31] D. Wang, F. Li and H. Cheng, "Hierarchical porous nickel oxide and carbon as electrode materials for asymmetric supercapacitor," *J. Power Sources*, vol. 185, pp. 1563–1568, Dec 2008.
- [32] Y. G. Wang, L. Yu and Y. Y. Xia, "Electrochemical capacitance performance of hybrid supercapacitors based on Ni(OH)<sub>2</sub>/carbon nanotube composites and activated carbon," *J. Electrochem. Soc.*, vol. 153, pp. A743–A748, 2006.
- [33] A. Yuan and Q. Zhang, "A novel hybrid manganese dioxide/activated carbon supercapacitor using lithium hydroxide electrolyte," *Electrochem. Comm.*, vol. 8, pp. 1173–1178, 2006.
- [34] X. Zhao, C. Johnston and P. S. Grant, "A novel hybrid supercapacitor with a carbon nanotube cathode and an iron oxide/carbon nanotube composite anode," *Journal of Materials Chemistry*, vol. 19, pp. 8755–8760, 2009.
- [35] D. C. Marcano, D. V. Kosynkin, J. M. Berlin, A. Sinitskii, Z. Sun, A. Slesarev, L. B. Alemany, W. Lu and J. M. Tour, "Improved Synthesis of Graphene Oxide," *Acs Nano*, vol. 4, pp. 4806–4814, Aug, 2010.
- [36] A. R. Maxson, "Novel Synthesis and Characterization of Inorganic Fullerene Type WS<sub>2</sub> and Graphene Hybrids," M.S. thesis, Dept. of Mech. and Aero. Eng., Naval Postgraduate School, Monterey, CA, 2012.
- [37] H. Zea, C. C. Luhrs and J. Phillips, "Reductive/expansion synthesis of zero valent submicron and nanometal particles," *J. Mater. Res.*, vol. 26, pp. 672–681, Mar 2011.

- [38] C. Luhrs, M. Kane, Z. Leseman and J. Phillips, "Novel Process for Solid State Reduction of Metal Oxides and Hydroxides," *Metallurgical and Materials Transactions B-Process Metallurgy and Materials Processing Science*, vol. 44, pp. 115–122, Feb 2013.
- [39] H. Zea, C. Luhrs and J. Phillips, "Production submicron and nano metallic particles via reductive/expansion method," *Abstracts of Papers of the American Chemical Society*, vol. 242, Aug 2011.
- [40] A. W. Coats and J. P. Redfern, "Thermogravimetric analysis. A review." *Analyst*, vol. 88, pp. 906–924, 1963.
- [41] "Automated software assistant for the proper calculation of BET area of microporous materials," Quantachrome Inst., Boynton Beach, FL, Powder Tech Note 54, 2011.
- [42] D. R. Dreyer, S. Park, C. W. Bielawski and R. S. Ruoff, "The chemistry of graphene oxide," *Chem. Soc. Rev.*, vol. 39, pp. 228–240, 2010.
- [43] T. N. Lambert, C. C. Luhrs, C. A. Chavez, S. Wakeland, M. T. Brumbach and T. M. Alam, "Graphite oxide as a precursor for the synthesis of disordered graphenes using the aerosol-through-plasma method," *Carbon*, vol. 48, pp. 4081–4089, Nov 2010.
- [44] J. S. Bunch, A. M. van der Zande, S. S. Verbridge, I. W. Frank, D. M. Tanenbaum, J. M. Parpia, H. G. Craighead and P. L. McEuen, "Electromechanical resonators from graphene sheets," *Science*, vol. 315, pp. 490–493, Jan 2007.
- [45] X. Xie, L. Ju, X. Feng, Y. Sun, R. Zhou, K. Liu, S. Fan, Q. Li and K. Jiang, "Controlled Fabrication of High-Quality Carbon Nanoscrolls from Monolayer Graphene," *Nano Letters*, vol. 9, pp. 2565–2570, Jul 2009.
- [46] H. S. Ju, S. H. Choi and H. L. Lee, "Structures of Thermally and Chemically Reduced Graphene," *Mat. Lett.*, vol. 64, pp. 4, 2010.
- [47] S. Wakeland, R. Martinez, J. K. Grey and C. C. Luhrs, "Production of graphene from graphite oxide using urea as expansion-reduction agent," *Carbon*, vol. 48, pp. 3463–3470, Oct 2010.
- [48] A. Dato, J. Phillips and M. Frenklach, "Substrate-free Gas Phase Synthesis of Graphene Sheets," *Nano Lett.*, vol. 8, pp. 5, 2008.
- [49] D. Wei, Y. Liu, Y. Wang, H. Zhang, L. Huang and G. Yu, "Synthesis of N-Doped Graphene by Chemical Vapor Deposition and Its Electrical Properties," *Nano Letters*, vol. 9, pp. 1752–1758, May 2009.

- [50] M. J. McAllister, J. Li, D. H. Adamson, H. C. Schniepp, A. A. Abdala, J. Liu, M. Herrera-Alonso, D. L. Milius, R. Car, R. K. Prud'homme and I. A. Aksay, "Single sheet functionalized graphene by oxidation and thermal expansion of graphite," *Chemistry of Materials*, vol. 19, pp. 4396–4404, Sep 2007.
- [51] H. C. Schniepp, J. L. Li, M. J. McAllister, H. Sai, M. Herrera-Alonso, D. H. Adamson, R. K. Prud'homme, R. Car, D. A. Saville and I. A. Aksay, "Functionalized single graphene sheets derived from splitting graphite oxide," *J Phys Chem B*, vol. 110, pp. 8535–8539, May 2006.
- [52] C. Berger, Z. M. Song, T. B. Li, X. B. Li, A. Y. Ogbazghi, R. Feng, Z. T. Dai, A. N. Marchenkov, E. H. Conrad, P. N. First and W. A. de Heer, "Ultrathin epitaxial graphite: 2D electron gas properties and a route toward graphene-based nanoelectronics," *J Phys Chem B*, vol. 108, pp. 19912–19916, Dec 2004.
- [53] L. Lai, L. Chen, D. Zhan, L. Sun, J. Liu, S. H. Lim, C. K. Poh, Z. Shen and J. Lin, "One-step synthesis of NH<sub>2</sub>-graphene from in situ graphene-oxide reduction and its improved electrochemical properties," *Carbon*, vol. 49, pp. 3250–3257, Aug 2011.
- [54] M. Choucair, N. M. K. Tse, M. R. Hill and J. A. Stride, "Adsorption and desorption characteristics of 3-dimensional networks of fused graphene," *Surf. Sci.*, vol. 606, pp. 34–39, Jan 2012.
- [55] M. D. Stoller, S. Park, Y. Zhu, J. An and R. S. Ruoff, "Graphene-Based Ultracapacitors," *Nano Lett.*, vol. 8, pp. 3498–3502, 2008.
- [56] Y. Zhu, S. Murali, M. D. Stoller, K. J. Ganesh, W. Cai, P. J. Ferreira, A. Pirkle, R. M. Wallace, K. A. Cychoz, M. Thommes, D. Su, E. A. Stach and R. S. Ruoff, "Carbon-Based Supercapacitors Produced by Activation of Graphene," *Science*, vol. 332, pp. 1537–1541, Jun 2011.
- [57] C. Liu, Z. Yu, D. Neff, A. Zhamu and B. Z. Jang, "Graphene-Based Supercapacitor with an Ultrahigh Energy Density," *Nano Letters*, vol. 10, pp. 4863–4868, Dec 2010.

THIS PAGE INTENTIONALLY LEFT BLANK



## **INITIAL DISTRIBUTION LIST**

1. Defense Technical Information Center  
Ft. Belvoir, Virginia
2. Dudley Knox Library  
Naval Postgraduate School  
Monterey, California